Coherent Dynamic Nuclear Polarization: Mechanistic Insights and Experimental Advances

by

Yifu Ouyang

Submitted to the Department of Chemistry
in partial fulfillment of the requirements for the degree of

DOCTOR OF PHILOSOPHY IN CHEMISTRY

at the

MASSACHUSETTS INSTITUTE OF TECHNOLOGY

May 2025

© 2025 Yifu Ouyang. All rights reserved.

The author hereby grants to MIT a nonexclusive, worldwide, irrevocable, royalty-free license to exercise any and all rights under copyright, including to reproduce, preserve, distribute and publicly display copies of the thesis, or release the thesis under an open-access license.

Authored by: Yifu Ouyang
Department of Chemistry
May 19, 2025

Certified by: Robert G. Griffin
Arthur Amos Noyes Professor of Chemistry, Thesis Supervisor

Accepted by: Adam P. Willard
Professor of Chemistry
Graduate Officer

THESIS COMMITTEE

Thesis Supervisor

Robert G. Griffin
Arthur Amos Noyes Professor of Chemistry

Thesis Readers

Gabriela S. Schlau-Cohen
Thesis Committee Chair
Robert T. Haslam and Bradley Dewey Professor of Chemistry

Mei Hong
David A. Leighty Professor of Chemistry
Thesis Committee Member

Coherent Dynamic Nuclear Polarization: Mechanistic Insights and Experimental Advances

by

Yifu Ouyang

Submitted to the Department of Chemistry
on May 19, 2025 in partial fulfillment of the requirements for the degree of

DOCTOR OF PHILOSOPHY IN CHEMISTRY

ABSTRACT

Dynamic Nuclear Polarization (DNP) enhances the sensitivity of solid-state Nuclear Magnetic Resonance (NMR) by transferring polarization from electrons to nuclei. While traditional continuous-wave (CW) DNP has advanced through improved radical design, the development of pulsed DNP—employing short, high-power microwave bursts—has shown the advantages of coherent spin control. We present both theoretical and experimental investigations aimed at understanding and optimizing polarization transfer. On the theoretical side, we examined multiple DNP mechanisms, including a re-evaluation of the Overhauser effect in insulating solids and a foundational treatment of the chirped solid effect. We also identified a new transfer channel, termed Resonant Mixing, arising from interference effects under off-resonance driving. Building on these insights, we developed a general framework for analyzing amplitude-, phase-, and frequency-modulated pulses. This approach enables the design of hybrid pulse sequences that combine modulation and chirping to produce efficient, selective spin transfer. These sequences maintain high enhancement even at reduced microwave power, thereby improving scalability to high magnetic fields. To test the practical viability of this approach, we designed and evaluated a prototype 400 MHz/263 GHz probe incorporating new resonator and RF technologies. While the initial performance was limited, the system provided a testbed for future high-field pulsed DNP experiments under realistic conditions. Together, these results establish a theoretical and technical foundation for next-generation pulsed DNP, emphasizing coherent spin manipulation, power-efficient design, and applicability to high-field, static-solid NMR systems.

Thesis supervisor: Robert G. Griffin
Title: Arthur Amos Noyes Professor of Chemistry

Acknowledgments

First and foremost, I owe an immense debt of gratitude to my advisor, Professor Robert Griffin. Not only did he provide scientific guidance, mentorship, and the occasional drag force when I drifted too far from the topic, he also demonstrated heroic patience with my English. From misplaced adverbs to syntactically bold interpretations of formal writing, their tolerance made this thesis possible—and probably tested the limits of human resilience. Thank you for letting the science speak, even when the grammar tried not to.

I would also like to express sincere thanks to all my colleagues, including but not limited to members of the past and current group: Daniel Banks, Kong Ooi Tan, Michael Mardini, Natalie Golota, Ravi Shankar Palani, and Yifan Quan. Your seriousness, your discipline, and your unrelenting focus were a grounding force through every chaotic moment of this work. In a project defined by oscillations, detunings, and strange sidebands, you were the fixed reference. If I've ever appeared like I know what I'm doing, it's probably because you quietly made sure of it. To the many colleagues who weren't directly involved in this project but were always ready to lend a hand: thank you. Whether it was explaining a stubborn bit of code, sharing lab equipment you barely trusted me with, or simply exchanging ideas in the Melanie Cafe, your generosity and presence made the day-to-day challenges bearable—and sometimes even enjoyable. This thesis may be mine, but its survival owes plenty to your incidental heroism.

To the Chemistry department: thank you for your near-total absence. It's remarkable how smoothly research can progress when no one comes to bother on it. The silence in the hallways, the office in NW14 out of your reach, the Schrödinger's faculty — all of this created an environment uniquely suited for introspection, MATLAB crashes, and independent despair. I learned more about perseverance in your vacuum than I might have in a fully staffed ecosystem.

All these work would not be possible without talented technicians Dave Ruben, Stephen Thompson and Mike Mullins. Special thanks go to Ralph Weber, who is no longer with us. Your presence during the early stages of this work left a deep and lasting impact—scientifically, personally, and philosophically. I wish you could have seen where this ended up. I think you'd be proud, or at least amused.

To MIT, thank you for the resources, the Supercloud system that once was more open to us, the ever-surprising power surges, and the beautifully ambiguous laser safety trainings. (I heard they've been better these years.) Without you, this thesis would have required a much more expensive hobby.

To my friends: thank you for pretending to understand any of this, and for replying "sounds cool!" when I tried to explain pulse sequences over dinner. And the occasional sparks

when you do understand and inspired me. To my family: thank you for your love and support, and for constantly asking why I'm still in school. You are my ground state.

To the COVID-19 pandemic: your timing was truly impeccable. Thank you for turning lab shutdowns into scheduling puzzles, international conferences into awkward Zoom calls, and every minor cold into a week-long existential crisis. You made experimental delays longer, social life thinner, and motivation a rare and precious isotope. Yet somehow, through your unpredictable chaos, this work managed to progress—often in spite of you, never because of you.

And finally, to coffee. You were always there. Unlike the simulations. I don't drink coffee at all. But I have to do simulations. Alas.

Contents

List of Figures 11
List of Tables 13

1 Introduction **15**
1.1 Background and Scientific Motivation . . . 15
1.1.1 NMR in Physical and Biological Sciences . . . 15
1.1.2 Dynamic Nuclear Polarization: Concept and Promise . . . 16
1.1.3 Limitations of CW DNP . . . 16
1.1.4 Toward Enhanced DNP Platforms . . . 17
1.2 Principles of Dynamic Nuclear Polarization . . . 17
1.2.1 Spin Polarization and the Zeeman Reservoir . . . 18
1.2.2 Microscopic Interactions Enabling DNP . . . 19
1.2.3 Overhauser Effect (OE) . . . 19
1.2.4 Solid Effect (SE) . . . 19
1.2.5 Cross Effect (CE) . . . 21
1.2.6 Thermal Mixing (TM) . . . 21
1.2.7 Field Dependence and Regimes of Dominance . . . 22
1.2.8 Coherent Versus Incoherent Mechanisms . . . 22
1.2.9 Role of MAS in DNP . . . 23
1.2.10 Theoretical Descriptions and Their Limits . . . 23
1.2.11 Summary . . . 24
1.3 Emergence of Pulsed DNP . . . 24
1.3.1 Limitations of CW Saturation and the High-Field Regime . . . 24
1.3.2 Early Pulsed DNP Sequences . . . 25
1.3.3 Beyond NOVEL: Expanding the Pulse Toolkit . . . 25
1.3.4 A Need for New Theoretical Tools . . . 26
1.4 Open Questions and Theoretical Gaps . . . 27
1.5 Goals and Scope of This Thesis . . . 29

2 Pulsed DNP Sequences **31**
2.1 Introduction . . . 31
2.2 Theory . . . 32
2.2.1 Overview . . . 32
2.2.2 Driven Spin Dynamics . . . 32
2.2.3 Frequency Domain Analysis . . . 34

2.2.4 Spin Trajectory Analysis . . . 35
2.2.5 Powder Averaging and MAS Integration . . . 37
2.2.6 Landau-Zener Transition . . . 39
2.3 Methods . . . 41
2.4 Results and Discussion . . . 42
2.4.1 TPPM . . . 43
2.4.2 Adiabatic Spin Transfer via Chirped TPPM . . . 44
2.4.3 TOP . . . 47
2.4.4 XiX . . . 49
2.5 Conclusions and Discussion . . . 51
2.6 Supporting Information . . . 54

3 Overhauser Effect and Resonant Mixing 67
3.1 Amplified Overhauser DNP with Selective Deuteration . . . 67
3.1.1 Synthesis . . . 70
3.1.2 DNP Experiments . . . 70
3.1.3 Discussion . . . 74
3.2 Resonant Mixing DNP . . . 77
3.2.1 Introduction . . . 77
3.2.2 Experiments and Analysis . . . 79
3.2.3 Theory . . . 81
3.2.4 Conclusion . . . 85
3.3 Resonant Mixing DNP with Overhauser Effect . . . 86
3.3.1 Introduction . . . 86
3.3.2 Theory . . . 87
3.3.3 Numerical Simulation . . . 93
3.3.4 Experimental Results . . . 95
3.4 Summary and Discussions . . . 103

4 Instrumentation for High-Field Pulsed DNP 105
4.1 Introduction . . . 105
4.2 Pulse Generation at 250 GHz . . . 105
4.3 Requirements for Pulsed DNP Probes . . . 107
4.4 Resonator Designs Developed . . . 108
4.4.1 Helical-Cut Resonator . . . 108
4.4.2 Disc-Assembled Resonator (Machined Modular Design) . . . 109
4.5 MAS Compatibility and Integration Challenges . . . 111
4.6 Summary and Outlook . . . 112

5 Conclusions and Outlook 115

A Code listing 117

References 149

List of Figures

1.1 Comparioson of electron polarization and nuclear polarization under the same experimental conditions . . . 18
1.2 Overhauser Effect recently discovered in non-insulating solids[10] . . . 20

2.1 Simulated TPPM trajectory and power spectrum . . . 36
2.2 Schematics of DNP pulses . . . 41
2.3 TPPM, TOP and XiX Sequences. . . . 42
2.4 TPPM optimal parameter scan . . . 43
2.5 TPPM enhancement with a preparation pulse . . . 45
2.6 Phase-Chirped TPPM sequence . . . 46
2.7 Frequency shift in Phase-Chirped TPPM sequence . . . 47
2.8 Improvement of Phase-Chirped TPPM sequence . . . 48
2.9 TOP parameter scan . . . 49
2.10 XiX parameter scan . . . 51
2.11 TOP parameter scan at several other frequency offsets . . . 57
2.12 Prep-pulse determined ω_{1S} . . . 58
2.13 Contact-time relationship for multiple pulse schemes. . . . 59
2.14 Contact curve for several pulse sequences . . . 62
2.15 Frequency-swept enhancement spectra for several pulse sequences . . . 65

3.1 Deuteration of phenyl ring on BDPA radical leads to larger OE enhancement 68
3.2 Synthetic route to Phe-d_5-BDPA radical . . . 70
3.3 DNP comparison between partially- and fully-deuterated BDPA . . . 72
3.4 DNP comparison between partially- and non-deuterated BDPA across four different magnetic fields . . . 73
3.5 Enhancement vs (a) MAS rate and (b) microwave power for h_{21}- and Phe-d_5-BDPA. . . . 75
3.6 Resonant Mixing schematics . . . 77
3.7 Dispersive center feature of OX063 DNP field profile at 600 MHz, with simulations 79
3.8 Dispersive center feature of OX063 DNP field profile at 380 MHz, with simulations 80
3.9 140 GHz concentration-dependent EPR of Trityl . . . 81
3.10 140 GHz concentration-dependent EPR of Trityl . . . 82
3.11 New frame formation . . . 90
3.12 Calculated DNP Zeeman profile from arbitrary parameters . . . 94
3.13 DNP Zeeman profiles of selectively deuterated BDPA from [59] . . . 95

3.14 Simulated DNP Zeeman profile from arbitrary parameters 96
3.15 Temperature dependence of DNP field profile at 380 MHz 97
3.16 Temperature dependence of DNP field profile at 211 MHz 98
3.17 260 GHz EPR for matrices of different solvent and concentration 99
3.18 Central feature distortion by Gd doping of trityl sample at 600 MHz 100
3.19 Central feature distortion by Gd doping of trityl sample at 380 MHz 101
3.20 Relaxation effect by Gd doping of trityl sample at Q-band 102

4.1 Comparison of MAS stator with microwave resonator structure 106
4.2 Simulated electric field distribution and microwave power distribution of resonator 109
4.3 Test of early resonator design 110
4.4 The disc-assembled resonator 111

List of Tables

2.1 Comparison of pulsed DNP sequences 50

3.1 ^{1}H T_1 and DNP buildup times T_B for h_{21}-BDPA and Phe-d_5-BDPA at 8.9 and 14.1 T. 73

3.2 DNP enhancement ε values for h_{21}-BDPA and Phe-d_5-BDPA at multiple fields 74

Chapter 1

Introduction

1.1 Background and Scientific Motivation

1.1.1 NMR in Physical and Biological Sciences

Nuclear Magnetic Resonance (NMR) spectroscopy is a powerful, non-destructive analytical method used to probe the atomic-scale structure and dynamics of matter. It plays a foundational role in both the physical sciences—where it informs quantum chemistry, catalysis, materials science, and condensed matter physics—and the biological sciences, enabling insight into protein folding, membrane structure, metabolomics, and drug interactions.

The continuous advancement of instrumentation has propelled the utility and resolution of NMR spectroscopy. High-field superconducting magnets, now reaching up to 1.2 GHz proton resonance frequencies [1], provide improved dispersion and sensitivity. Parallel improvements in radio-frequency (RF) transmitter and receiver technology, low-noise detection schemes, and cryogenically cooled electronics have significantly enhanced signal-to-noise ratios. In solid-state NMR (SSNMR), Magic Angle Spinning (MAS) has been a key innovation: by spinning samples at the "magic angle" of 54.7° relative to the magnetic field, anisotropic interactions—such as dipolar couplings and chemical shift anisotropy—can be averaged out, yielding narrower lines and more interpretable spectra.

NMR operates on the principle of the Zeeman interaction, where nuclear spin states experience an energy splitting in a static external magnetic field B_0. The energy separation between spin states is given by

$$\Delta E = \hbar \gamma B_0 \tag{1.1}$$

where γ is the gyromagnetic ratio and $\hbar$ is the reduced Planck constant. This energy splitting leads to a Boltzmann population imbalance:

$$\frac{N_\uparrow - N_\downarrow}{N_\uparrow + N_\downarrow} \approx \frac{\hbar \gamma B_0}{2 k_B T} \tag{1.2}$$

At room temperature and high field, this ratio is typically on the order of 10^{-5} to 10^{-4}, resulting in inherently weak signal intensity. In practice, improving sensitivity requires signal averaging over long acquisition times, isotopic enrichment (e.g., ^{13}C, ^{15}N), and advanced pulse sequences to manipulate spin coherences.

In the solid state, spectral resolution and sensitivity face additional challenges. Unlike solutions, where molecular tumbling averages out dipolar and quadrupolar interactions, solids retain strong anisotropic couplings. These broaden spectral lines, reduce coherence lifetimes, and complicate spectral interpretation. MAS and cross-polarization (CP) techniques mitigate these effects, but they require specialized hardware and careful calibration. Even under optimized conditions, acquiring high-quality data often demands milligram quantities of sample and extensive signal averaging [2, 3].

1.1.2 Dynamic Nuclear Polarization: Concept and Promise

Dynamic Nuclear Polarization (DNP) addresses the fundamental sensitivity limitation of NMR by leveraging the large magnetic moment and high polarization of unpaired electrons. Under microwave irradiation, polarization is transferred from electron spins—typically introduced via paramagnetic radicals—to neighboring nuclear spins, increasing the detectable nuclear magnetization far beyond thermal equilibrium values.

The resulting gain is characterized by the enhancement factor ε, defined as

$$\varepsilon = \frac{S_{\text{DNP}}}{S_{\text{thermal}}} \tag{1.3}$$

Enhancements of 10–100× are routinely achieved in practice, with the theoretical upper bound given by the ratio of electron to nuclear gyromagnetic ratios (e.g., $\gamma_e/\gamma_H \approx 658$ for protons). While such maximal values are rarely reached due to relaxation effects, depolarization, and leakage pathways, even modest enhancements can transform NMR into a viable technique for previously inaccessible samples—such as dilute bio-molecules, intact cells, or non-crystalline materials.

DNP is particularly powerful in biological contexts where sample quantity is limited or isotopic labeling is challenging. It has enabled new directions in membrane protein structure, in-cell NMR, metabolic profiling, and time-resolved studies of enzymatic function[4–6]. In the realm of materials science, DNP enhances the study of heterogeneous catalysts, battery interfaces, and metal organic frameworks where sensitivity limits otherwise obscure critical features[7–9].

1.1.3 Limitations of CW DNP

Despite its great potential, traditional DNP implementations have several intrinsic limitations. Most conventional experiments employ continuous-wave (CW) microwave irradiation to saturate electron spin transitions near the Larmor frequency. This approach is conceptually straightforward, and many DNP mechanisms—such as the Overhauser effect[10], solid effect[11], and cross effect[12]—can be efficiently realized under CW driving. However, CW-DNP faces significant performance bottlenecks in several key regimes:

- **High magnetic fields:** As field strength increases, the electron-nuclear energy mismatch widens, and direct polarization transfer becomes less efficient. Electron spin relaxation times may also decrease, reducing polarization buildup [13].

- **High MAS rates:** MAS is essential for line narrowing in solids, but at fast spinning speeds (e.g., $> 40\,\text{kHz}$), many DNP mechanisms lose their efficiency due to motional averaging of the necessary dipolar interactions [14].
- **Microwave power limitations:** At frequencies corresponding to high magnetic fields (e.g., 263 GHz for 400 MHz ^{1}H), producing sufficient microwave power to saturate electron transitions becomes a major challenge. Gyrotrons, while powerful, are bulky, expensive, and difficult to tune.

In addition, most high-field DNP experiments rely on cryogenic MAS at temperatures below 100 K. While this boosts polarization retention and spin-lattice relaxation times, it adds considerable technical complexity. Cryogenic systems must maintain stable spinning, manage sample cooling, and contend with thermal gradients and hardware fragility.

Thus, the optimization of DNP remains a multi-dimensional problem, requiring simultaneous tuning of radical chemistry, field strength, microwave irradiation, sample temperature, and MAS rate. Recent developments have aimed to alleviate these constraints via improved polarizing agents, radical tags, and alternative DNP mechanisms [15, 16].

1.1.4 Toward Enhanced DNP Platforms

To overcome these challenges, research has turned to multiple fronts. Chemically, the development of next-generation bi-radicals—such as NaphPol, TEMTriPol, and AMUPol derivatives—has improved DNP performance across a range of solvents, pH conditions, and field strengths. These radicals are engineered for long electron relaxation times, high solubility, and reduced inhomogeneous broadening, making them ideal for high-field operation [15].

Technological advances have also played a critical role. Innovations in cryogenic MAS hardware now enable stable operation at temperatures below 30 K, significantly boosting polarization lifetimes and enabling longer acquisition windows without depolarization [17]. Meanwhile, developments in waveguide design and frequency-agile gyrotrons are beginning to allow more flexible microwave control in high-field settings[18].

However, despite these advances, the reliance on CW irradiation and MAS remains a limitation. New strategies are needed—ones that reduce power requirements, improve coherence, and offer greater control over the spin dynamics of the electron-nuclear system. Pulsed DNP presents a promising path forward, offering the possibility of resonant, selective, and coherent polarization transfer using shaped microwave bursts. It is this direction—both theoretical and experimental—that this thesis explores.

1.2 Principles of Dynamic Nuclear Polarization

Dynamic Nuclear Polarization (DNP) enhances nuclear spin polarization by transferring it from electron spins, which possess significantly greater thermal polarization at a given temperature and magnetic field. The origin of this contrast lies in the gyromagnetic ratio: electrons are approximately three orders of magnitude more magnetically responsive than nuclei, leading to much higher Boltzmann polarization under otherwise identical conditions.

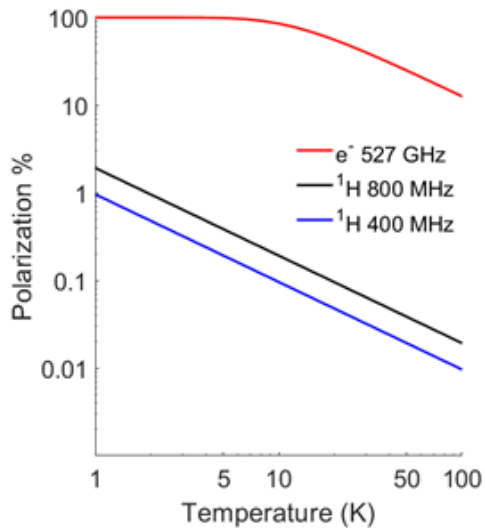

Figure 1.1: Comparioson of electron polarization and nuclear polarization under the same experimental conditions. The electron polarization is significantly higher.

DNP was first proposed by Overhauser in 1953 in the context of metallic conduction electrons[19]. Since then, DNP has evolved into a diverse family of techniques applied across NMR spectroscopy, magnetic resonance imaging (MRI)[20], and quantum sensing[21]. At its core, DNP is a nonequilibrium process: energy is injected into the electron spin system via microwave irradiation, which is then transferred to nuclear spins through spin-spin couplings and relaxation pathways. The resulting enhancement of nuclear polarization enables dramatic gains in sensitivity, making DNP an essential tool in modern solid-state NMR.

1.2.1 Spin Polarization and the Zeeman Reservoir

Under a magnetic field B_0, both nuclear and electron spins experience Zeeman splitting:

$$\mathcal{H}_Z = -\gamma \hbar B_0 S_z \tag{1.4}$$

The polarization of a spin-$\frac{1}{2}$ ensemble at temperature T is given by the Boltzmann distribution:

$$P = \frac{N_\uparrow - N_\downarrow}{N_\uparrow + N_\downarrow} = \tanh\left(\frac{\hbar \gamma B_0}{2 k_B T}\right) \tag{1.5}$$

For example, at $B_0 = 18.8\,\mathrm{T}$ and $T = 100\,\mathrm{K}$, the electron polarization is approximately 0.13, while the proton polarization is only about 2×10^{-4}. This disparity creates a powerful thermodynamic drive for polarization transfer.

Spin systems in solids are often modeled using “reservoirs”: the electron Zeeman reservoir, the bulk nuclear Zeeman reservoir, and the nuclear Zeeman reservoir inside the "spin diffusion barrier"[22]. Microwave irradiation perturbs these subsystems, inducing entropy flow and polarization redistribution. DNP mechanisms manipulate these pathways—some incoherently, some coherently—to increase nuclear polarization.

1.2.2 Microscopic Interactions Enabling DNP

Polarization transfer from electrons to nuclei depends on spin-spin interactions. In solid state, the relevant coupling is typically dipolar:

$$\mathcal{H}_{\mathsf{hf}} = \mathbf{S} \cdot \mathbf{A} \cdot \mathbf{I} \tag{1.6}$$

where $\mathbf{A}$ is the hyperfine tensor. This interaction mixes electron and nuclear states, making otherwise forbidden transitions weakly allowed under microwave irradiation. In some cases, scalar (Fermi contact) interactions also contribute.

These interactions form the basis for various DNP mechanisms. Below, we review the main mechanisms relevant to insulating solids under high-field conditions.

1.2.3 Overhauser Effect (OE)

The Overhauser effect is a two-spin cross-relaxation mechanism relying on electron–nuclear interactions and stochastic modulation due to molecular motion. In liquids, rapid tumbling leads to time-dependent fluctuations in the electron–nuclear coupling, enabling transitions such as S_+I_- and S_-I_+. When microwaves saturate the electron transition, these cross-relaxation pathways redistribute spin populations, resulting in net nuclear polarization.

The enhancement is characterized by:

$$\varepsilon = -f \cdot \xi \cdot \frac{\gamma_e}{\gamma_n} \tag{1.7}$$

where f is the leakage factor indicating the transfer efficiency of cross-polarization, and ξ is the coupling factor, representing the fraction of retained polarization under bulk relaxation[23].

In non-insulating solids, the Overhauser mechanism is thought to be largely inactive due to the lack of molecular motion. However, recently in this group we've found that it might actually be effective in some systems, which will be discussed thoroughly later in this thesis.

1.2.4 Solid Effect (SE)

The Solid Effect is the dominant mechanism in low-field, rigid solids with narrow electron lines. It involves a two-spin system (one electron, one nucleus) with a dipolar coupling.

The Hamiltonian in the lab frame is:

$$\mathcal{H} = \omega_e S_z + \omega_n I_z + A S_z I_z + B(S_+I_- + S_-I_+) \tag{1.8}$$

where A and B characterize the secular and flip-flop parts of the hyperfine interaction. Transitions at $\omega = \omega_e \pm \omega_n$ are formally forbidden (as they involve simultaneous spin flips), but become weakly allowed through $B \neq 0$.

Microwave irradiation at one of these frequencies can drive these mixed transitions, resulting in a net increase (or decrease) in nuclear polarization depending on which sideband is used. The solid effect is most efficient when:

- The electron linewidth is narrow,

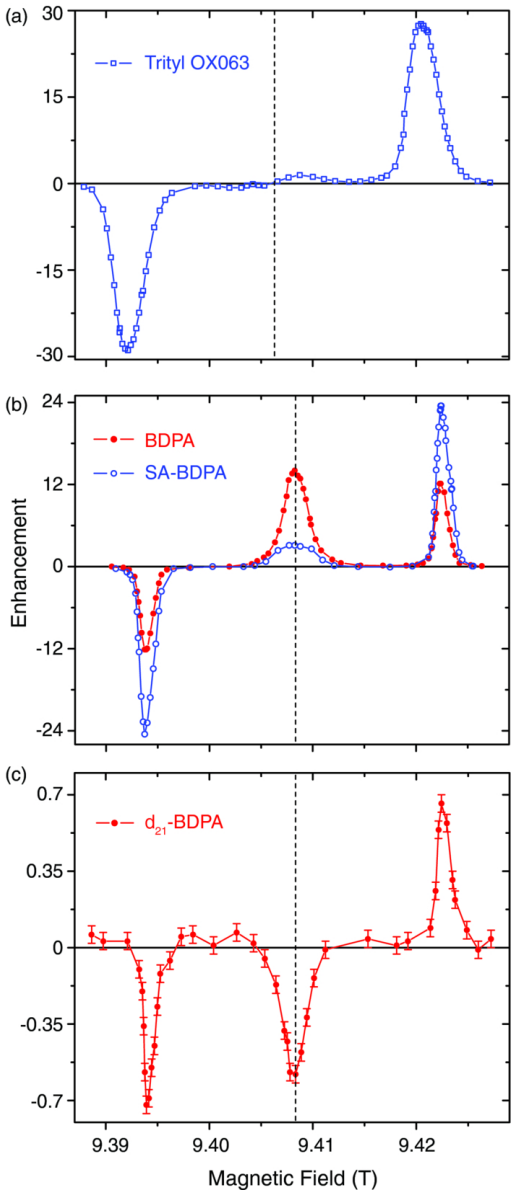

Figure 1.2: Overhauser Effect recently discovered in non-insulating solids with radicals BDPA, SA-BDPA, and deuterated BDPA. Figure reproduced from [10].

- The coupling is strong,
- And the microwave field is sufficiently strong to overcome the forbidden nature of the transition.

At high fields, SE becomes inefficient due to increasing detuning and the reduced overlap between the electron line and the $\omega_e \pm \omega_n$ transitions[11].

1.2.5 Cross Effect (CE)

The Cross Effect is a three-spin mechanism involving two electrons and one nucleus. It is efficient in inhomogeneously broadened systems where $\omega_{e1} - \omega_{e2} \approx \omega_n$, and where the electrons are weakly dipolar-coupled. This is usually achieved by biradicals, where two radical centers are bound together by bonds, although sometimes monoradical with a large g-anisotropy is used[24].

The intuitive picture is as follows: microwave irradiation at frequency $\omega \approx \omega_{e1}$ saturates one electron transition. This induces a polarization gradient between two electrons. The nuclear spin acts as a mediator, enabling the simultaneous flip-flop $S_{1+}S_{2-}I_{-}$. This three-body process transfers polarization efficiently, particularly under MAS, where time-dependent averaging creates periodic resonance conditions[25].

The CE is favored at high fields because:

- The electron linewidth caused by g-anisotropy scales as fast as the nuclear frequency,
- MAS brings the matching condition into transient resonance,
- the non-forbidden transition is less affected by high fields,
- And modern biradicals (e.g., AMUPol, TEMTriPol-I) are designed to optimize the necessary electron–electron spacing[26].

Because the CE relies on a three-body coherence, it is particularly sensitive to electron relaxation, and is enhanced by fast spin diffusion across the radical ensemble[12].

1.2.6 Thermal Mixing (TM)

Thermal Mixing arises when the electron–electron dipolar interaction is strong and broad enough to allow for spectral diffusion[27]. In this case, individual interactions responsible for cross-polarization is hard to distinguish, so TM is mostly analyzed on a ensemble basis. The electron ensemble behaves as a thermal reservoir, characterized by a spin temperature T_s, which can be manipulated via microwave irradiation. The nuclei then equilibrate with this reservoir through flip-flop interactions, resulting in nuclear polarization that reflects T_s.

The theory assumes rapid spectral diffusion within the electron line and weak coupling between the electron Zeeman and dipolar reservoirs. Under microwave irradiation, spin energy is redistributed across the electron line, producing an effective "temperature gradient" that drives nuclear polarization. This is formalized by:

$$P_n = \tanh\left(\frac{\hbar\gamma_n B_0}{2k_B T_s}\right) \tag{1.9}$$

Thermal mixing is efficient at low temperatures (typically below 20 K), moderate fields (3–5 T), and at high radical concentration. At very high fields, the assumptions of TM break down: spectral diffusion becomes slower, the line becomes broader, and the spin reservoirs may no longer be well-defined. As such, TM is rarely observed at fields $> 9.4\,\mathrm{T}$.

1.2.7 Field Dependence and Regimes of Dominance

The relative importance of the different DNP mechanisms depends strongly on the external magnetic field B_0, the microwave frequency, temperature, and the properties of the polarizing agent. Each mechanism occupies a different region of the DNP "phase diagram," typically visualized as a function of field and temperature.

- **Low fields (0.3–5 T):** The solid effect and thermal mixing dominate. The narrow separation between electron and nuclear Zeeman levels allows for efficient forbidden transitions and ensemble-level spin exchange. This was the regime of early DNP experiments.
- **Intermediate fields (5–10 T):** The cross effect becomes increasingly important, particularly under MAS. The matching condition $|\omega_{e1} - \omega_{e2}| \approx \omega_n$ is readily met in disordered electron ensembles, and dipolar coupling between radical pairs enables efficient transfer.
- **High fields (10–18 T and beyond):** Classical DNP mechanisms lose efficiency. Forbidden transitions (SE) become too weak, spectral diffusion slows down (TM), and CE also suffers. Alternative strategies—chirped pulses, adiabatic transitions, pulsed DNP—is what we propose to be most efficien in this region.

The increasing reliance on MAS at high field is both a strength and a limitation. While MAS enhances resolution, it introduces technical complexity and may suppress essential dipolar couplings. This motivates the development of MAS-synchronized polarization methods, such as those based on tailored pulse sequences.

1.2.8 Coherent Versus Incoherent Mechanisms

DNP mechanisms can be broadly classified into two categories: incoherent (relaxation-mediated) and coherent (driven by Hamiltonian evolution). This distinction is central to understanding the limitations of traditional theory and the potential of pulse-engineered DNP.

Incoherent transfer: Continuous wave DNP, for example OE and TM, operate through stochastic processes involving spectral diffusion and cross-relaxation. These mechanisms are well-described by classical rate models and spin temperature theory. They are robust but often slow, and sensitive to spin-lattice relaxation and depolarization pathways.

Coherent transfer: SE and CE can, under the right conditions, be driven coherently using resonant microwave irradiation. In this regime, polarization transfer is governed by the unitary evolution of a coupled spin system. The outcome depends on pulse duration, detuning, coupling strength, and pulse shape.

This coherent regime becomes particularly relevant in pulsed DNP, where the goal is to drive spin transitions in a controlled, phase-sensitive manner[28]. In contrast to CW saturation, pulsed sequences may produce highly selective, resonant polarization transfer using short, shaped bursts of microwaves.

1.2.9 Role of MAS in DNP

Magic Angle Spinning (MAS) plays a dual role in solid-state DNP. On the one hand, it improves spectral resolution by averaging anisotropic interactions, being essential for NMR practice. On the other, it modulates dipolar couplings in time, affecting DNP efficiency.

Under MAS, dipolar interactions become time-dependent, and mechanisms like the CE rely on transient passages through matching conditions. This has led to the development of rotor-synchronized sequences and MAS-enhanced DNP mechanisms. However, MAS-DNP is not always feasible, as hardware constraints at high magnetic fields limit the available microwave power inside MAS stators, thereby reducing the efficiency of microwave irradiation and the resulting DNP enhancement[29].

Much of low-field DNP experiments has focused on polarization transfer under static conditions, without MAS. Moving to higher fields requires rethinking how coherence and orientation are handled—leading to new models for DNP that may or may not rely on periodic averaging.

1.2.10 Theoretical Descriptions and Their Limits

Most of the established theoretical tools for DNP fall into one of the following categories:

Rate Equations and Spin Temperature Theory: These are most suitable for incoherent mechanisms in CW DNP. They describe average polarization transfer rates, thermal reservoirs, and energy redistribution. However, they ignore phase coherence, transient dynamics, and non-equilibrium behavior. The Bloch-Redfield-Wangsness theory based on Bloch equations is usually key to this topic[30, 31].

Floquet Theory: Floquet analysis is more general and can handle periodic, strongly modulated systems. It has been applied to pulsed DNP, but becomes analytically intractable for complex pulse shapes or when relaxation is significant. Moreover, it often obscures physical intuition[32, 33].

Average Hamiltonian Theory (AHT): AHT describes time-dependent spin systems under periodic driving. It has been used to analyze MAS-enhanced CE, rotor synchronization, and pulsed SE. However, AHT assumes weak time-dependent perturbations and periodicity—assumptions that break down in the presence of shaped or chirped pulses[34].

Numerical Simulations: Exact simulations using spin density matrices, Liouville-von Neumann evolution, or Monte Carlo methods provide detailed predictions, but at high computational cost. These methods are essential for benchmarking but often lack transparency and generality, depending heavily on the system parameters which are mostly guesses. Examples of these include SPINEVOLUTION [35], Spinach [36], and DNPSOUP [37].

1.2.11 Summary

DNP has transformed the sensitivity landscape of solid-state NMR, enabling applications across chemistry, biology, and materials science. Yet, as field strengths rise and sample demands grow more complex, conventional approaches are nearing their limits.

The classical mechanisms of Overhauser, solid effect, cross effect, and thermal mixing have served the field well, but each has its drawbacks. Theoretical tools like AHT and spin temperature theory provide valuable guidance, but do not capture the full richness of coherent, shaped, or resonant pulse-driven dynamics.

This thesis builds on these foundations but goes beyond them—developing new frameworks to understand and optimize polarization transfer under strong, time-modulated microwave driving. The chapters that follow aim to formalize this picture, grounded in both theory and experiment.

1.3 Emergence of Pulsed DNP

While continuous-wave (CW) DNP has led to significant sensitivity enhancements in solid-state NMR, its efficiency diminishes at high magnetic fields due to several intrinsic limitations. These include electron saturation challenges, microwave power losses, and the inefficiency of forbidden transition pathways. Pulsed DNP, which replaces continuous irradiation with short, shaped microwave bursts, has emerged as a promising alternative for overcoming these barriers.

1.3.1 Limitations of CW Saturation and the High-Field Regime

The traditional approach to DNP relies on saturating electron spin transitions using CW microwave irradiation. In the solid effect (SE) and cross effect (CE), this drives polarization transfer from electrons to nuclei through time-independent, incoherent mechanisms. However, at high fields (e.g., 14.1 T and above), several issues become prominent:

- **Reduced transition probabilities:** Forbidden transitions (e.g., $\omega_e \pm \omega_n$) become more off-resonant as the field increases, diminishing their transition rates.
- **Microwave inefficiency:** Higher frequencies (e.g., 527 GHz at 800 MHz ^{1}H) suffer greater losses in microwave sources, waveguides and sample chambers, leading to reduced microwave amplitude at the sample.
- **Power saturation limitations:** Electron spin transitions often cannot be fully saturated within MAS stators at high fields due to geometric and dielectric constraints [38].

- **Line broadening and inhomogeneity:** Broad electron linewidths and inhomogeneous distributions reduce the effectiveness of uniform CW irradiation. Especially g-anisotropy, which means that most of the EPR line is not covered by a mono-frequency source.

These limitations motivate a shift away from power- and saturation-based transfer and toward selective, time-domain control of spin transitions—i.e., pulsed DNP.

Time-Domain Polarization Transfer: Conceptual Shift Pulsed DNP represents a fundamental conceptual shift from incoherent saturation to coherent control. Rather than applying continuous microwaves to randomize the electron spin population, shaped pulses are used to enact specific quantum evolutions that directly couple electron and nuclear spin states.

In this framework, the goal is not to saturate transitions, but to drive population transfer along selected spin pathways using tailored dynamics. This is more akin to techniques used in quantum control or magnetic resonance spectroscopy than classical DNP. The advantages include:

- **Selectivity:** Pulses can be designed to target specific transitions or spin orientations.
- **Power efficiency:** Coherent driving can achieve transfer without requiring full saturation, reducing power demands.
- **New mechanisms:** Chirped pulses and modulated waveforms can access transfer pathways not available in CW-DNP.

1.3.2 Early Pulsed DNP Sequences

The earliest and most widely known pulsed DNP method is NOVEL (Nuclear Orientation via Electron Spin Locking), introduced by Henstra et al. [39]. NOVEL applies a continuous spin-lock pulse to the electron spin system while the nuclear spins evolve freely. When the Rabi frequency of the electron matches the nuclear Larmor frequency, efficient polarization transfer occurs through a double-quantum transition.

The NOVEL Hamiltonian in the doubly rotating frame is:

$$\mathcal{H}_{\mathsf{NOVEL}} = \delta S_z + \omega_1 S_x + \omega_n I_z + A S_z I_z + B(S_+ I_- + S_- I_+) \tag{1.10}$$

Resonance occurs when $\omega_1 = \omega_n$, and δ is the detuning from the spin-lock frame. This resonance condition defines the starting point for many subsequent pulsed methods.

1.3.3 Beyond NOVEL: Expanding the Pulse Toolkit

Building on the NOVEL framework, two main catagories of pulsed DNP sequences have been developed to enhance transfer efficiency, selectivity, and robustness:

- **Adiabatic Pulses:** Integrated solid effect (ISE) [40] and ramped-amplitude NOVEL (RA-NOVEL) [41] apply chirped pulses that slowly traverse resonance conditions. These are more robust to line broadenings and frequency/field detunings.

- **Modulated Pulses:** Sequences such as TOP, XiX, TPPM use alternating periodic pulse trains to generate effective fields that drive polarization transfer, borrowing ideas from the NMR cross-polarization technique [42–44].

Each of these sequences offers trade-offs between enhancement, robustness, pulse duty cycle, and power requirements. Many rely on resonance conditions involving microwave power (ω_{1S}), nuclear Larmor frequency (ω_n), effective pulse-driving field (ω_{eff}), or combinations thereof.

Challenges in Pulsed DNP Implementation Despite their promise, pulsed DNP sequences face several implementation challenges:

- **Power and timing precision:** Precise control of microwave amplitude, phase, and duration is needed, often beyond the capabilities of standard DNP instrumentation.
- **Orientation dependence:** Most sequences rely on specific matching conditions between the microwave driving field and the hyperfine interaction terms, which becomes problematic in powders where anisotropy broadens and detunes the matching.
- **Electron T_2 decay:** Spin dynamics is only coherent within the dephasing time of the electron spin system, limiting pulse durations.
- **Relaxation losses:** Inefficient polarization diffusion away from the polarizing agent may reduce net enhancement.

Recent work has begun to address these issues through different aspects, such as optimal control theory and broadband pulses[45, 46].

1.3.4 A Need for New Theoretical Tools

Unlike CW-DNP, where spin temperature and rate equations offer sufficient explanatory power, pulsed DNP operates in a regime dominated by coherent spin dynamics, strong time dependence, and specific evolution pathways. The Hamiltonians are no longer static, and the outcomes depend on the full time dynamics of the spin system.

This necessitates new theoretical tools that:

- Track spin evolution under arbitrary time-dependent fields.
- Identify conditions responsible for polarization transfer.
- Allow for pulse design of efficient sequences.
- Predict enhancement efficiency from simulations.

1.4 Open Questions and Theoretical Gaps

Although pulsed DNP has demonstrated remarkable potential in overcoming limitations of traditional CW-based approaches, its physical basis remains less well understood. Empirical success with sequences such as NOVEL, ASE, TPPM, and chirped pulses has outpaced the development of generalizable theory. As a result, much of pulsed DNP remains a black box: specific pulse parameters yield high enhancements, sometimes confirmed by simulations, but the mechanisms behind such outcomes are not always clear.

This section outlines the central theoretical gaps that motivate the present work.

Lack of Predictive Frameworks for Optimizing Pulses Many pulsed DNP sequences operate under conditions of strong, resonant, or time-dependent driving. In these regimes, the Hamiltonian is nontrivial and sometimes lacks periodicity. Classical methods such as Average Hamiltonian Theory (AHT) become unreliable when the microwave pulses are non-periodic.

Moreover, the spin system's behavior during a pulse can dominate the overall polarization outcome, making a time-resolved treatment of spin dynamics essential. Without such tools, the optimization of pulse sequences remains a largely empirical task, reliant on brute-force parameter sweeps and simulation-based searches.

Ambiguity in Mechanism: What Enables Transfer? Different pulsed DNP sequences appear to rely on distinct physical mechanisms. NOVEL is typically interpreted as a driven zero-quantum transfer process, while ASE and chirped pulses are described in terms of adiabatic passage or Landau–Zener transitions. Sequences like TOP, XiX, and TPPM generate effective Hamiltonians that have no simple analog in the traditional DNP framework. Yet, no unifying description connects these mechanisms under a single formalism.

Key questions remain unresolved: Is polarization transfer always resonant in nature, or can non-resonant pathways dominate? Do coherence and relaxation enhance or degrade the polarization process? Which features of the driven spin dynamics correlate with successful transfer? And finally, can the polarization efficiency be predicted directly from the hyperfine terms? These questions point to a need for a model that treats the microwave field not as a saturation mechanism, but as a tool for driving coherent, controllable spin trajectories.

Orientation Dependence and the Role of Anisotropy In static samples or powdered solids, the orientation of the electron g-tensor and hyperfine tensor relative to the laboratory frame strongly affects the spin dynamics. Most existing models simplify this by assuming isotropic couplings or ignoring this, yet orientation effects are often critical to the outcome.

Simulations routinely show that enhancements vary widely across different crystal orientations, that powder patterns can exhibit strong asymmetries, and that the relative phase between the pulse sequence and hyperfine tensor can determine the sign or magnitude of the enhancement. Capturing these effects requires a model that respects the full anisotropic hyperfine geometry and tracks the spin dynamics for arbitrary orientations. In particular, one must describe how an ensemble of spins with different spatial alignments evolves under a given pulse sequence, and be able to compute ensemble averages.

Time–Frequency Duality and the Need for Spectral Decomposition In pulsed DNP, the role of frequency is more nuanced than in CW-DNP. Rather than matching the carrier frequency to a transition, pulsed sequences involve modulation that generates sidebands and broad spectral content. Two pulses with the same average power may differ substantially in frequency content, and only specific components may contribute to polarization transfer.

The effective field experienced by the nuclear spin can differ dramatically from the nominal electron Rabi frequency. When MAS is included, an additional modulation from sample rotation introduces further complexity, compounding the time–frequency structure of the problem.

Existing models partially address this through Fourier analysis of the time-dependent Hamiltonian. An alternative—and potentially more intuitive—approach is to decompose the trajectory of the driven electron spin itself, and examine which components of that motion produce polarization. This shift from analyzing the Hamiltonian to analyzing the spin trajectory forms the conceptual basis for the approach developed in this thesis.

Limited Insight into Pulse Design Principles The practical design of pulsed DNP sequences remains largely empirical. Parameters such as pulse length, phase modulation scheme, chirp width, and repetition rate are typically optimized through trial-and-error rather than theory. It is unclear what makes one pulse better than another, or whether optimal pulses can be predicted from the system's spin dynamics or geometry.

Additionally, it remains unresolved whether pulses can be designed to selectively enhance specific transitions broadened by hyperfine anisotropy, or how one should balance pulse duration and delay with coherence times and relaxation rates. Without a predictive and intuitive model, pulse development remains inefficient and poorly transferable across systems.

Toward a Geometric and Intuitive Framework A central goal of this work is to move beyond abstract matrix evolution and develop a geometric, time-resolved picture of pulsed DNP. Under strong driving, the electron spin undergoes coherent motion on the Bloch sphere. This motion, in turn, modulates the hyperfine field experienced by the nuclear spin, resulting in a time-dependent interaction that drives polarization.

By treating this interaction as a trajectory through coupling space, one gains access to a more intuitive representation of spin transfer. Such a framework allows direct visualization of polarization pathways, reveals resonance conditions encoded in spin motion, and clarifies how preparation pulses (spin rotations) affect enhancement. It also makes it possible to identify orientation-selective behaviors geometrically, based on the alignment of the hyperfine tensor with respect to the driven spin motion.

The remainder of this thesis develops this framework in detail, showing how electron spin trajectories under strong pulsed driving determine the frequency-domain content of the interaction and ultimately govern the polarization outcome. This trajectory-based model unifies several previously disconnected observations, and offers practical insight into the rational design of pulsed DNP sequences.

1.5 Goals and Scope of This Thesis

This thesis develops a unified theoretical and experimental framework for understanding and improving dynamic nuclear polarization (DNP) across multiple regimes of operation, with a primary focus on pulsed DNP under strong microwave driving. At the same time, it addresses several complementary directions—including Overhauser-based mechanisms in insulating solids, light-driven photo-DNP, and resonator and probe design for high-field operation—all of which contribute to the broader goal of enhancing solid-state NMR sensitivity in complex systems.

The central contribution lies in formulating a new approach to coherent polarization transfer in pulsed DNP. This work introduces a trajectory-based framework that models the electron spin's motion on the Bloch sphere under strong driving, and identifies how this motion modulates the hyperfine interaction in real time. By decomposing the spin trajectory in the frequency domain, the model captures resonant polarization pathways and explains enhancement trends across a variety of pulse types—including NOVEL, chirped pulses, and multi-phase modulation schemes. Orientation-selective effects and the function of preparation pulses are naturally incorporated, offering geometric insight into anisotropic transfer and pulse design.

Experimentally, this thesis presents a systematic evaluation of pulsed DNP sequences, including TPPM, XiX, TOP, tested under static solid conditions at 51 MHz / 34 GHz. Each pulse family is characterized through detailed parameter sweeps, contact time studies, and polarization buildup experiments. Orientation control via preparation pulses is also demonstrated and interpreted using the trajectory formalism.

In addition to pulsed methods, a separate investigation is presented on Overhauser-based DNP in insulating solids. This includes analysis of saturation behavior, field dependence, and the role of electron–nuclear hyperfine interactions. Another investigation about a new mechanism, tentatively termed "resonant mixing," is proposed and supported through experimental data and simulations.

Finally, the thesis includes the design, simulation, and initial testing of a custom high-field probe compatible with 263 GHz microwave irradiation. New strategies are explored for coupling microwave power into MAS or static samples with minimal losses, and challenges in waveguide layout, sample positioning are addressed.

Together, these studies form a comprehensive picture of how DNP can be enhanced, manipulated, and extended to new experimental regimes. The combined results offer both explanatory depth and practical tools for improving polarization transfer in high-field NMR and related spectroscopies.

Chapter 2

Pulsed DNP Sequences

Recently, we proposed a new mechanism to mediate dynamic nuclear polarization (DNP), resonant mixing (RM), that originates from state mixing induced by microwave irradiation near the EPR frequency. It was derived by considering the evolution of the density matrix for a simple electron–nucleus coupled spin pair in the presence of weak microwave irradiation, but the calculation did not include relaxation. In this manuscript, we present a theoretical model to describe the RM mechanism and its relation to Overhauser effect (OE) DNP in insulating solids. With the incorporation of relaxation, we calculate the static nuclear polarization produced by continuous wave microwave irradiation using Bloch theory. Both RM and OE depend on electron-nuclear cross-relaxation rates, and we find that the theoretical and experimental results suggest that RM can transition to the Overhauser effect (OE) DNP . When the zero-quantum (ZQ) and double-quantum (DQ) cross-relaxation rates are equal, a dispersive RM Zeeman field profile is observed, and when they differ a positive or negative absorptive Zeeman profile is expected, which by definition is OE DNP.

2.1 Introduction

Dynamic nuclear polarization (DNP) enhances nuclear spin polarization by transferring spin order from electrons to nearby nuclei, offering substantial sensitivity improvements in NMR spectroscopy. In the solid state, DNP has become a useful technique for studying biomolecular assemblies, functional materials, and surfaces. Most established implementations rely on continuous-wave microwave irradiation in combination with magic-angle spinning (MAS) to enable efficient polarization transfer. However, pulsed DNP methods have emerged as versatile alternatives, offering selective transfer pathways, broadband excitation profiles, less sample heating with a smaller average power. Combined with carefully engineered pulse sequences, pulsed DNP is expected to maintain its efficiency at high magnetic fields and

Several pulsed sequences, including NOVEL[47], TOP[42], XiX[43], BEAM[45], TPPM[44], and ASE[48–50], have been developed to engineer polarization transfer under strong, time-dependent electron spin driving. These sequences create dynamic spin transfer pathways that depend sensitively on pulse parameters and interaction profile. A range of theoretical approaches, including average Hamiltonian theory and Floquet analysis, have been used to describe the underlying physics. More recently, single-spin vector effective Hamiltonian

theory (SSV-EHT) [45, 51–53] have been proposed to capture the time dependence of spin dynamics, providing more intuitive insight into when and how polarization transfer occurs under pulsed conditions.

In this work, we test and extend this recently proposed SSV-EHT framework for understanding polarization transfer under strong pulsed driving. This model suggests that transfer efficiency can be understood from the frequency content of the electron spin dynamics during the pulse sequence. Building on this idea, we introduce a new approach for achieving better DNP enhancement in static solids by controlling the initial spin direction, and propose a strategy for interpreting powder patterns based on spin trajectory behavior. To evaluate and demonstrate these concepts, we perform a systematic experimental study of three pulsed DNP sequences—TPPM, XiX, and TOP—on a model system. Experiments are conducted at 1.2 T/34 GHz/51 MHz on OX063 radicals within a glycerol-water glassy matrix at 80 K. TPPM is analyzed in greatest detail, including a full parameter scan, contact time optimization, preparation-pulse sweeps to resolve the principal transfer axis, and Landau-Zener-style adiabatic transfer over changing pulse phase or duration. XiX and TOP are studied through parameter optimization and transition mapping via pulse and delay variations. Finally, the adiabatic Solid Effect is included as a comparison under matched conditions. These experiments confirm the key predictions of the theory, and establish new insight for pulse sequence analysis, simulation and design in static solid-state DNP.

2.2 Theory

2.2.1 Overview

The single-spin vector effective Hamiltonian theory (SSV-EHT), initially introduced in the context of solid-state NMR recoupling[51, 52], applies naturally to pulsed DNP sequences as well, offering an intuitive framework for interpreting driven electron spin dynamics and their role in polarization transfer[45, 53].

2.2.2 Driven Spin Dynamics

We consider a coupled spin system consisting of a single electron spin-$\frac{1}{2}$ and a single nuclear spin-$\frac{1}{2}$, placed in a static magnetic field along the z-axis. A strong, time-dependent transverse driving field is applied to the electron spin. In the rotating frame defined by the microwave carrier frequency ω_{MW}, the Hamiltonian takes the form

$$H(t) = \Omega S_z - \omega_n I_z + \mathbf{S} \cdot \mathbf{A} \cdot \mathbf{I} + H_{\mathsf{drive}}(t), \tag{2.1}$$

where $\Omega = \omega_e - \omega_{\mathsf{MW}}$ is the electron detuning, $-\omega_n$ is the nuclear Larmor frequency, $\mathbf{A}$ is the hyperfine interaction tensor, $\mathbf{S}$ and $\mathbf{I}$ denote electron and nuclear spin operators, respectively. The transverse driving field is given by

$$H_{\mathsf{drive}}(t) = 2\omega_{1S}(t) \left[\cos\phi(t)\, S_x + \sin\phi(t)\, S_y\right], \tag{2.2}$$

where both amplitude $\omega_{1S}(t)$ and phase $\phi(t)$ may vary in time.

To isolate the influence of the hyperfine interaction under strong electron driving, assuming $\mathrm{Tr}(\mathbf{A})^2 \ll \Omega^2 + \omega_{1S}^2$, we move to the interaction picture defined by the electron-only Hamiltonian

$$H_0(t) = \Omega S_z + H_{\mathsf{drive}}(t), \quad U_0(t) = \mathcal{T} \exp\left(-i \int_0^t H_0(t')\, dt'\right), \tag{2.3}$$

yielding the interaction-picture Hamiltonian:

$$\widetilde{H}(t) = -\omega_n I_z + U_0^\dagger(t)\, (\mathbf{S} \cdot \mathbf{A} \cdot \mathbf{I})\, U_0(t). \tag{2.4}$$

Since $H_0(t)$ acts only on the electron, the nuclear Zeeman term remains static. The time dependence arises solely from the transformation of the electron spin operators, expressed as:

$$U_0^\dagger(t)\, \mathbf{S}\, U_0(t) = \mathbf{R}(t)\, \mathbf{S}, \tag{2.5}$$

where $\mathbf{R}(t)$ is a real, time-dependent rotation matrix. This allows us to write:

$$\widetilde{H}(t) = -\omega_n I_z + \mathbf{S}^\top\, \mathbf{R}^\top(t)\, \mathbf{A}\, \mathbf{I}. \tag{2.6}$$

Expanding this in terms of spin raising and lowering operators, we can isolate the terms responsible for polarization exchange:

$$V(t) = \alpha(t) S_+ I_- + \alpha^*(t) S_- I_+ + \beta(t) S_+ I_+ + \beta^*(t) S_- I_-, \tag{2.7}$$

with coefficients defined by proper projection tensors $\mathbf{T}$:

$$\alpha(t) = \sum_{\mu,\nu} \left(\mathbf{T}_{\mu\nu}^{(+,-)}\right)^* \left[\mathbf{R}^\top(t)\mathbf{A}\right]_{\mu\nu}. \tag{2.8}$$

$$\beta(t) = \sum_{\mu,\nu} \left(\mathbf{T}_{\mu\nu}^{(+,+)}\right)^* \left[\mathbf{R}^\top(t)\mathbf{A}\right]_{\mu\nu}. \tag{2.9}$$

This interaction drives transitions in two independent two-level subspaces, the zero-quantum (ZQ) subspace, driven by $\alpha(t) S_+ I_- + \alpha^*(t) S_- I_+$, and the double-quantum (DQ) subspace, driven by $\beta(t) S_+ I_+ + \beta^*(t) S_- I_-$.

Starting from a polarized electron spin state, he ZQ transition frequency lies near the nuclear Larmor frequency $-\omega_n$, while the DQ transition is near ω_n. We isolate the dynamics by extracting the corresponding near-resonant Fourier components of $\alpha(t)$ and $\beta(t)$, denoted $\widetilde{\alpha} e^{i\omega_n t}$ and $\widetilde{\beta} e^{-i\omega_n t}$, respectively.

For now, we treat $\widetilde{\alpha}$ and $\widetilde{\beta}$ as constant amplitudes representing the dominant resonant contributions. The justification for this approximation–based on frequency selection and spectral filtering–will be given in the following section.

Assuming the electron is initially polarized with $\langle S_z(0) \rangle = \frac{1}{2} p_0$, and the nuclear spin is unpolarized, the polarization dynamics reduce to two independent driven two-level systems in the proton rotating frame:

$$H_{\mathrm{ZQ}} = \begin{bmatrix} 0 & \widetilde{\alpha} \\ \widetilde{\alpha}^* & 0 \end{bmatrix}, \quad H_{\mathrm{DQ}} = \begin{bmatrix} 0 & \widetilde{\beta} \\ \widetilde{\beta}^* & 0 \end{bmatrix}. \tag{2.10}$$

The initial population imbalance in each subspace is p_0, but each accounts for only half the total Hilbert space. Note that the rotation commutes withI_z, meaning that $\langle I_z \rangle$ is preserved. The resulting contributions to nuclear polarization are

$$\Delta P_I^{(\mathrm{ZQ})}(t) = \frac{p_0}{2} \sin^2 \left(|\widetilde{\alpha}|t\right), \quad \Delta P_I^{(\mathrm{DQ})}(t) = -\frac{p_0}{2} \sin^2 \left(|\widetilde{\beta}|t\right), \tag{2.11}$$

and the total change is

$$\Delta P_I(t) = \frac{p_0}{2} \left[\sin^2 \left(|\widetilde{\alpha}|t\right) - \sin^2 \left(|\widetilde{\beta}|t\right)\right]. \tag{2.12}$$

This expression captures coherent polarization transfer from a partially polarized electron to the nucleus, governed by the resonant zero- and double-quantum components of the modulated Hamiltonian.

2.2.3 Frequency Domain Analysis

We now analyze the structure of the rotating-frame hyperfine Hamiltonian in the frequency domain. As derived in the last section, the interaction-picture Hamiltonian takes the form:

$$\widetilde{H}(t) = -\omega_n I_z + \mathbf{S}^\top \mathbf{R}^\top(t)\, \mathbf{A}\, \mathbf{I}. \tag{2.6}$$

where $\mathbf{R}(t)$ is the time-dependent rotation matrix associated with the electron-only propagator $U_0(t)$, defined via:

$$U_0^\dagger(t)\, \mathbf{S}\, U_0(t) = \mathbf{R}(t)\, \mathbf{S} \tag{2.5}$$

Even in the special case that $H_0(t)$ is periodic, the resulting rotation matrix $\mathbf{R}(t)$ is not necessarily periodic. This stems from the fact that $H_0(t)$ generally does not commute with itself at different times:

$$[H_0(t), H_0(t')] \neq 0, \tag{2.13}$$

so the propagator $U_0(t)$ must be evaluated using a Dyson series. Consequently, $U_0(t)$ may accumulate a net rotation over time, and $\mathbf{R}(t)$ fails to be strictly periodic. In the framework of Average Hamiltonian Theory (AHT), this accumulated rotation is described by an effective field ω_{eff}), which acts as a static field generating the long-time precession of the electron spin.

We take another approach by performing a Fourier analysis of the time-dependent matrix $\mathbf{R}(t)$, as it is crucial for identifying the frequency components that mediate polarization transfer. Moreover, in the practical case of piecewise constant microwave pulses, $\mathbf{R}(t)$ can be easily simulated.

The Fourier transform of $\mathbf{R}(t)$ is given by:

$$\widetilde{\mathbf{R}}(\omega) = \int_{-\infty}^{\infty} \mathbf{R}(t) e^{-i\omega t} dt. \tag{2.14}$$

Since $\mathbf{R}(t)$ is a real rotation matrix, its Fourier transform is even:

$$\widetilde{\mathbf{R}}(\omega) = \widetilde{\mathbf{R}}(-\omega). \tag{2.15}$$

This allows us to isolate the relevant frequency components at the nuclear Larmor frequency ω_n for polarization transfer. As defined in Section 2.1, $\tilde{\alpha}$ corresponds to the resonant component of $\alpha(t)$ at $-\omega_n$, and $\tilde{\beta}$ corresponds to the resonant component of $\beta(t)$ at ω_n.

We now express $\tilde{\alpha}$ and $\tilde{\beta}$ in terms of the Fourier transform components at ω_n:

$$\tilde{\alpha} = \sum_{\mu,\nu} \left(\mathbf{T}_{\mu\nu}^{(+,-)}\right)^* \left[\widetilde{\mathbf{R}}^\top(\omega_n)\mathbf{A}\right]_{\mu\nu} \tag{2.16}$$

$$\tilde{\beta} = \sum_{\mu,\nu} \left(\mathbf{T}_{\mu\nu}^{(+,+)}\right)^* \left[\widetilde{\mathbf{R}}^\top(\omega_n)\mathbf{A}\right]_{\mu\nu} \tag{2.17}$$

The immediate inference is that spin polarization transfer rate depends on the relative strength of $\widetilde{\mathbf{R}}^\top(\omega_n)$, which can be measured by the Frobenius norm of the matrix $\|\widetilde{\mathbf{R}}(\omega_n)\|_F$. Before we start numerical simulations, the key observation is that up to now the derivation relies on the only assumption that hyperfine coupling is weak enough not to mix electron spin states. This theory can be applied to arbitrary pulses, and in the special case of periodic pulses, it is equivalent to AHT methods in that $\mathbf{R}(t)$ now descirbes a precession. When AHT matching condition,

$$n\omega_n + k\omega_m + l\omega_{eff} = 0 \tag{2.18}$$

is fulfilled, the frequency term is also a maximum.

2.2.4 Spin Trajectory Analysis

The approach we use for analyzing polarization transfer retains the full time-dependence of the system and provides a more flexible framework for pulse design than conventional time-averaging methods. By explicitly incorporating the rotation matrix $\mathbf{R}(t)$, which encodes the modulation effects of the pulse sequence, the method allows direct connections between pulse parameters and polarization transfer outcomes.

Starting from a polarized electron spin state $\mathbf{S}(0) = S_z$, the time-dependent spin trajectory is defined as

$$\mathbf{S}(t) = \mathbf{R}(t)\mathbf{S}(0), \tag{2.19}$$

and the interaction-picture Hamiltonian becomes

$$\widetilde{H}(t) = -\omega_n I_z + \mathbf{S}(t)^\top \mathbf{A}\,\mathbf{I}. \tag{2.20}$$

By performing a Fourier analysis of $\mathbf{S}(t)$, we decompose its trajectory into frequency components. This reveals the characteristic spectral structure induced by the pulse sequence and initial condition, and isolates the resonant frequencies responsible for polarization transfer.

Figure 2.1(a) shows the simulated trajectory $\mathbf{S}(t)$ under a model TPPM pulse, calculated using the SPINEVOLUTION package. First, the evolution is nearly identical when the hyperfine coupling is omitted, confirming that the trajectory is governed by the electron Hamiltonian alone. This validates the use of our home-written code, which neglects the hyperfine term. Second, the simulated $\mathbf{S}(t)$ remains confined to the unit Bloch sphere, further confirming that the hyperfine interaction is weak. The accumulated rotation from non-commuting pulse segments is clearly visible in the curved path traced on the sphere.

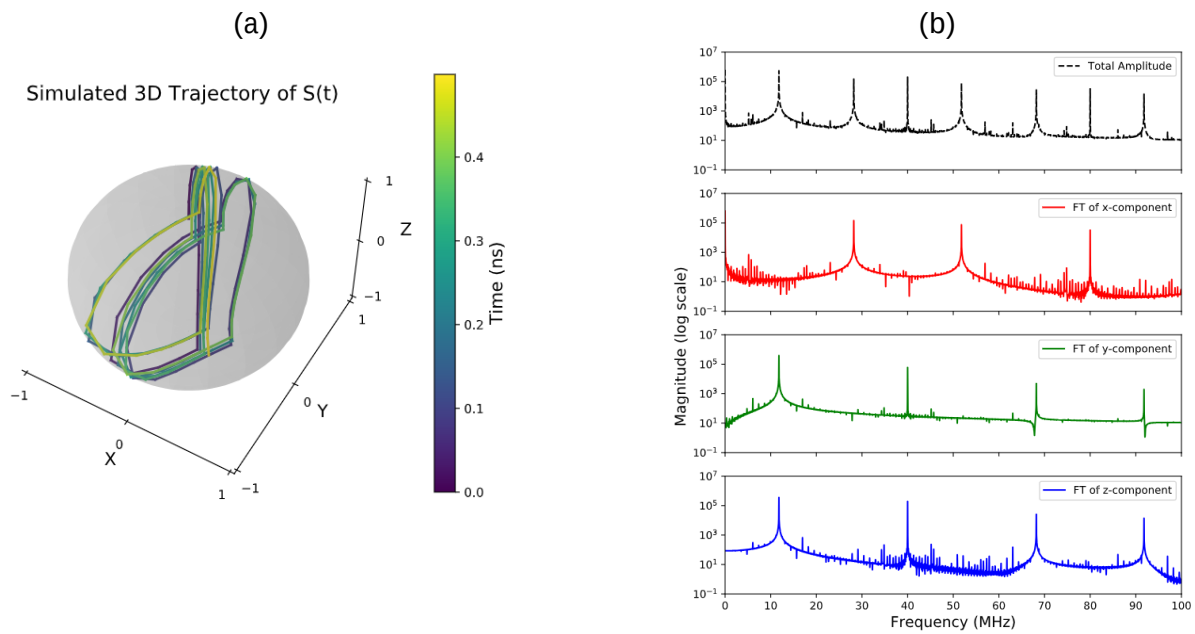

Figure 2.1: (a) SPINEVOLUTION simulated trajectory of a model TPPM pulse and (b) home-written code simulated power spectrum.

Figure 2.1(b) shows the power spectrum of $\mathbf{S}(t)$, computed using a home-written simulation without hyperfine coupling, consistent with results from the SPINEVOLUTION simulation. A distinct peak appears near 51 MHz, corresponding to the proton Larmor frequency ω_n. This indicates that the driven electron spin develops a frequency component capable of resonantly coupling to the proton, enabling polarization transfer.

This method provides a direct, visual picture of the driven electron spin dynamics, making it possible to interpret pulse sequences intuitively—without relying on time-averaged or perturbative approximations. This greatly aids pulse design by revealing how specific modulations drive the trajectory $\mathbf{S}(t)$ and its frequency content. For example, the strongest power component emerges when $\mathbf{S}(t)$ executes a uniform circular motion along a great circle of the Bloch sphere, resonant with the nuclear Larmor frequency, consistent with the NOVEL mechanism.

Orientation-Selective Enhancement via Preparation Pulse

The spin trajectory $\mathbf{S}(t) = \mathbf{R}(t)\,\mathbf{S}(0)$ offers a visually intuitive framework for identifying resonant driving conditions based on the motion of the electron spin. However, this method does not fully characterize polarization transfer unless the hyperfine tensor $\mathbf{A}$ is known. In systems with unknown or distributed couplings—as in powder samples or disordered environments—the trajectory alone cannot predict whether the oscillatory components of $\mathbf{S}(t)$ couple effectively to the nuclear spin.

This limitation motivates a complementary strategy based on controlling the initial condition $\mathbf{S}(0)$ through a single preparation pulse. By adjusting the orientation of the spin prior to the pulse train, one can directly modulate the amplitude of transfer without requiring

prior knowledge of $\mathbf{A}$. This approach enables empirical optimization of DNP efficiency and provides a practical handle for exploring effective polarization conditions in complex systems.

The prep-pulse is usually implemented as a single rotation

$$\hat{U}_{\mathsf{prep}} = e^{-i\theta\,\mathbf{n}\cdot\mathbf{S}}, \tag{2.21}$$

where $\mathbf{n}$ is a unit vector specifying the axis of rotation and θ the angle. Acting on the initial spin vector $\mathbf{S} = (S_x, S_y, S_z)^\top$, this produces

$$\mathbf{S}'(0) = \mathbf{R}_{\mathsf{prep}}\,\mathbf{S}, \tag{2.22}$$

where $\mathbf{R}_{\mathsf{prep}}$ is the rotation matrix corresponding to $\hat{U}_{\mathsf{prep}}$ under conjugation of operators.

The resulting spin vector evolves under the pulse train as

$$\mathbf{S}'(t) = \mathbf{R}(t)\,\mathbf{S}'(0), \tag{2.23}$$

steering the trajectory into regimes that enhance polarization transfer.

To clarify the effect of the prep-pulse, we define the spin trajectory as

$$\mathbf{S}'(t) = \mathbf{R}'(t)\,\mathbf{S}, \quad \text{where} \quad \mathbf{R}'(t) = \mathbf{R}(t)\,\mathbf{R}_{\mathsf{prep}}. \tag{2.24}$$

This treats the prep-pulse and the pulse train as a single time-dependent transformation of the initial spin vector. The interaction-picture Hamiltonian becomes

$$\widetilde{H}(t) = -\omega_n I_z + \mathbf{S}^\top\,\mathbf{R}'(t)^\top\,\mathbf{A}\mathbf{I}. \tag{2.25}$$

This form shows that the prep-pulse modifies the frame in which the hyperfine tensor is sampled, thereby controlling which components of $\mathbf{A}$ contribute to the transfer process. When $\mathbf{R}(t)$ is known or simulated, the spin trajectory $\mathbf{S}'(t)$ is determined for any prep-pulse, allowing one to infer features of $\mathbf{A}$ by correlating transfer efficiency with prep-pulse direction. In the case of NOVEL, the prep-pulse is typically chosen such that the transformed hyperfine interaction $\mathbf{R}'(t)^\top\mathbf{A}$ has maximal spectral power in the zero-quantum transfer channel S_+I_- at frequency ω_n, enabling coherent driving of the dominant polarization pathway. More generally, varying the prep-pulse allows one to effectively rotate the hyperfine tensor $\mathbf{A}$ while keeping the electron g-frame fixed, enabling orientation-selective exploration of the transfer process.

2.2.5 Powder Averaging and MAS Integration

All experiments in this study were performed on frozen glassy matrices, where molecules are randomly oriented. This makes orientational averaging essential for any theoretical prediction to reflect measurable outcomes. In particular, polarization transfer depends sensitively on the relative orientation between the molecular hyperfine tensor and the trajectory of the driven electron spin. This necessitates a powder average, in which relevant quantities are averaged over all possible molecular orientations.

To quantify the efficiency of polarization transfer across this disordered ensemble, we define a scalar measure that captures the orientation-dependent strength and directionality of

spin transfer. From the two-level approximation in Section 2.1, the nuclear spin polarization evolves as:

$$\Delta P_I(t) = \frac{p_0}{2}\left[\sin^2(|\widetilde{\alpha}|t) - \sin^2(|\widetilde{\beta}|t)\right] \tag{2.26}$$

At short times, this simplifies to:

$$\Delta P_I(t) \approx \frac{p_0}{2}(|\widetilde{\alpha}|^2 - |\widetilde{\beta}|^2)t^2 \tag{2.27}$$

This motivates the definition of a transfer metric:

$$\mathcal{P} = |\widetilde{\alpha}|^2 - |\widetilde{\beta}|^2 \tag{2.28}$$

We compute its average over all directions in space. Specifically, we define the powder average as:

$$\langle \mathcal{P} \rangle = \frac{1}{4\pi}\int_0^{\pi} \sin\theta \, d\theta \int_0^{2\pi} d\phi \, \mathcal{P}(\theta, \phi) \tag{2.29}$$

To evaluate $\mathcal{P}(\theta, \phi)$, we use the rotation matrix $\mathbf{S}(\theta, \phi)$, which defines the orientation of the hyperfine tensor $\mathbf{A}(\theta, \phi)$ in the lab frame. For each orientation (θ, ϕ), the hyperfine tensor is rotated as follows:

$$\mathbf{A}(\theta, \phi) = \mathbf{S}^\top(\theta, \phi)\mathbf{A}_0\mathbf{S}(\theta, \phi) \tag{2.30}$$

Here, $\mathbf{A}_0$ is the hyperfine tensor in its principal axis frame. The Fourier component $\widetilde{\alpha}(\theta, \phi)$ is then determined by projecting the Fourier components of the rotation matrix $\mathbf{R}(t)$ onto the rotated hyperfine tensor.

Next, we compute the squared amplitude $|\widetilde{\alpha}(\theta, \phi)|^2$:

$$|\widetilde{\alpha}(\theta, \phi)|^2 = \left|\sum_{\mu,\nu} \left(\mathbf{T}^{(+,-)}_{\mu\nu}\right)^* \left[\widetilde{\mathbf{R}}^\top(\omega_n)\mathbf{S}^\top(\theta, \phi)\mathbf{A}_0\mathbf{S}(\theta, \phi)\right]_{\mu\nu}\right|^2 \tag{2.31}$$

The powder-averaged $|\widetilde{\alpha}|^2$ is then computed by integrating over all possible orientations:

$$\langle |\widetilde{\alpha}|^2 \rangle = \frac{1}{4\pi}\int_0^{\pi} \sin\theta \, d\theta \int_0^{2\pi} d\phi \, |\widetilde{\alpha}(\theta, \phi)|^2 \tag{2.32}$$

This integral can be performed numerically using spherical quadrature or Monte Carlo sampling. The result $\langle |\widetilde{\alpha}|^2 \rangle$ provides a simulable measure of the polarization transfer efficiency in a disordered sample. By repeating this procedure for $\widetilde{\beta}$, we obtain the powder-averaged transfer metric:

$$\langle \mathcal{P} \rangle = \langle |\widetilde{\alpha}|^2 \rangle - \langle |\widetilde{\beta}|^2 \rangle \tag{2.33}$$

This approach is fully simulable: for any given pulse sequence and hyperfine coupling tensor $\mathbf{A}_0$, one can compute the Fourier component $\widetilde{\mathbf{R}}(\omega_n)$ of the spin trajectory and evaluate the integrand numerically over the unit sphere. This makes it a practical and generalizable tool for theoretical DNP optimization in realistic systems.

Magic-angle spinning (MAS) introduces a time-dependent rotation of the molecular frame relative to the laboratory frame, continuously modulating the orientation of the hyperfine tensor. This effect is crucial for high-field NMR and Dynamic Nuclear Polarization (DNP) development, as it allows the effective averaging of dipolar interactions that would otherwise be too strong at high fields. By dynamically averaging the molecular orientations, MAS enables polarization transfer even in systems where static orientation would lead to inefficient coupling, significantly enhancing the potential for polarization under strong driving conditions.

MAS is captured by defining a time-dependent tensor:

$$\mathbf{A}_{\mathsf{MAS}}(t) = \mathbf{R}_{\mathsf{MAS}}^{\top}(t)\,\mathbf{A}(\theta,\phi)\,\mathbf{R}_{\mathsf{MAS}}(t) \tag{2.34}$$

where $\mathbf{R}_{\mathsf{MAS}}(t)$ describes uniform rotation about the rotor axis at angular frequency ω_r, typically set at the magic angle. Traditionally, MAS is viewed as a mechanism for orientation averaging, but in the present framework, it can be absorbed directly into the spin dynamics.

Or, we can treat MAS as an additional rotation acting on the driven spin trajectory. The combined spin evolution in the lab frame is given by the composite trajectory:

$$\mathbf{S}_{\mathsf{MAS}}(t) = \mathbf{R}_{\mathsf{MAS+pulse}}(t)\,\mathbf{S}(0) \tag{2.35}$$

Since MAS rotation and $\mathbf{R}(t)$ usually don't commute. The resulting trajectory captures the full lab-frame motion of the electron spin in the presence of both driving and mechanical spinning.

This composite trajectory is similarly used in the interaction Hamiltonian:

$$\widetilde{H}(t) = -\omega_n I_z + \mathbf{S}_{\mathsf{MAS}}(t)^{\top}\mathbf{A}_0\,\mathbf{I} \tag{2.36}$$

and allows the MAS effect to be incorporated without time-averaging. Instead, one directly computes the Fourier transform of $\mathbf{S}_{\mathsf{MAS}}(t)$ to extract $\widetilde{\alpha}$ and $\widetilde{\beta}$ in the presence of spinning.

This approach enables a unified treatment of strong driving and MAS. Moreover, it highlights the potential of rotor-synchronized pulse design—by tailoring the pulse sequence to the rotor phase, one can shape the composite trajectory $\mathbf{S}_{\mathsf{MAS}}(t)$ to maximize resonant coupling across a broad range of orientations, turning MAS into a possible tool for dynamic control rather than passive averaging.

2.2.6 Landau-Zener Transition

Recall the zero-quantum (ZQ) subspace formalism in Section 2.1, describes transitions where the electron and nuclear spins flip simultaneously. The interaction Hamiltonian in this frame is:

$$H_{\mathsf{ZQ}} = \omega_n I_z + \tilde{\alpha} e^{i\omega_n t} S_+ I_- + \tilde{\alpha}^* e^{-i\omega_n t} S_- I_+ \tag{2.37}$$

where $\tilde{\alpha}$ is the Fourier coefficient and ω_n is the nuclear Larmor frequency. This Hamiltonian governs the polarization transfer in the ZQ subspace.

Now suppose that interaction coefficient $\tilde{\alpha}$ has no component at the nuclear Larmor frequency ω_n, but it has a significant component at a nearby frequency $\omega_n - \delta$, where δ

represents a shift in the characteristic frequency. This shift affects the interaction between the electron and nuclear spins. The most important interaction coefficient $\tilde{\alpha}$ is now

$$\tilde{\alpha} = \sum_{\mu,\nu} \left(\mathbf{T}_{\mu\nu}^{(+,-)}\right)^* \left[\widetilde{\mathbf{R}}^\top(\omega_n - \delta)\mathbf{A}\right]_{\mu\nu} \tag{2.38}$$

The shift δ now modifies the Hamiltonian as:

$$H_{\mathsf{ZQ}} = \omega_n I_z + \tilde{\alpha} e^{i(\omega_n - \delta)t} S_+ I_- + \tilde{\alpha}^* e^{-i(\omega_n - \delta)t} S_- I_+ \tag{2.39}$$

To simplify the dynamics, we move to the nuclear detuned rotating frame by applying the unitary transformation $e^{-i(\omega_n - \delta)I_z t}$. This removes the time dependence from the Hamiltonian, resulting in the following effective Hamiltonian:

$$H_{\mathsf{ZQ,\ det}} = \delta I_z + \tilde{\alpha} S_+ I_- + \tilde{\alpha}^* S_- I_+ \tag{2.40}$$

The transformation removes the explicit time dependence of the system, leaving only the resonant interaction terms that drive the polarization transfer.

This form of the Hamiltonian has efficient spin transfer potential because it resembles the Landau-Zener form. In Dynamic Nuclear Polarization (DNP), the Landau-Zener transition has been a useful tool to efficiently transfer polarization between the electron and nuclear spins under the influence of external driving fields, such as Integrated Solid Effect or Adiabatic Solid Effect[49].

In Landau-Zener theory, the system is driven by a time-dependent detuning, which reduces the energy gap between the two states. As the gap approaches zero, the system undergoes a adiabatic transition, facilitating polarization transfer between the electron and nuclear spins. By engineering the pulse sequence such that $\delta(t)$ varies with time, the system is driven through resonance. For simplicity in theory, we assume a linear time dependence for $\delta(t)$, i.e., $\delta(t) = Q(t - t_0)$, but this is not a requirement.

In the nuclear detuned rotating frame, the Hamiltonian describing the interaction between the electron and nuclear spins is now:

$$H_{\mathsf{ZQ,\ det}} = \begin{pmatrix} \delta(t) & \tilde{\alpha} \\ \tilde{\alpha}^* & -\delta(t) \end{pmatrix} \tag{2.41}$$

For a two-level system governed by the interaction Hamiltonian, the Landau-Zener transition probability P_{LZ} is given by:

$$P_{\mathsf{LZ}} = \exp\left(-\frac{2\pi|\tilde{\alpha}|^2}{Q}\right) \tag{2.42}$$

where Q is the rate of change of the time-dependent detuning $\delta(t)$. This formula describes the probability of the system undergoing a Landau-Zener transition, resulting in polarization transfer between the electron and nuclear spins. The system undergoes a non-adiabatic transition, facilitating efficient polarization transfer.

Although the model simplifies the system with assumptions such as linear detuning and neglects effects like relaxation, it provides an intuitive starting point for efficient DNP pulse design. This theoretical framework provides a foundation for exploring polarization transfer

in experimental systems. The next step is to investigate its validity and implications in practical setups, which will be explored in the experimental section.

2.3 Methods

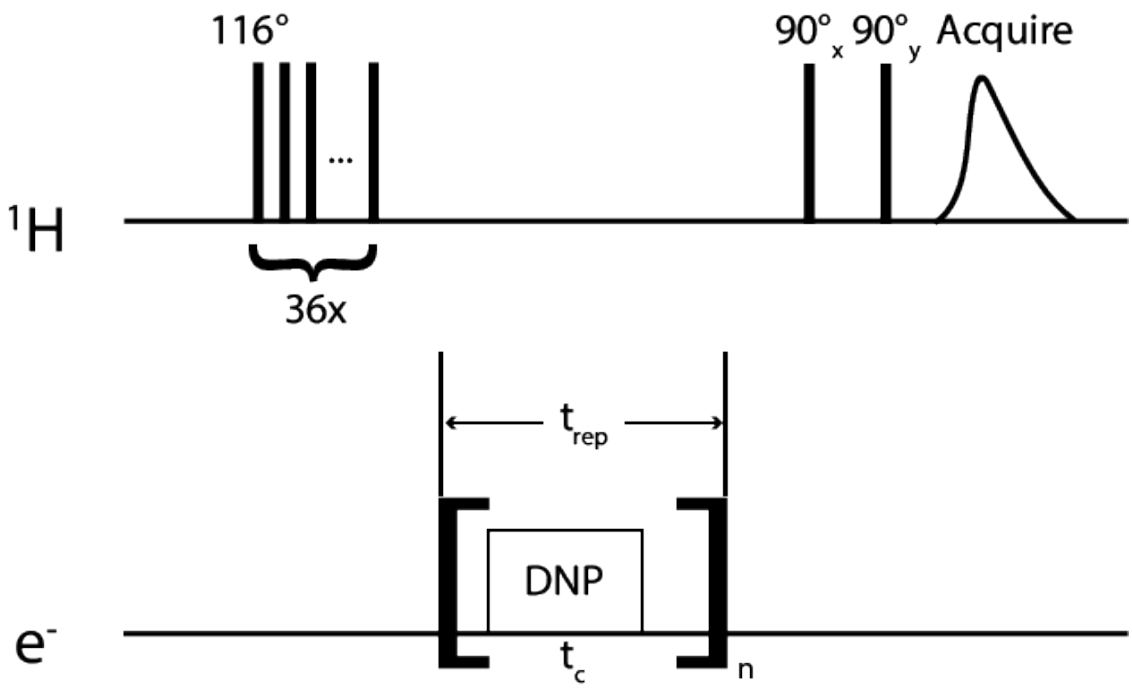

Figure 2.2: General pulse sequence used for all DNP experiments. Proton saturation was applied using a train of 36 pulses, followed by a solid echo detection. Microwave irradiation was applied periodically during the buildup time $t_b = n \times t_{\mathsf{rep}}$, with contact time t_{c}.

All experiments were performed on a static sample of 4.8 mM trityl OX063 dissolved in DNP juice (glycerol-d_8:D_2O:H_2O, 6:3:1 by volume), loaded into a 1 mm inner-diameter quartz EPR tube and placed inside a Bruker EN 5107D2 dielectric resonator. The trityl concentration was verified by UV-Vis spectroscopy. The sample was cooled to 80 K using a ColdEdge Stinger closed-cycle cryostat system coupled to an Oxford Instruments CF935O cryostat. Temperature regulation was provided by an Oxford ITC503 controller. The sample was snap-freezed and formed a homogeneous glassy matrix under these conditions.

Experiments were executed on a Bruker ELEXSYS E580 spectrometer equipped with a built-in arbitrary waveform generator (AWG). All measurements were carried out at Q-band ($B_0 = 1.2$ T), with electron and proton Larmor frequencies of $\omega_e = 34$ GHz and $\omega_p = 51$ MHz, respectively. Microwave irradiation was generated using a 50 W traveling-wave tube amplifier (TWT), and the nominal electron Rabi frequency was $\omega_{1S} = 2\pi \times 21$ MHz unless

otherwise stated. The center frequency was set to $\omega_{\mathsf{mw}} = 2\pi \times 33.745$ GHz and used as input to the AWG, with the actual output spectrum determined by the programmed pulse sequence. Pulse sequences were programmed using the Bruker Xepr interface with cross-system control handled via the Xepr Python API.

Proton NMR detection was performed using a home-built receiver channel. A solid echo sequence was used for all acquisitions, with a $\pi/2$ pulse length of 3.5 µs and dwell time of 10 µs. The repetition delay was set to $t_{\mathsf{rep}} = 10$ s unless otherwise stated. A saturation-recovery scheme was used throughout, as in Fig 2.2. Longitudinal relaxation times T_1 were independently measured and used to estimate enhancement factors.

Data were processed in MATLAB. Spectra were baseline-corrected. Enhancement values were calculated from the peak height relative to a reference signal acquired without microwave irradiation. This reference was averaged over 1024 scans to provide a high-SNR baseline for normalization. Each data point in DNP experiments was typically averaged over 4 or 8 scans, according to phase cycling schemes.

Sequence-specific parameters and variations for TPPM, XiX, and TOP are detailed in Sections 4.1–4.3.

2.4 Results and Discussion

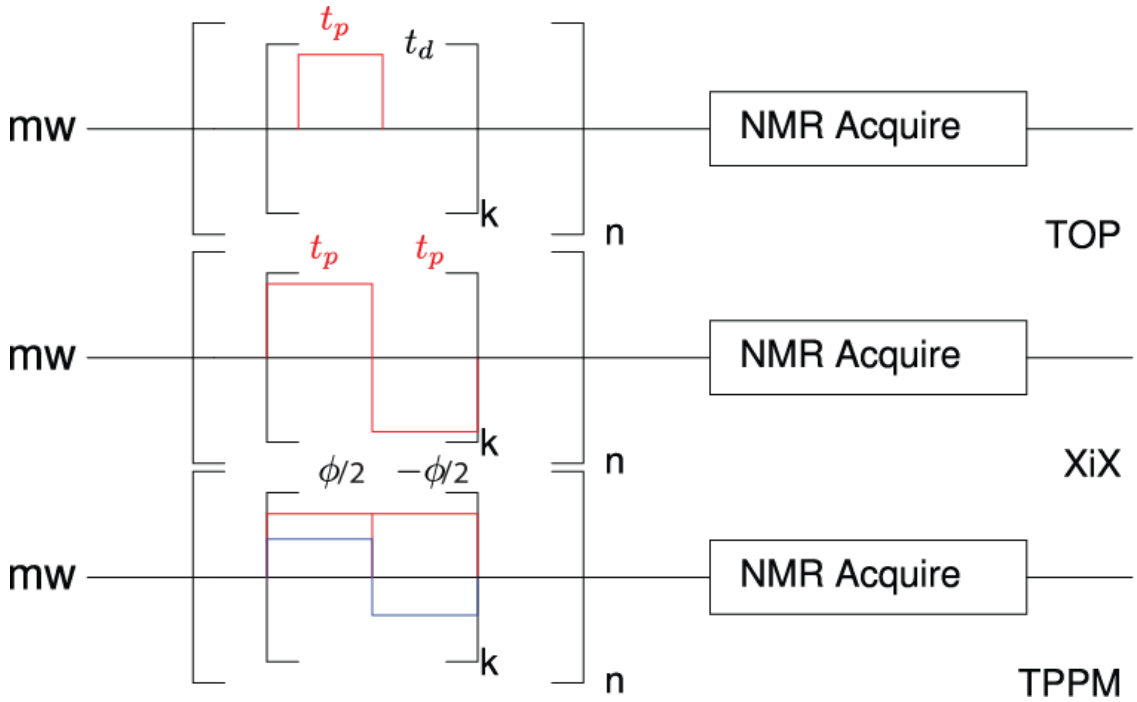

Figure 2.3: Schematics of basic TPPM, TOP and XiX sequences as used in the expriments.

2.4.1 TPPM

TPPM, originally developed for heteronuclear decoupling, consists of alternating-phase RF pulses repeated at fixed intervals. Recent work by Redrouthu *et al.* [44] demonstrated that TPPM can also drive DNP under static conditions by generating coherent spin dynamics . We adopt the new theoretical approach, using TPPM as a polarization-transfer sequence and exploring its behavior via systematic parameter scans.

Optimal TPPM Parameters

We performed a detailed parameter scan of the TPPM pulse sequence to investigate the conditions for optimal polarization transfer. The TPPM sequence consists of a train of phase-alternated pulses of fixed duration τ and phase offset $\pm\phi/2$, applied to the electron spin. For each combination of τ and ϕ, we recorded the resulting echo signals and extracted the polarization transfer by evaluating the peak area of the resulting NMR spectra. The final data were assembled into a two-dimensional matrix of peak heights as a function of pulse parameters.

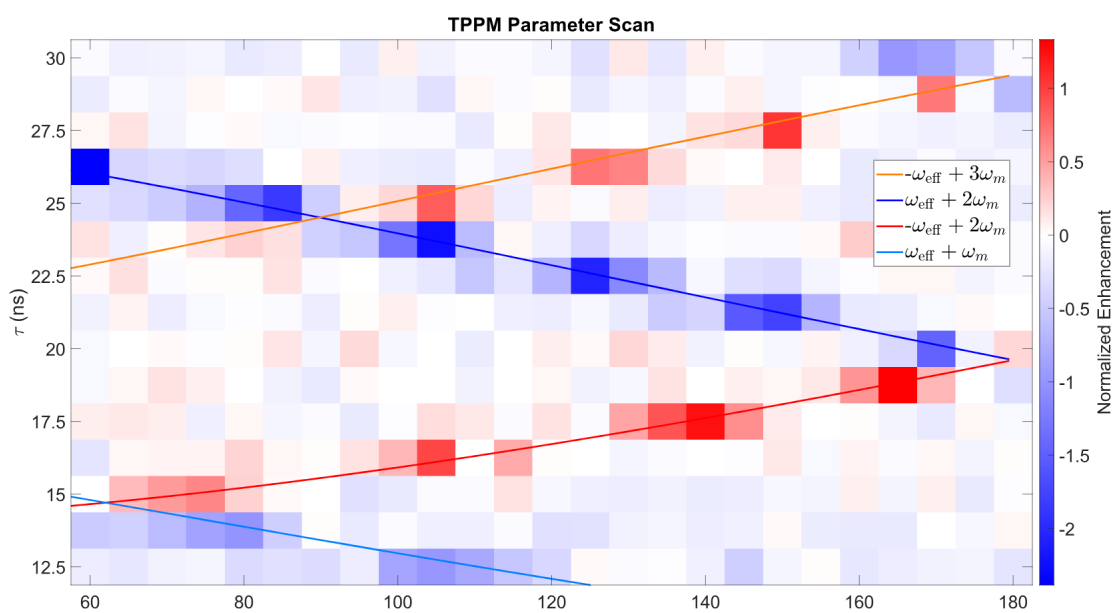

Figure 2.4: TPPM parameter scan showing peak heights as a function of pulse duration τ and phase ϕ. Blue and red lines indicate resonance conditions $\omega_{\text{e}\square} \pm k\omega_m = \omega_n$ for various integers k.

The resulting map, shown in Fig. 2.4, reveals broad resonance ridges and antiresonance troughs, indicative of constructive and destructive polarization transfer conditions for DQ and ZQ transitions. To interpret these features, we overlaid parametric contours derived from theoretical resonance conditions involving the effective frequency $\omega_{\text{e}\square}$ generated by the pulse train. Specifically, the blue and red lines in the figure correspond to solutions of the equations

$$\pm\omega_{\text{e}\square} + k\omega_m = \omega_n \tag{2.43}$$

for various integer k, where $\omega_m = \frac{1}{2\tau}$ is the modulation frequency set by the pulse sequence, and ω_n is the nuclear Larmor frequency. These lines align remarkably well with the features in the experimental map, validating the theoretical model and confirming that resonant spin trajectories underlie polarization transfer. In particular, the strongest enhancements occur at $\tau = 26.25ns$ and $\phi = 60°$, with a negative enhancement of -407. The precise trace of the lines reflect the nonlinear dependence of $\omega_{e\square}$ on both pulse duration and phase.

Improved Enhancement via Preparation Pulse

To investigate how the initial spin orientation affects polarization transfer, we implemented a systematic sweep of preparation pulses applied prior to the TPPM sequence. Each preparation pulse corresponds to a rotation of the electron spin vector, effectively altering the initial condition $\mathbf{S}'(0)$ on the Bloch sphere. Experimentally, we varied the pulse length from 0 to 12.5 ns in 1.25 ns steps and the pulse phase from 0° to 345° in 15° steps. These settings span a hemispherical grid of polar and azimuthal angles, allowing for a spatial scan of possible initial spin states.

The enhancement observed after TPPM recoupling exhibits a strong dependence on the orientation of $\mathbf{S}'(0)$. As shown in Fig. 2.5, the enhancement map features a well-defined peak at $\phi = 300°$, $\theta = 0.165\,\text{rad}$, corresponding to a prep-pulse of 1.25 ns. This configuration yields a 16% improvement in signal intensity compared to the case without a preparation pulse, up to around -460 times enhancement. Notably, the optimal axis for initial spin alignment does not coincide with the effective field direction $\boldsymbol{\omega}_{e\square}$, indicating that maximum transfer is not achieved by aligning with the driven precession axis alone. This highlights the importance of trajectory matching over the full spin evolution.

We note that the scan was limited to a single hemisphere under the initial assumption that the profile would be symmetric. The presence of a clear maximum suggests that a symmetric but inverted enhancement peak may exist on the opposite side of the Bloch sphere. This follows directly from the nature of the two-level transfer subspace, where inverting the initial spin orientation yields an enhancement of the same magnitude but opposite sign. However, we note two puzzling observations. First, the enhancement at the opposite pole (around $\phi = 60°$, $\theta \approx \pi - 0.165\,\text{rad}$, see Supporting Information) reaches only about 60% of the maximum value. This remain unexplained by the present trajectory-based model. Second, the microwave field strength ω_{1S} extracted from this profile corresponds to approximately 21 MHz, which is consistent with effective field simulations. However, this value is significantly lower than the 50 MHz value determined from EPR nutation measurements on the same instrument.

2.4.2 Adiabatic Spin Transfer via Chirped TPPM

To explore the role of adiabatic spin transfer in pulsed DNP, we extended the TPPM sequence by smoothly varying either the *pulse phase* or the *pulse duration* across the pulse train. This modulation transforms the effective electron spin trajectory into a chirped path in frequency space, designed to sweep through resonance with the nuclear spin. Such frequency-swept sequences mimic Landau-Zener transitions (see Section 2.2.6), offering an alternative to traditional adiabatic DNP schemes.

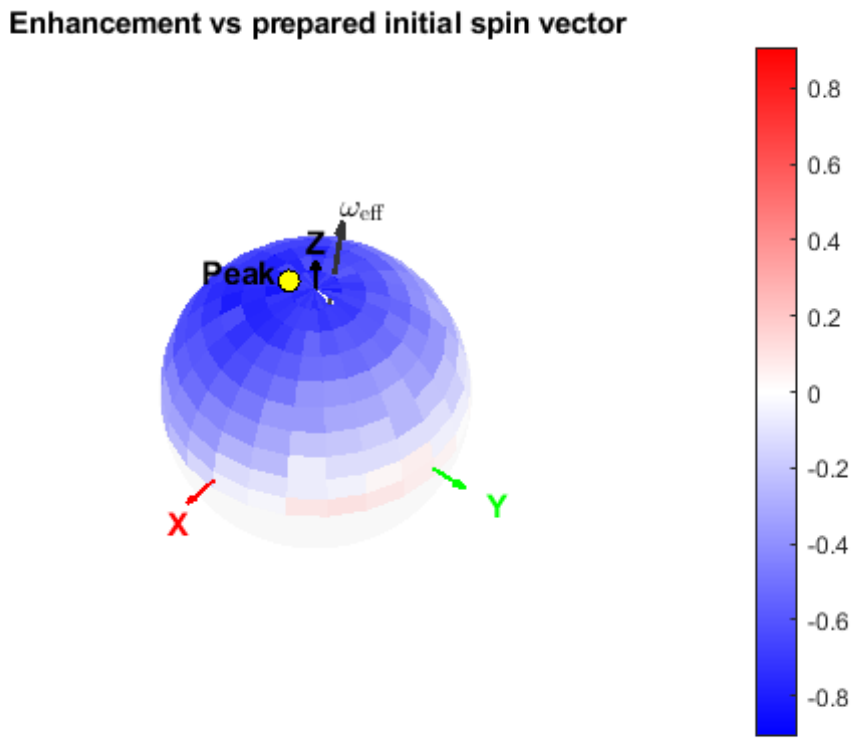

Figure 2.5: Enhancement as a function of preparation pulse angle and duration, visualized on the unit Bloch sphere. The maximum enhancement occurs near $\phi = 300°$, $\theta = 0.165\,\text{rad}$.

In the *phase-chirped TPPM*, we swept the phase offset $\phi(t)$ over the duration of the pulse train. In the *duration-chirped variant*, we modulated the pulse length $\tau(t)$, which alters both the modulation frequency $\omega_m = \frac{1}{2\tau(t)}$ and the effective rotation angle per cycle. Both strategies dynamically tune the effective detuning $\delta(t)$, enabling the system to cross through the nuclear Larmor frequency ω_n during the pulse train.

To test this, we constructed TPPM pulse trains with many segments, sweeping the phase offset from $\phi_{\text{start}} = \phi - \Delta\phi°$ to $\phi_{\text{end}} = \phi + \Delta\phi°$, while keeping τ fixed. The resulting trajectory $\mathbf{S}(t)$ undergoes a slow precession across different effective fields. Similarly, for duration-chirped TPPM, we held ϕ constant and swept τ from $\tau_{\text{start}} = \tau - \Delta\tau$ to $\tau_{\text{end}} = \tau + \Delta\tau$ over the same number of steps. The sweep trace is tangent shape, and the exact sweep shape is defined by the sweep parameter t_{co} (See Fig. 2.6). For example in the phase sweep, the parameter guides the sweep by the tangent formula given by [54]:

$$\delta\phi(t) = \frac{\Delta\phi}{2} \cdot \frac{\tan\left(\frac{2 \cdot t - t_c}{t_c} t_{\text{co}}\right)}{\tan(t_{\text{co}})}$$

In practice, The phase is calculated for each individual pulse, but the number of pulses is large enough to mimic a continuous sweep with discrete steps.

Previous theoretical analysis is based on linear chirp with constant frequency coeffi-

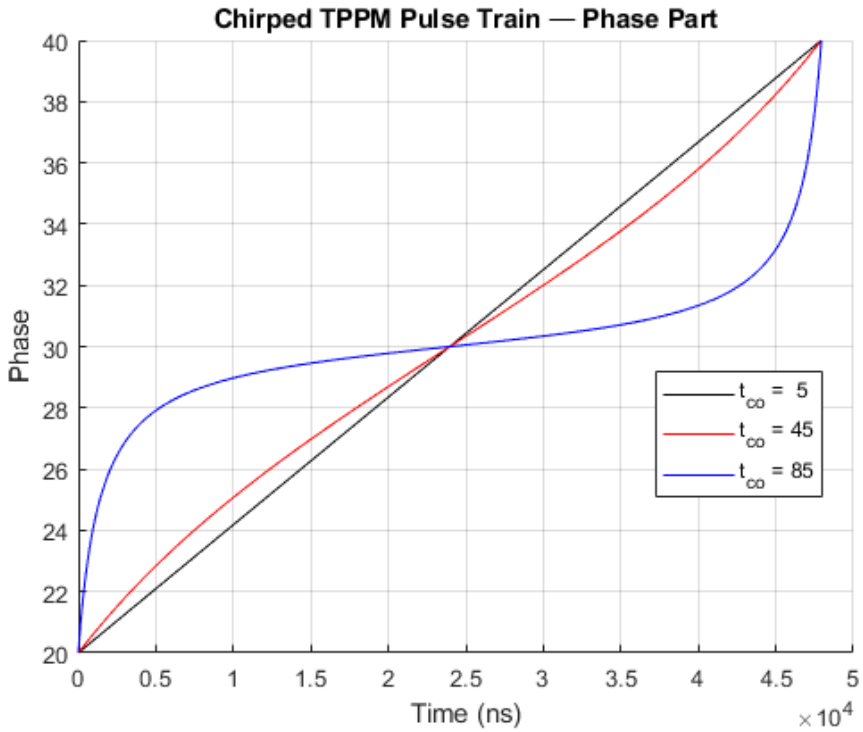

Figure 2.6: An example TPPM phase chirp from $\phi_{\mathsf{start}}/2 = 20°$ to $\phi_{\mathsf{end}}/2 = 40°$. Parameter $t_{co} = 5$ is almost linear, while $t_{co} = 85$ is flatter at the center.

cients [45]. While these two conditions are not met in the experimental setup, a key parameter that is crucial to polarization transfer is the "chirp rate". For example in the frequency chirp shown in Fig. 2.7, the sweep rate of diagonal term, the offset frequency is about 4 MHz over a pulse length of 50 µs. Using the linear Landau-Zener formula, and estimating the hyperfine coupling to be around 1 MHz:

$$P_{\mathsf{LZ}} = \exp\left(-\frac{2\pi|\tilde{\alpha}|^2}{d\delta/dt}\right) \tag{2.44}$$

The LZ transition is estimated to be quite efficient. But with a pulse length chirp the rate of change of detuning δ is too fast, and we expect LZ-transition to be not as efficient.

We tested chirped pulses based on two base TPPM sequences, the positive max at $\tau = 17.5ns$ and $\phi = 140°$ and the negative max at $\tau = 26.25ns$ and $\phi = 60°$. As shown in Fig. 2.8, phase-chirped protocols yield significant DNP enhancement, with maximal transfer observed when the $\Delta\phi = 10°$ parameters is chosen. The enhancement is improved around 55%, up to an enhancement factor of 488, The negative max also had a modest improvement of 12%. Meanwhile, the length-chirped variants only lead to decreased enhancement. This result supports the idea that a slowly varying $\delta(t)$ in the driven frame can steer the system through an avoided crossing in the spin subspace, yielding irreversible polarization buildup.

Compared to the unmodulated TPPM case, chirped TPPM achieves greater enhancements under matched average power. Importantly, the enhancement should be less sensitive to the precise choice of phase or duration, indicating a greater robustness to parameter

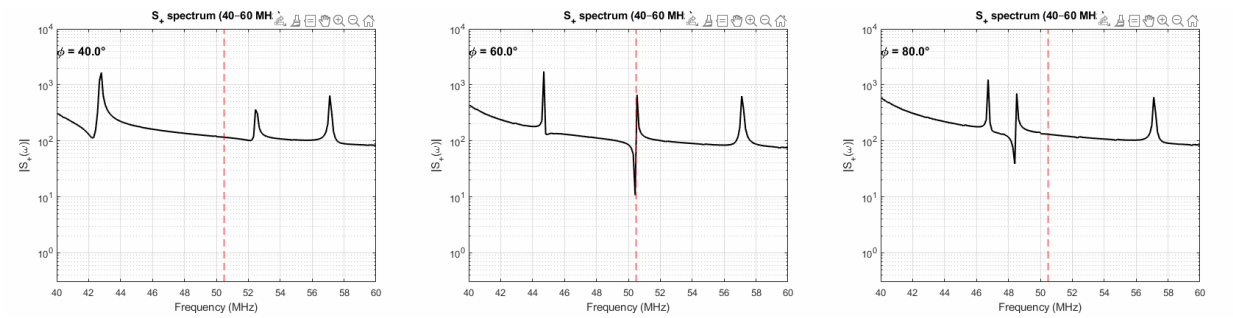

Figure 2.7: Frequency shift from $\phi_{\mathsf{start}} = 40°$ to $\phi_{\mathsf{end}}/2 = 80°$. Note the shift of characteristic frequency across nuclear Larmor frequency.

fluctuations—one of the hallmarks of adiabatic schemes. This suggests that Landau-Zener-style control of the spin trajectory can serve as a general principle for pulsed DNP optimization, even when implemented through nontraditional means such as phase-modulated TPPM.

2.4.3 TOP

The TOP sequence, originally developed for solid-state NMR decoupling, consists of a series of short, high-power pulses interleaved with adjustable free-evolution delays. In the context of DNP, the sequence has been proposed to exploit coherent spin transfer through structured electron spin modulation[42]. Unlike TPPM, which alternates the phase of identical pulses, TOP introduces a tunable delay between pulses that enables control over the timing and phasing of effective field modulation.

We implemented the TOP sequence using a train of pulsest_p ranging from 1.25 to 20 ns, separated by interpulse delays t_d in the same range, with 48 µs total length. As in TPPM, the pulses alternate to maintain periodicity, but the key feature of TOP is the use of a constant, nonzero delay between pulse segments. This introduces a distinct frequency modulation that allows the electron spin trajectory to visit specific frequency on the Bloch sphere in a controlled fashion.

To evaluate the performance of TOP, we performed a two-dimensional scan over pulse length t_p and delay length t_d, extracting the DNP enhancement from the resulting NMR signals. The results at microwave offset -92 MHz is shown in Fig. 2.9, reveal a set of resonant ridges aligned with theoretical transfer conditions, analogous to those observed for TPPM. These ridges correspond to combinations of t_p and t_d for which the effective frequency of the modulated spin trajectory matches the nuclear Larmor frequency ω_n. The near-linear behavior is due to the commutator of the electron spin vector rotations is significantly smaller than the rotation themselves. The maxima is found at $t_p = 18.75ns$ and $t_d = 12.5ns$. As we scan through several different offsets, another maxima is found for microwave offset -52 MHz at $t_p = 12.5ns$ and $t_d = 15ns$ (See Supporting Information).

Although the overall enhancement from TOP is modest compared to optimized TPPM (See table , the results confirm that frequency-tuned transfer is possible using delay-modulated sequences. Enhancement maxima align with conditions where the effective spin precession frequency $\omega_{\mathsf{e}\square}$ satisfies:

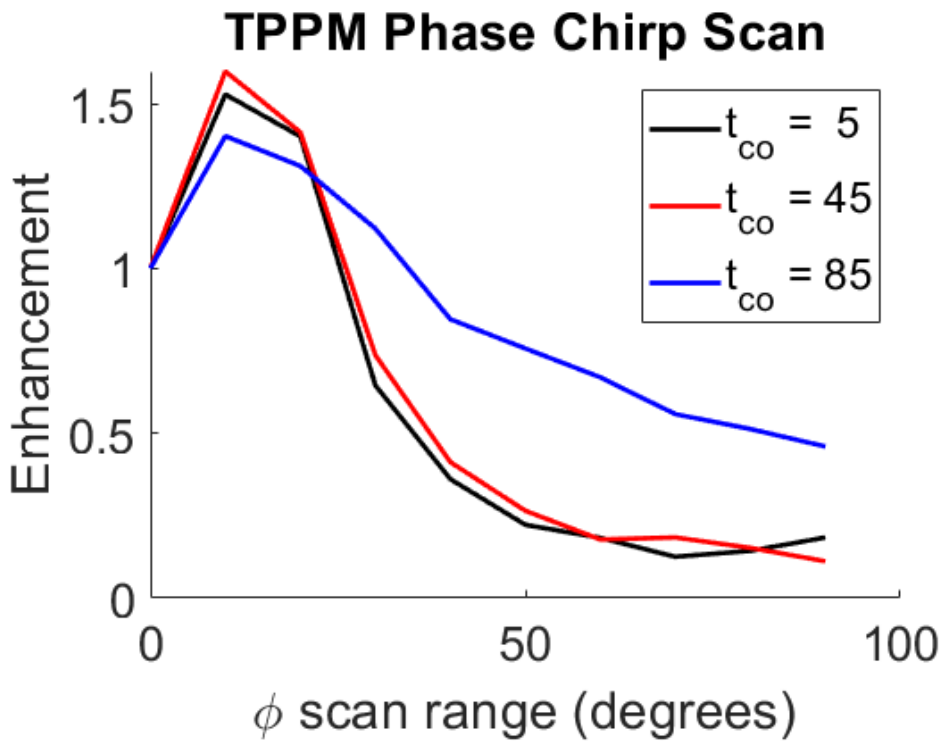

Figure 2.8: TPPM at positive max, $\tau = 17.5ns$ and $\phi = 140°$, with phase chirps. A significant improvement is found.

$$\pm\omega_{e\square} + k\omega_m = \omega_n, \tag{2.45}$$

where $\omega_m = \frac{1}{\tau+\Delta}$ is the base modulation frequency of the pulse cycle.

Interestingly, the enhancement landscape of TOP is less sharply structured than that of TPPM, instead exhibiting a broad enhancement ridge over a range of parameters. This suggests that the TOP sequence is more sensitive to intrinsic sample properties such as hyperfine coupling strength and g-tensor anisotropy. Under this interpretation, different resonance bands within the TOP map may correspond to distinct coupling regimes present in the sample, each becoming active under slightly different timing conditions. The broadness of the enhancement ridge implies that the effective matching frequency of TOP is less sensitive to small variations in pulse parameters, in contrast to the sharper, more selective resonances seen in TPPM.

This relative insensitivity, however, has a beneficial consequence. Because the effective frequency evolves more gradually, sweeping parameters such as the pulse length t_p or interpulse delay t_d across the pulse train results in a slow adiabatic traversal of resonance conditions. In effect, chirped versions of TOP perform a Landau-Zener-style passage through the effective spin coupling landscape, enabling greater net polarization transfer. Experimental results confirm this hypothesis: chirped TOP sequences consistently yield higher enhancements than their unmodulated counterparts, with up to 99% improvement observed under optimized sweep conditions.

Surprisingly, this trend does not hold for all parameter regimes. For instance, in the

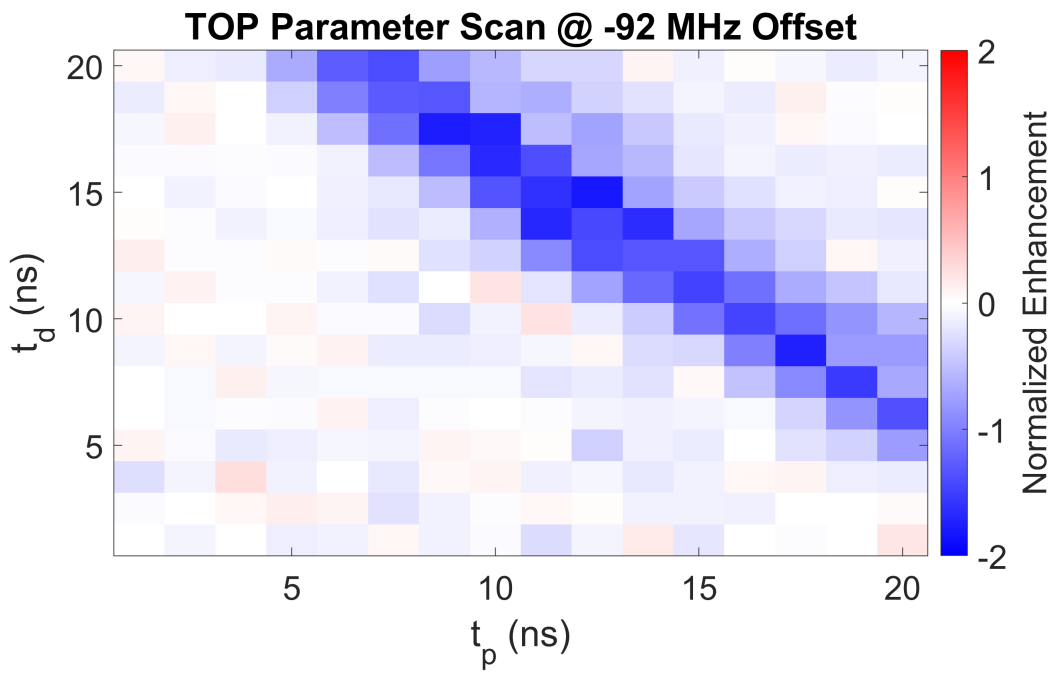

Figure 2.9: TOP parameter scan showing NMR instensity as a function of pulse length t_p and delay length t_d.

second set of TOP parameters (TOP2), chirped variants showed no significant enhancement over the unchirped case. Initially puzzling, this result was later explained by simulation, which showed that under these conditions, sweeping t_p or t_d introduces only negligible shifts in the effective driving frequency. As a result, the system does not undergo a meaningful Landau-Zener crossing, and chirped modulation fails to enhance the transfer. A similar limitation applies to pulse modifications that alter t_p and t_d while keeping the total cycle time $t_p + t_d$ constant: such changes leave the base modulation frequency nearly unchanged, thereby voiding any frequency sweep and nullifying the intended adiabatic effect.

These insights highlight the subtle but critical role of creating asymmetry in engineering effective chirped transfer. For chirping to induce a frequency sweep, it is essential that the pulse modifications introduce a net evolution in the modulation frequency or effective field orientation over time. Simply reshuffling internal timing without changing the overall evolution profile leads to adiabatic stagnation and fails to drive the system through resonance.

2.4.4 XiX

XiX is a symmetric phase-alternated sequence originally also developed for hetero-nuclear decoupling, consisting of identical pulses with fixed interpulse spacing and alternating phases. When adapted for DNP, however, a key limitation emerges: if the microwave frequency is centered at the EPR line, the sequence imposes a regular modulation on the electron spin, producing a trajectory that is symmetric and periodic, with minimal phase accumulation over time. While this may appear orderly, it leads to limited spectral breadth and weaker coupling to the nuclear spin reservoir. On the other hand, shifting the microwave frequency

Table 2.1: Results of pulsed DNP sequences studied in this paper. Enhancement factor is on/off at 10 s.

Sequence	Max Enh.	Parameter 1	Parameter 2	T_B (s)	Comments
TPPM(+)	315	$\tau = 17.5\,\text{ns}$	$\phi = 140°$	26	
Phase-Chirped TPPM(+)	488	$\Delta\phi = 10°$	$t_{\text{co}} = 45°$	20	+55%
TPPM(-)	-407	$\tau = 26.25\,\text{ns}$	$\phi = 60°$	22	
Phase-Chirped TPPM(-)	-470	$\Delta\phi = 10°$	$t_{\text{co}} = 5°$	21	+12%
Length-Chirped TPPM	–				No Increase
TOP1	183	$t_p = 18.75\,\text{ns}$	$t_d = 12.5\,\text{ns}$	33	$\Omega = -92\,\text{MHz}$
t_p Chirped TOP1	359	$\Delta t_p = 5\,\text{ns}$	$t_{\text{co}} = 45°$	24	+96%
t_d Chirped TOP1	364	$\Delta t_p = 5\,\text{ns}$	$t_{\text{co}} = 5°$	23	+99%
TOP2	245	$t_p = 12.5\,\text{ns}$	$t_d = 15\,\text{ns}$	31	$\Omega = -52\,\text{MHz}$
t_p Chirped TOP2	–				No Increase
t_d Chirped TOP2	–				No Increase
XiX	160	$t_p = 13.75\,\text{ns}$		39	$\Omega = -92\,\text{MHz}$
t_p Chirped XiX	260	$\Delta t_p = 2.5\,\text{ns}$	$t_{\text{co}} = 33°$	25	+62%
NMR	–			$T_1 = 22\,\text{s}$	

off-center can break this symmetry and improve trajectory dynamics, but at the cost of reduced microwave power due to the finite Q-factor of the resonator. As a result, XiX is generally less effective at establishing strong matching conditions compared to more flexible sequences such as TPPM or TOP.

Figure 2.10 shows a parameter scan of the XiX sequence as a function of microwave offset and pulse length t_p. A narrow ridge of enhancement is observed near $t_p = 13.75\,\text{ns}$ and a microwave offset of $\Omega = -92\,\text{MHz}$, corresponding to the condition where the spin trajectory generates a weak but resonant frequency component at the nuclear Larmor frequency. The resulting polarization transfer was moderate, reaching a maximum enhancement of 160. The sharpness of this ridge reflects the limited bandwidth of the modulation and the sensitivity of XiX to precise timing and offset conditions. Outside this narrow region, enhancement drops off quickly. This constrained behavior motivates the development of chirped variants to broaden the resonance and improve robustness.

To overcome the narrow resonance condition of the standard XiX sequence, we implemented a chirped variant in which the pulse length t_p was swept across the pulse train. As summarized in Table 2.1, this modification increased the enhancement from 160 to 260 under optimized conditions, corresponding to a 62% relative improvement. The chirp introduces a time-dependent detuning that enables the spin trajectory to sweep through resonance in a Landau-Zener-like fashion, broadening the effective transfer window. This approach demonstrates that even highly symmetric sequences like XiX can benefit from adiabatic design principles when appropriately modified.

Notably, despite the increased enhancement, the overall XiX performance remained lower than that of TPPM or chirped TOP. This may be attributed to the symmetric nature of the base sequence, which limits the accumulated rotation and restricts the dynamic range of the effective trajectory. Nevertheless, the observed improvement with chirping confirms that XiX

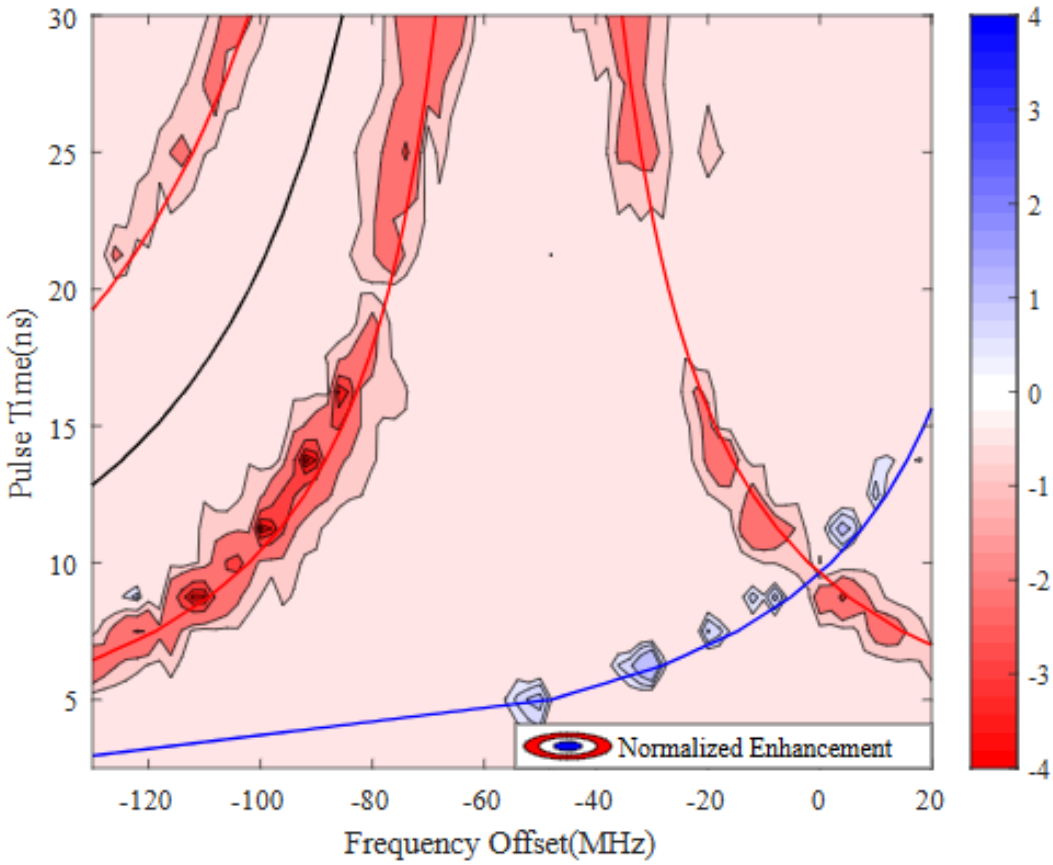

Figure 2.10: Parameter scan of the XiX sequence showing enhancement as a function of microwave offset and pulse length t_p. A few narrow enhancement ridge appears, with limited spectral bandwidth.

benefits from the same adiabatic principles and provides an alternative route for controlled polarization transfer when other sequences are less effective.

2.5 Conclusions and Discussion

This chapter presented a systematic study of several pulsed DNP sequences in static solids, including TPPM, TOP, and XiX, using a combination of theoretical models and experimental validation. The primary theoretical framework—based on the time-dependent trajectory of the driven electron spin and its frequency-domain structure—was shown to accurately predict the conditions under which polarization transfer occurs. In particular, sequences that generate coherent motion of the electron spin containing frequency components near the nuclear Larmor frequency were found to produce measurable enhancements, while sequences lacking such components were less effective.

A central insight that emerged from this work is the importance of controlled frequency modulation during the pulse train. By borrowing concepts from adiabatic sequences such as

ASE and ISE[40, 49, 55], we introduced chirped versions of TPPM, TOP, and XiX in which the phase, pulse duration, or inter-pulse delay was varied smoothly across the pulse train. These chirped sequences enable the electron spin trajectory to sweep through resonance conditions more gradually, allowing for Landau-Zener-type transitions that enhance the probability of polarization transfer. Experimental results confirmed this intuition: for both TPPM and TOP, chirped versions yielded significantly higher enhancements compared to their unchirped counterparts, often exceeding them by 50–100%. Even the symmetric XiX sequence, showed clear improvement when modified to incorporate a time-dependent pulse length.

However, the study also revealed limitations of these methods. Not all chirps lead to improved transfer: in certain timing configurations, particularly in the second TOP condition (TOP2), chirped modulation had little effect. Post-hoc simulations showed that in these cases the chirp failed to shift the effective electron spin frequency sufficiently, and thus did not produce a meaningful sweep across resonance. This outcome emphasizes a subtle but important point: not all parameter variations result in adiabatic frequency sweeps. In particular, chirps that maintain a constant total cycle time $t_p + t_d$ may leave the base modulation frequency unchanged and therefore fail to activate a Landau-Zener channel. These results underscore the value of simulation and theory in interpreting experimental outcomes and guiding pulse design.

While the agreement between theory and experiment is strong in identifying transfer conditions and relative performance, it is important to recognize that the current models remain incomplete. All trajectory-based and frequency-domain approaches developed in this work assume purely coherent dynamics and neglect the influence of relaxation—specifically, the electron dephasing time T_2 and the nuclear longitudinal relaxation time T_1, or more precisely, the experimentally measured buildup time T_B under microwave irradiation. These relaxation times fundamentally limit the efficiency of polarization transfer and determine how much polarization can accumulate in a given time window.

One might expect, for instance, that a Landau-Zener-style sweep would fail if electron spin coherence is lost before the sweep completes. This intuition is sound in principle, but it does not align with our experimental observations. In our experiments, the pulse sequences used—particularly chirped versions of TPPM and TOP—had total durations of $48\,\mu$s, significantly longer than the measured electron T_2 time of approximately $3.3\,\mu$s. Despite this apparent mismatch, these sequences consistently yielded the highest enhancements. As shown in the Supporting Information, increasing the pulse length generally improves the enhancement, even well beyond the electron dephasing time. The reason for this counterintuitive trend remains unclear, but may suggest that certain aspects of the spin transfer process are resilient to decoherence—possibly because the relevant polarization pathways are repeatedly reinitialized or because incoherent dynamics contribute constructively over longer timescales.

A second open question arises from the observed correlation between the nuclear buildup time T_B and the measured enhancement factor. Empirically, sequences with longer T_B tend to yield lower enhancements. The exact mechanism behind this inverse relationship is not fully understood. One speculative explanation is that a longer T_B may reflect inefficient transfer to bulk nuclear spins or slower spin diffusion away from the hyperfine-coupled site, which limits how much of the transferred polarization survives long enough to be detected.

Alternatively, longer buildup times may coincide with a non-efficient polarization pathway being the limiting factor, instead of spin diffusion. The exact reason of this behavior remains to be studied.

These observations highlight the limitations of purely coherent models and point toward the need for a more complete theoretical treatment. Incorporating relaxation into DNP theory is nontrivial: electron T_2 dephasing disrupts the unitary spin trajectory on which current models are built, requiring a shift toward open quantum systems and stochastic or Lindblad-based descriptions. The nuclear T_1 enters more subtly, setting the timescale for polarization retention and recovery. Some prior work in the context of solid-effect and cross-effect DNP has addressed these issues using master equations or semiclassical averaging[56–58], but a unified framework that integrates relaxation with time-dependent spin driving and spectral selectivity remains elusive. Developing such a model would enable more accurate predictions of absolute enhancements and help explain the intricate interplay between pulse design, spin coherence, and sample-specific relaxation properties.

In summary, this work demonstrates that a large portion of pulsed DNP behavior in static solids can be explained through the coherent dynamics of driven electron spins. By examining the frequency content of the spin trajectory and introducing time-dependent chirps to traverse resonance conditions, we achieve both conceptual understanding and experimental improvement. Nonetheless, fully predictive theory must ultimately account for relaxation processes. Developing such a model—one that integrates coherent driving, spectral matching, and decoherence—represents a key direction for future work.

2.6 Supporting Information

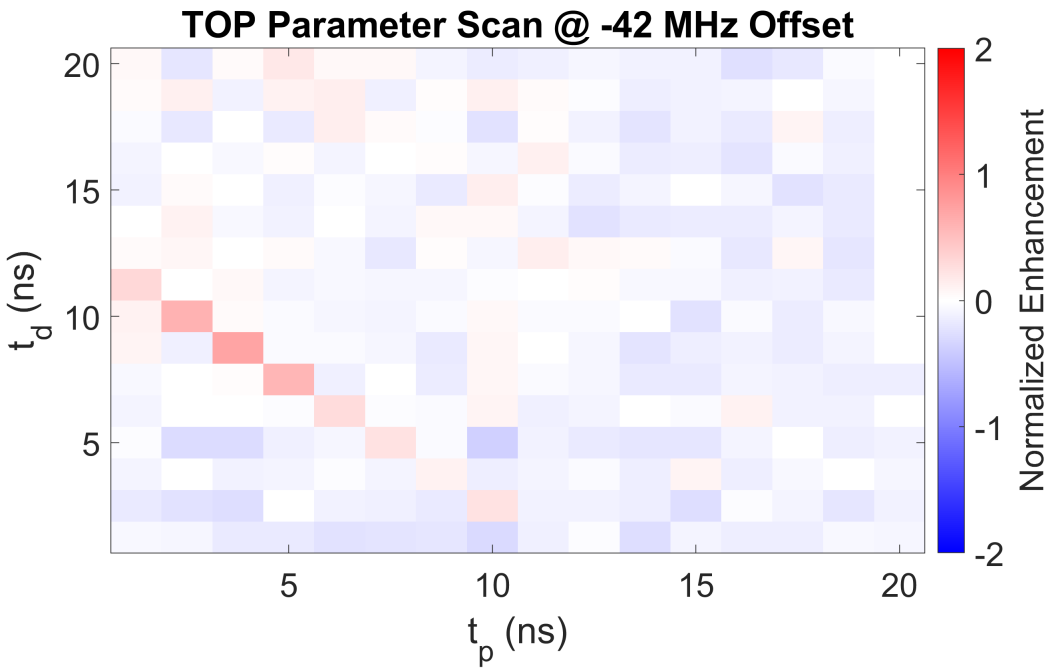
TOP Parameter Scan @ -42 MHz Offset
20
15
10
5
t_d (ns)
5
10
15
20
t_p (ns)
2
1
0
-1
-2
Normalized Enhancement

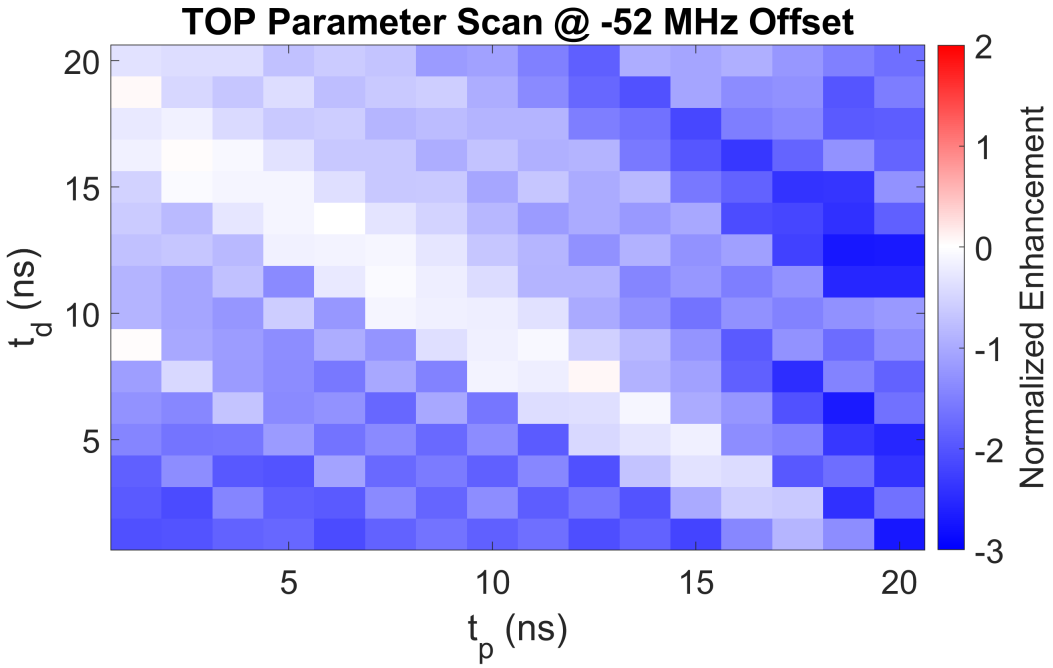
TOP Parameter Scan @ -52 MHz Offset
20
15
10
5
t_d (ns)
5
10
15
20
t_p (ns)
2
1
0
-1
-2
-3
Normalized Enhancement

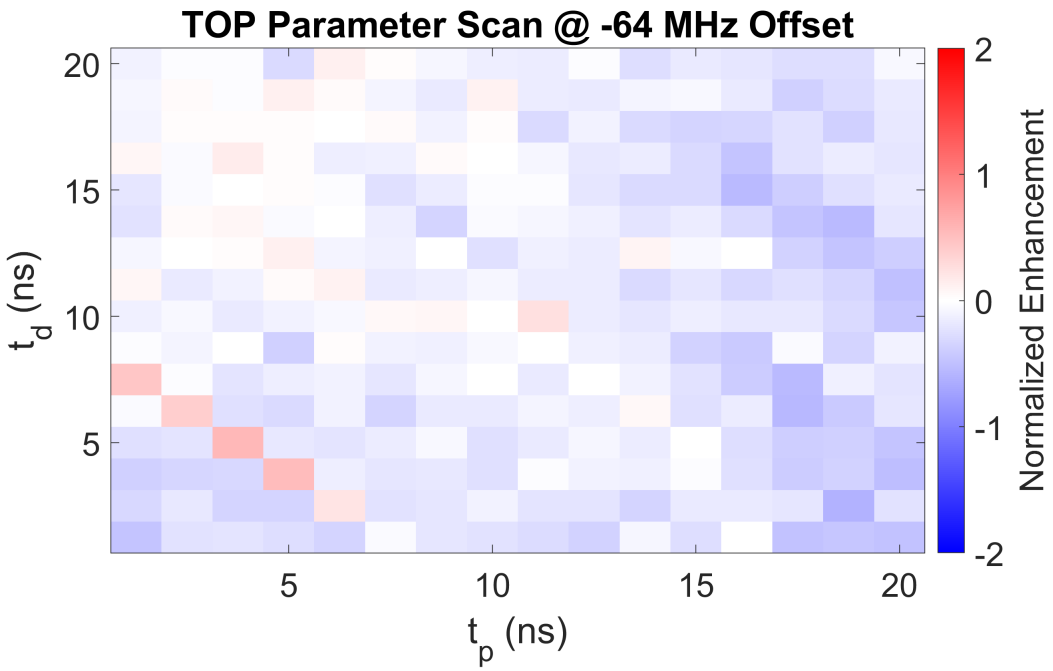
TOP Parameter Scan @ -64 MHz Offset
20
15
10
5
t_d (ns)
5
10
15
20
t_p (ns)
2
1
0
-1
-2
Normalized Enhancement

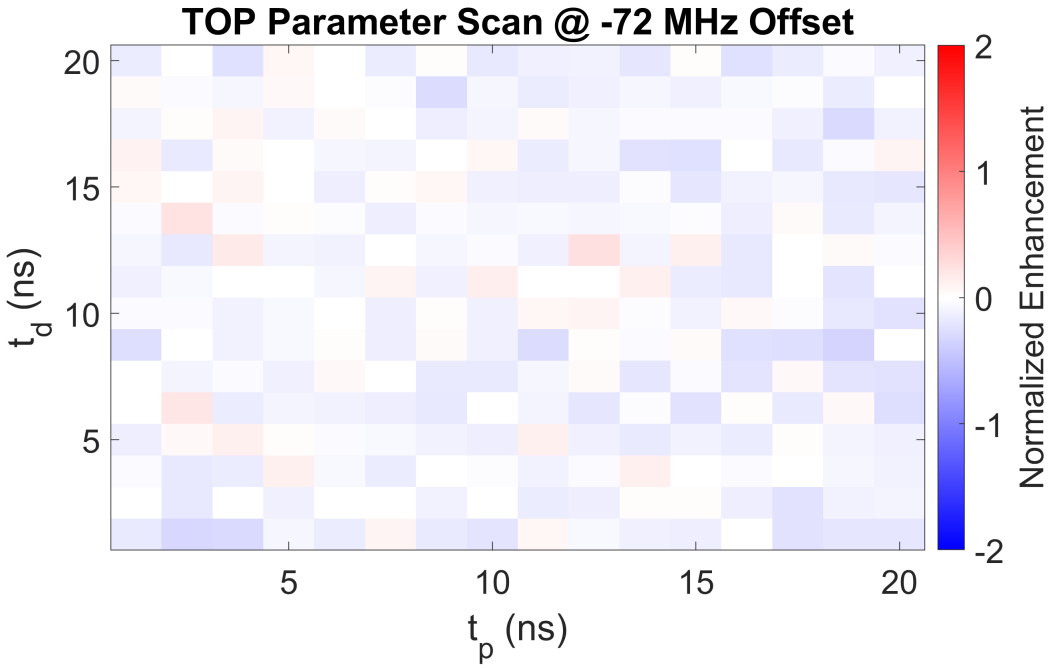
TOP Parameter Scan @ -72 MHz Offset
20
15
10
5
t_d (ns)
5
10
15
20
t_p (ns)
2
1
0
-1
-2
Normalized Enhancement

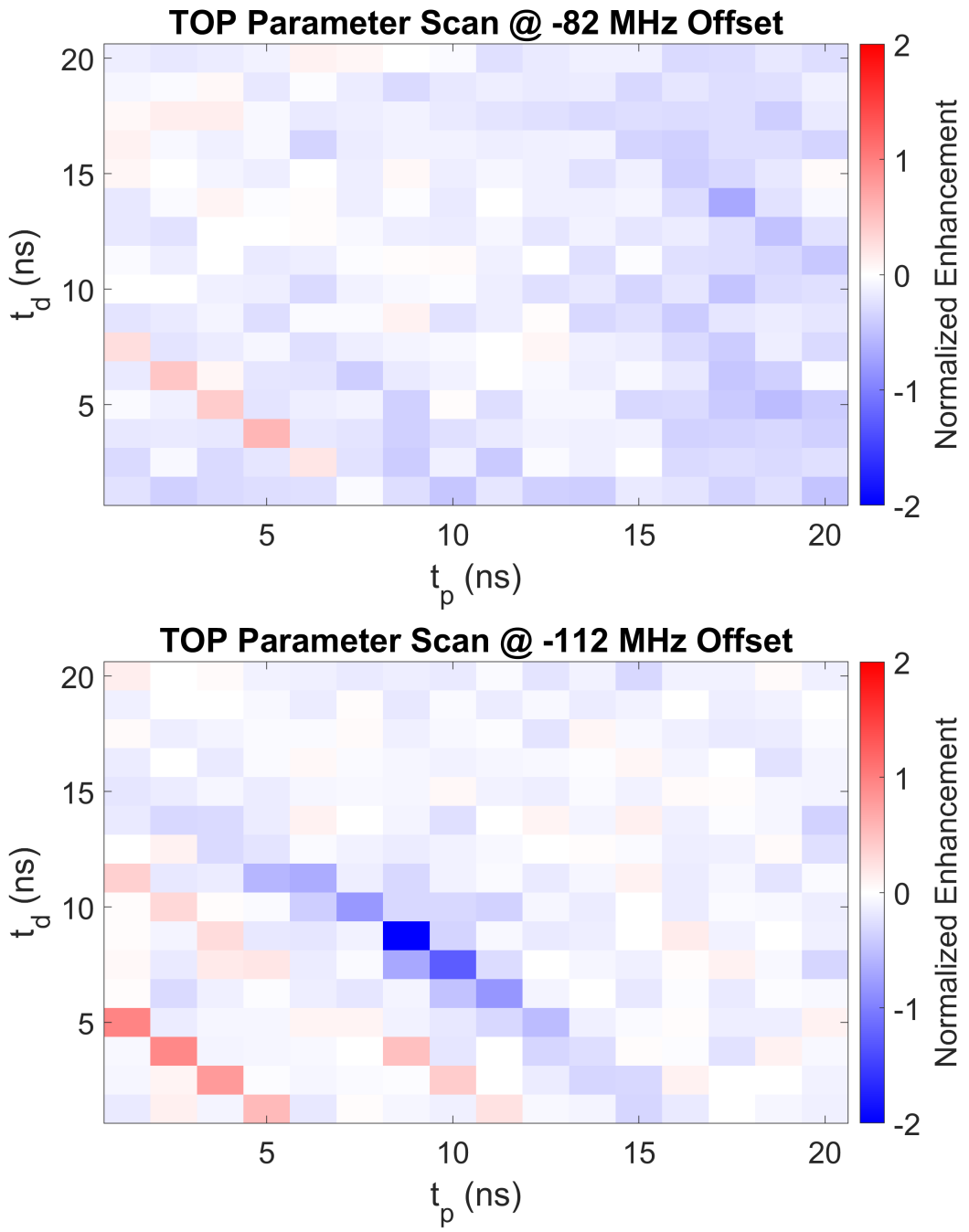

Figure 2.11: TOP parameter scan showing NMR intensity as a function of pulse length t_p and delay length t_d. Enhancement maxima occur near effective frequencies that satisfy $\omega_{e\square} \pm k\omega_m = \omega_n$.

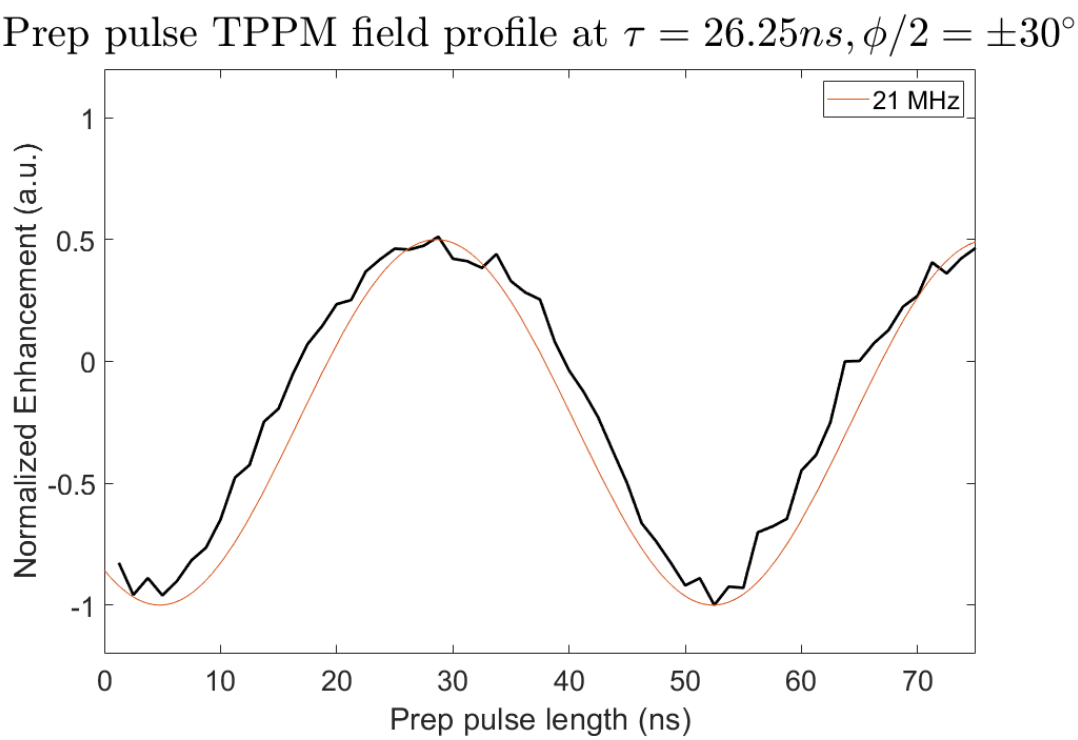

Figure 2.12: Prep-pulse scan of TPPM parameter at negative maximum, with prep pulse phase fixed at $\theta = 300°$. Note that (1) this gives an accurate measurement of ω_{1S} and (2) the anti-symmetry of maxima and minima is not observed.

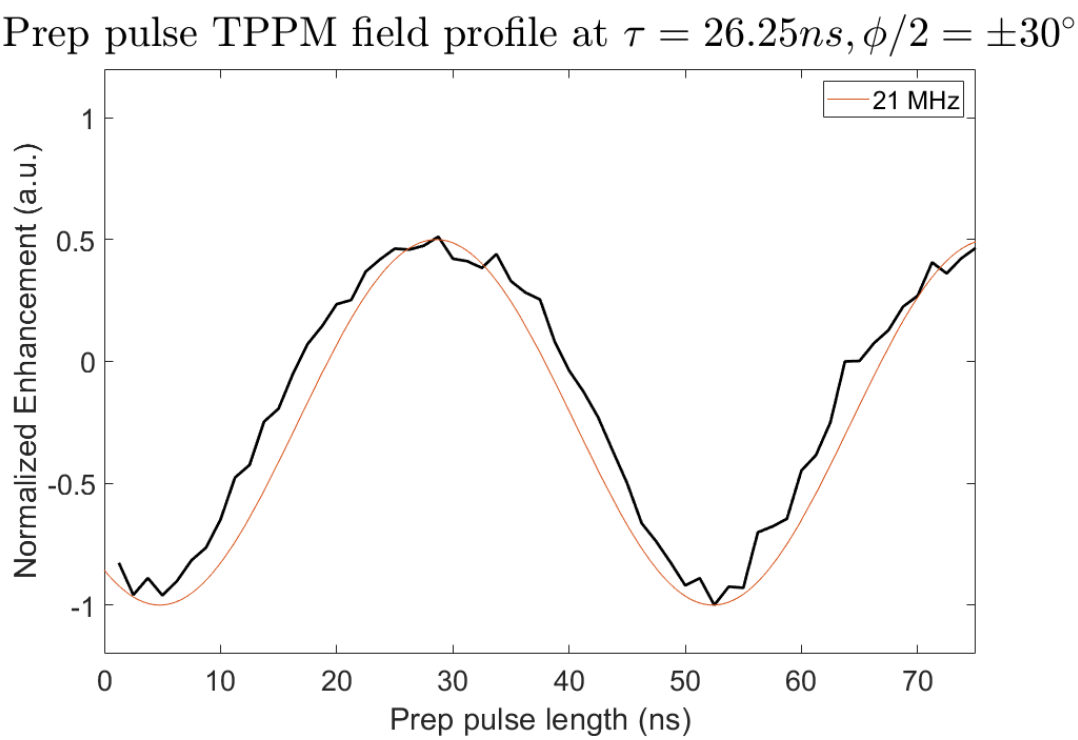

Figure 2.13: Prep-pulse scan of TPPM parameter at negative maximum, with prep pulse phase fixed at $\theta = 300°$. Note that (1) this gives an accurate measurement of ω_{1S} and (2) the anti-symmetry of maxima and minima is not observed.

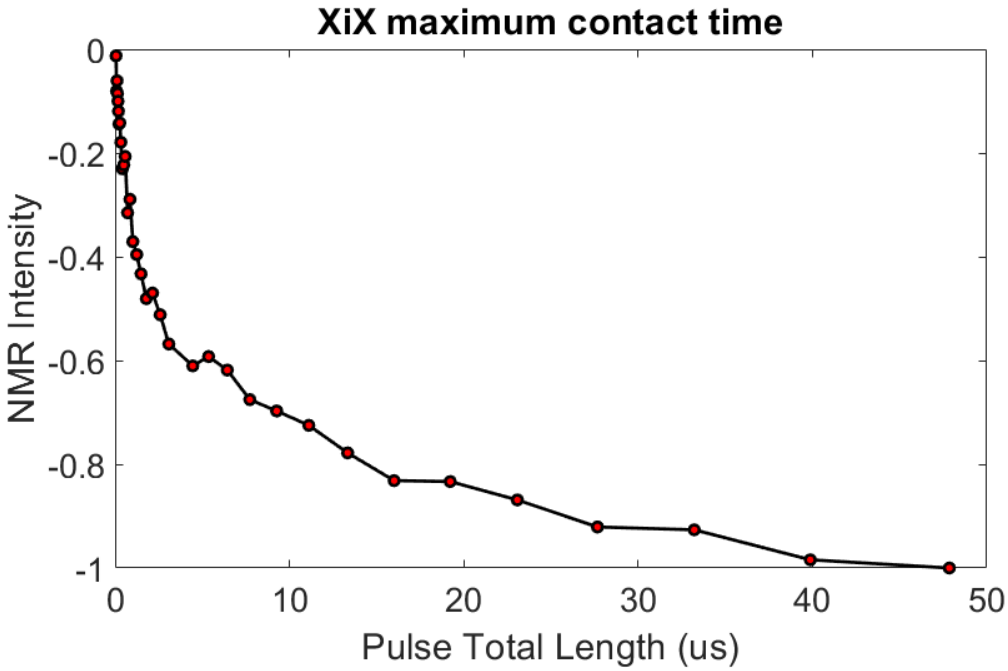
XiX maximum contact time
NMR Intensity
Pulse Total Length (us)
0
-0.2
-0.4
-0.6
-0.8
-1
0
10
20
30
40
50

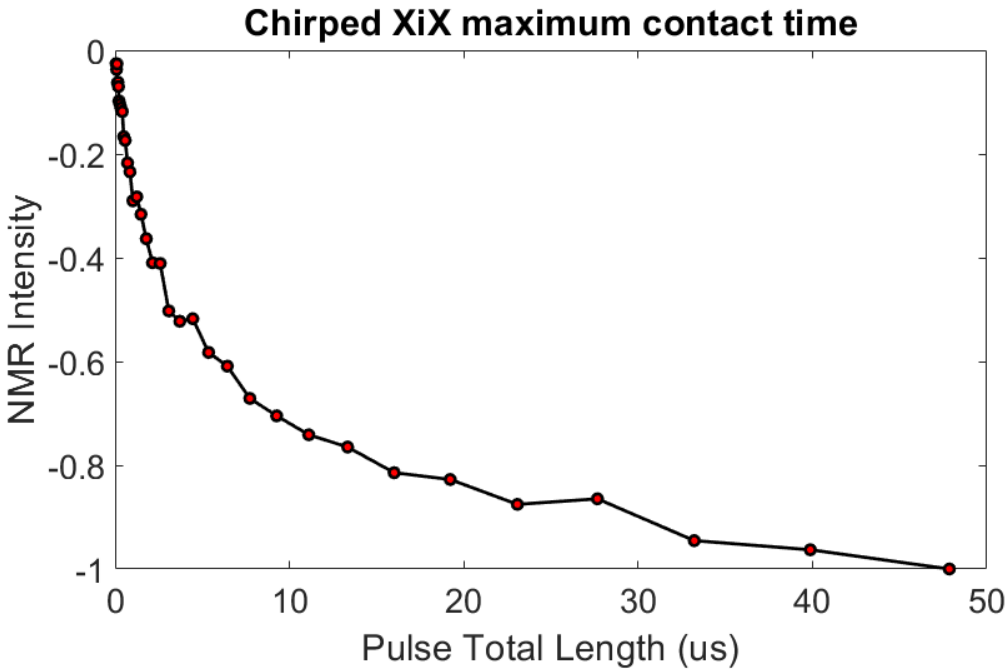
Chirped XiX maximum contact time
NMR Intensity
Pulse Total Length (us)
0
-0.2
-0.4
-0.6
-0.8
-1
0
10
20
30
40
50

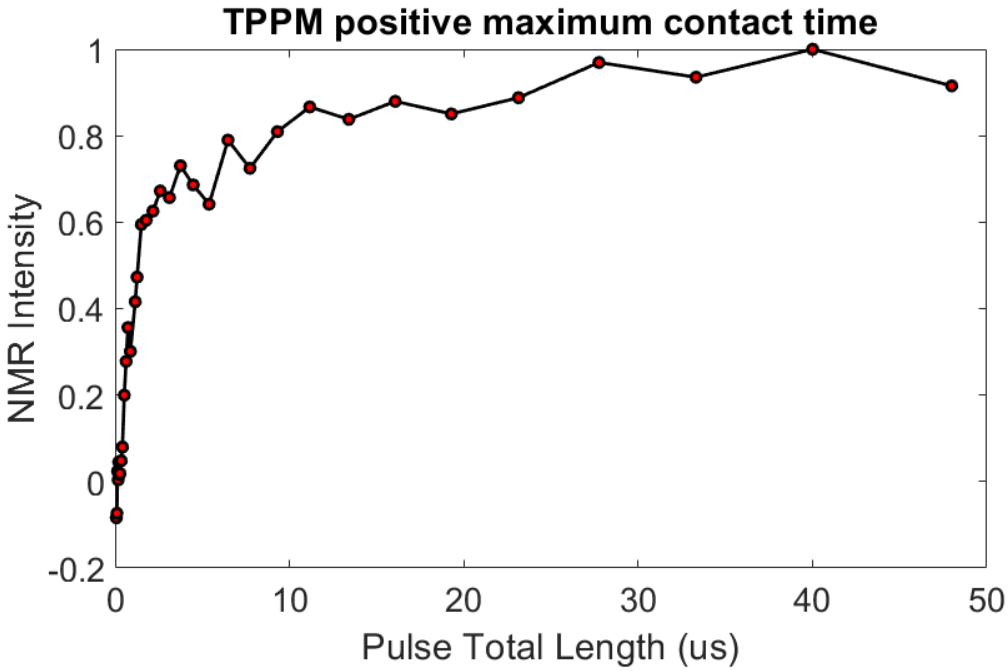
TPPM positive maximum contact time
NMR Intensity
Pulse Total Length (us)
1
0.8
0.6
0.4
0.2
0
-0.2
0
10
20
30
40
50

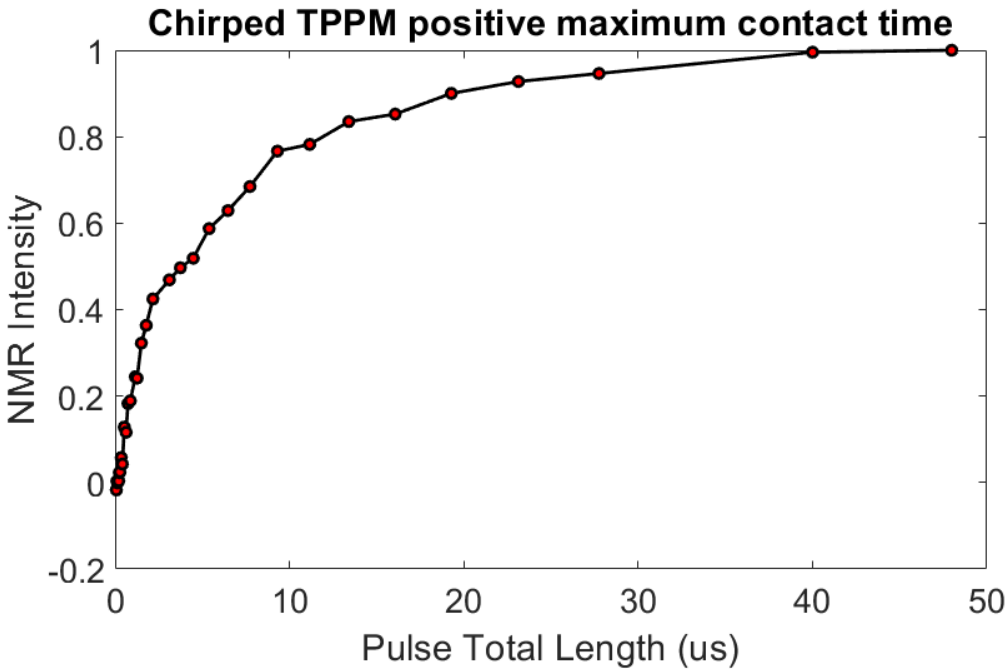
Chirped TPPM positive maximum contact time
NMR Intensity
Pulse Total Length (us)
1
0.8
0.6
0.4
0.2
0
-0.2
0
10
20
30
40
50

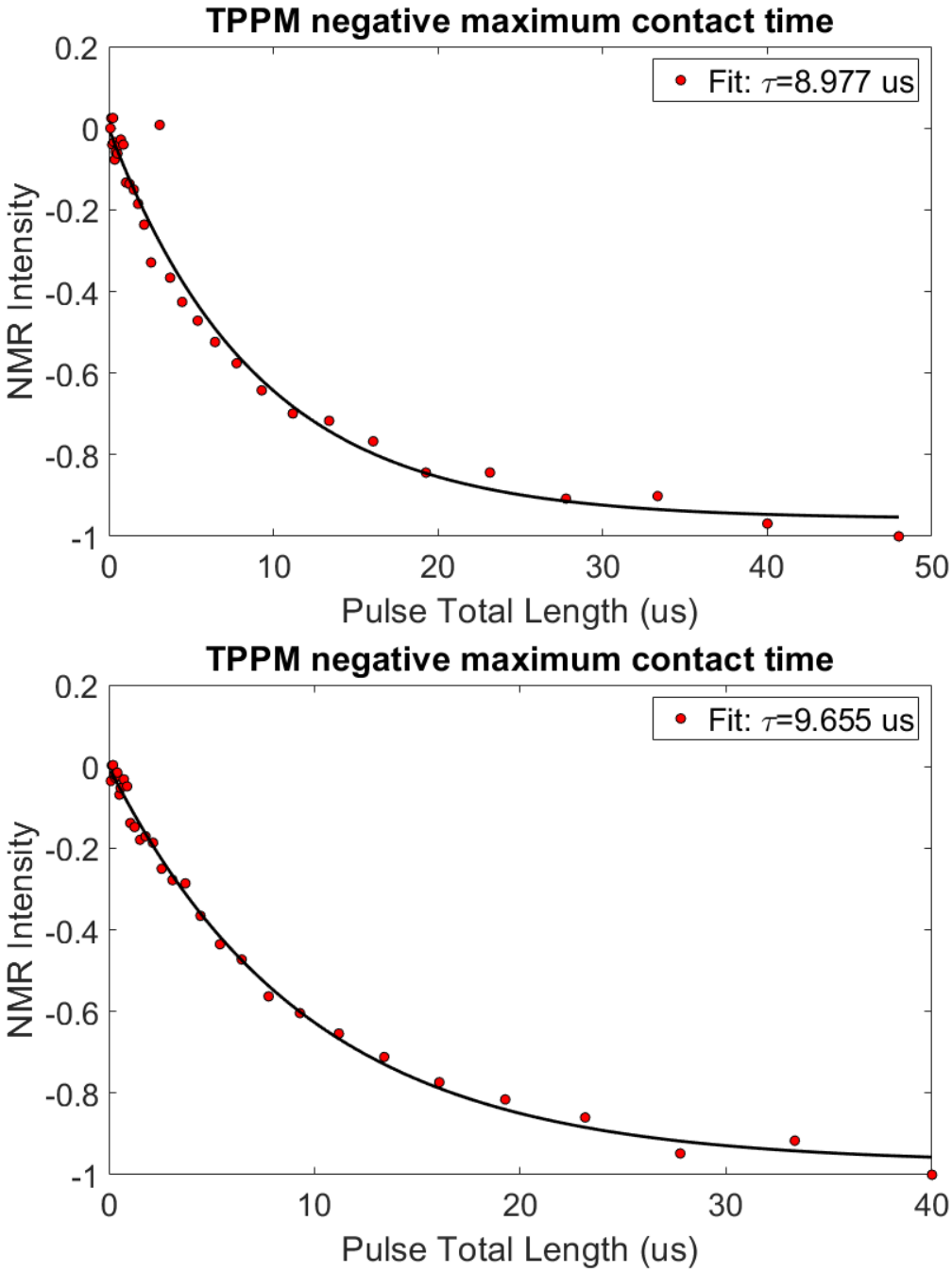

Figure 2.14: Contact curve for some pulse sequences. All is recorded at optimal parameters. Some are fitted to a single exponential, while others don't have such behavior.

TPPM field profile at $\tau = 26.25ns, \phi/2 = \pm 30^\circ$

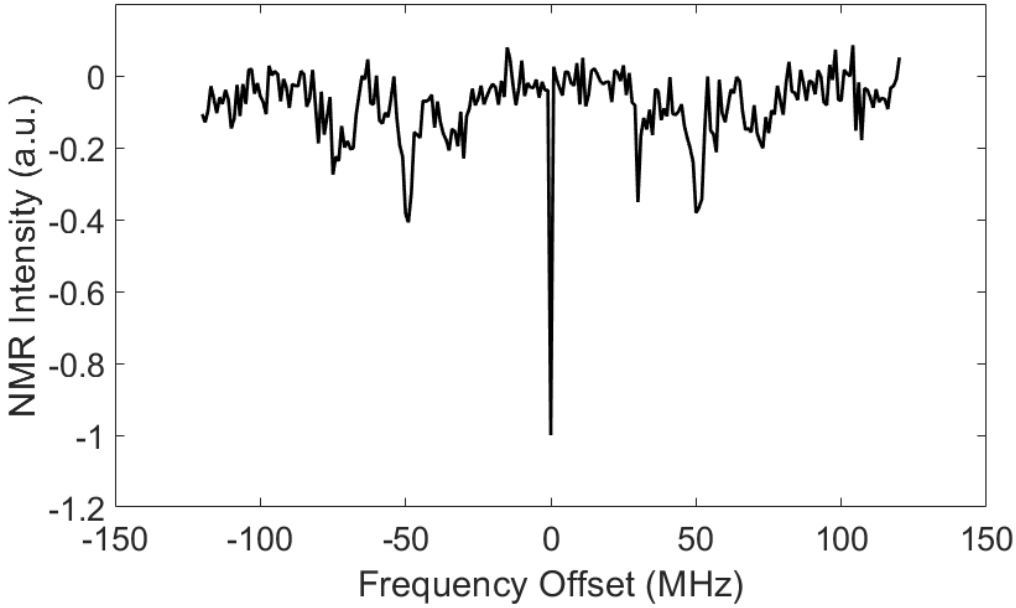

TPPM field profile at $\tau = 17.5ns, \phi/2 = \pm 70^\circ$

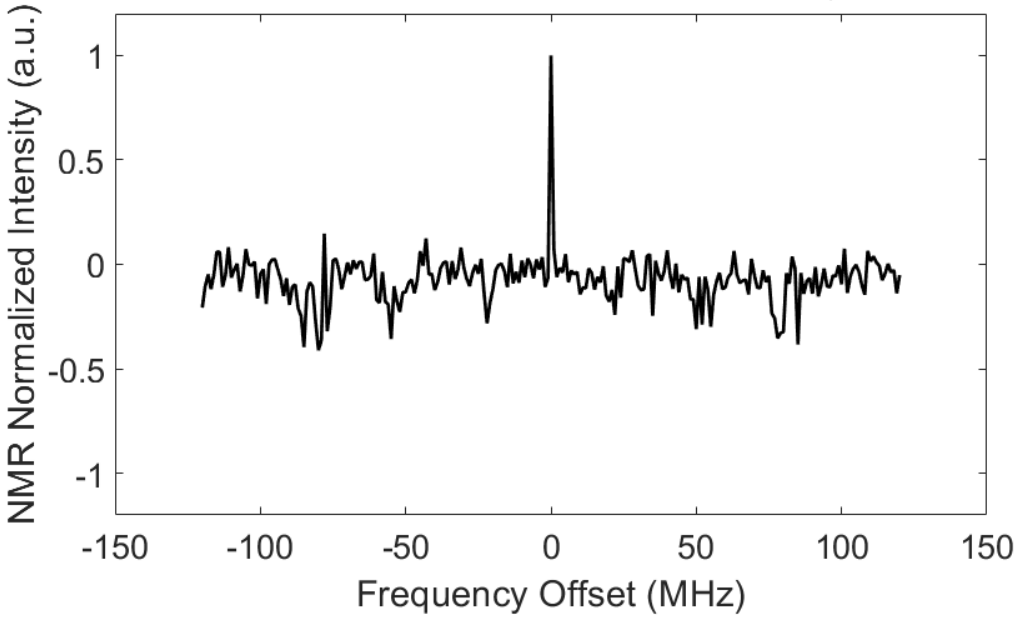

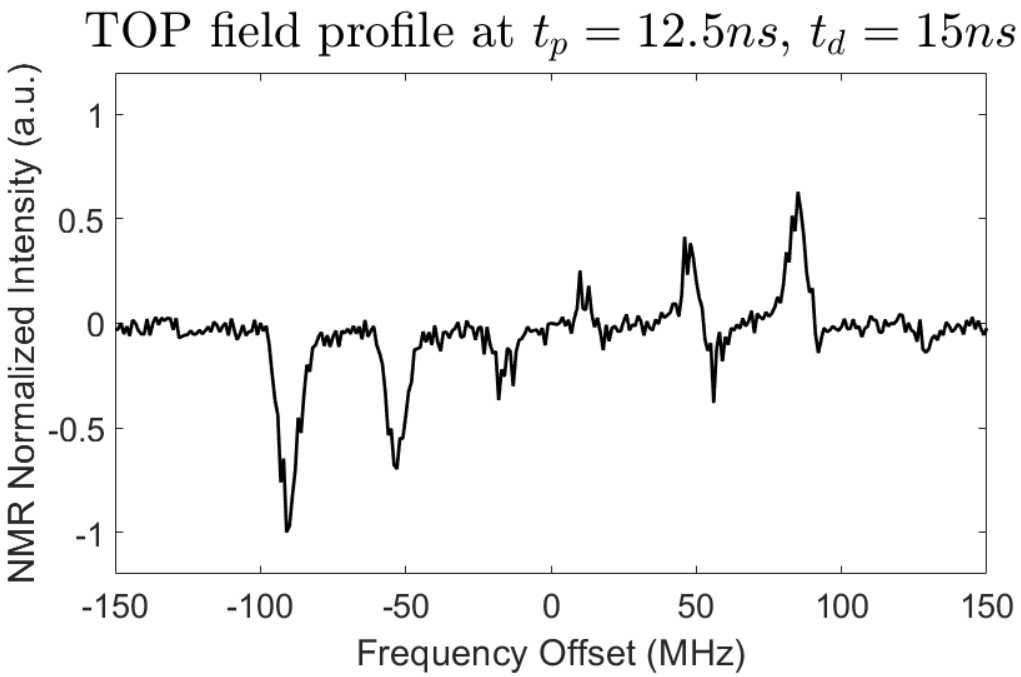
TOP field profile at $t_p = 12.5ns$, $t_d = 15ns$
NMR Normalized Intensity (a.u.)
1
0.5
0
-0.5
-1
-150
-100
-50
0
50
100
150
Frequency Offset (MHz)

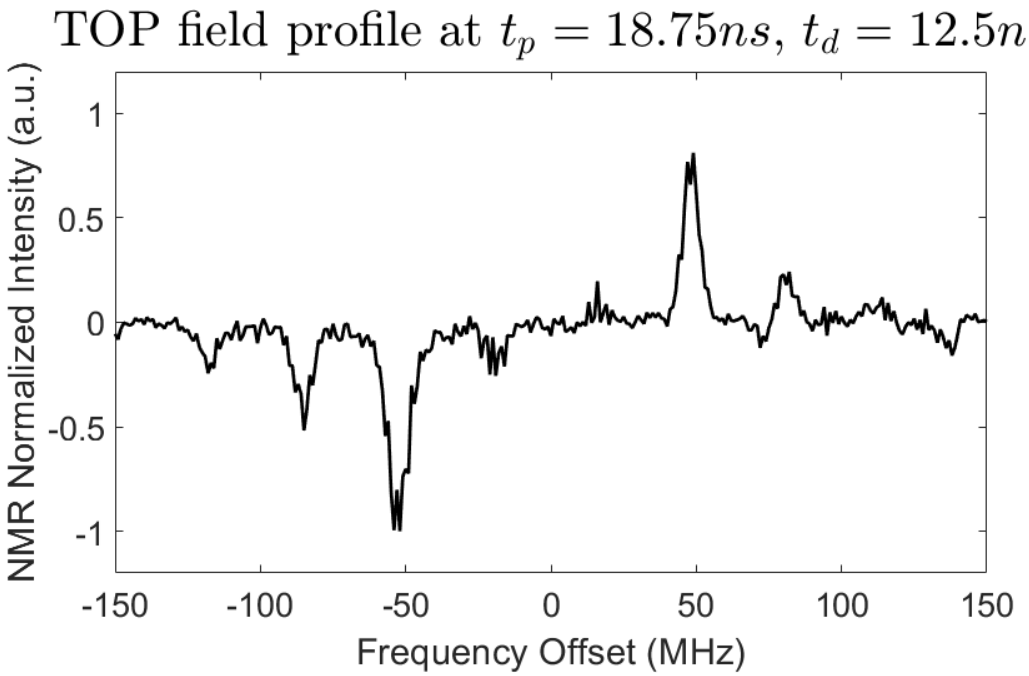
TOP field profile at $t_p = 18.75ns$, $t_d = 12.5ns$
NMR Normalized Intensity (a.u.)
1
0.5
0
-0.5
-1
-150
-100
-50
0
50
100
150
Frequency Offset (MHz)

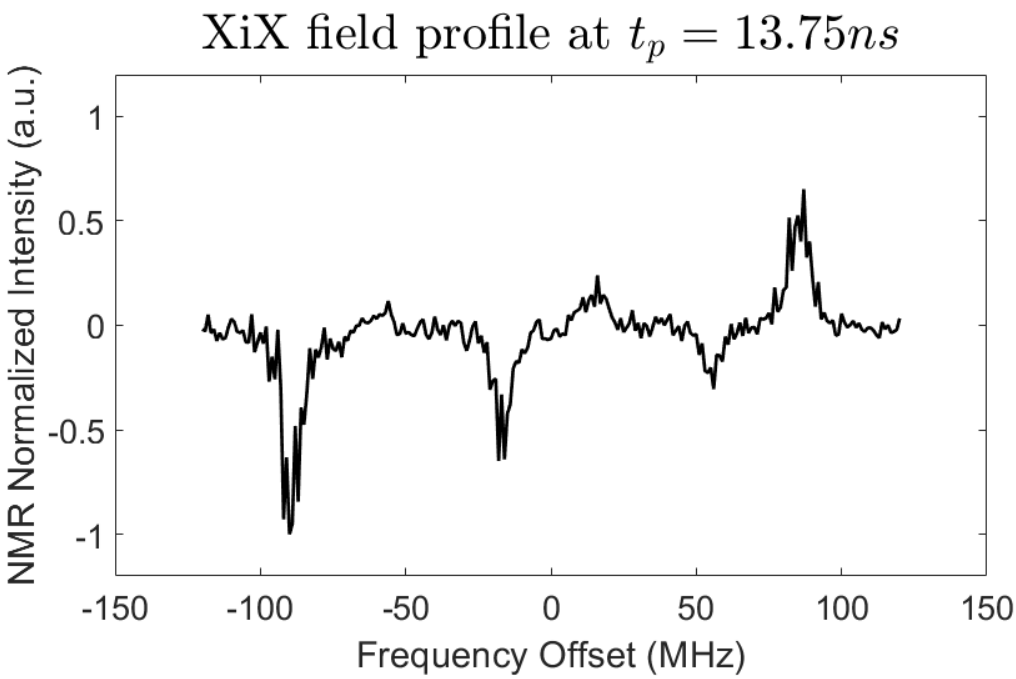

Figure 2.15: Enhancement factor versus microwave frequency offset of some pulse sequences. All data is normalized to the optimal condition. Parameter is the same as optimal condition except frequency.

Chapter 3

Overhauser E□ect and Resonant Mixing

Dynamic nuclear polarization (DNP) enhances NMR sensitivity by transferring polarization from electrons to nuclei, with multiple mechanisms—such as the solid effect (SE), cross effect (CE), and thermal mixing (TM)—well established for insulating solids. The Overhauser effect (OE), by contrast, is traditionally associated with liquids or conducting systems, where rapid molecular motion enables electron–nuclear cross-relaxation. Its observation in insulating solids was therefore unexpected and has prompted significant theoretical and experimental interest.

Recent work has shown that Overhauser-type enhancements can indeed arise in non-conducting, glassy matrices under magic angle spinning (MAS), particularly when narrow-line radicals such as BDPA are used. These findings suggest that time-dependent modulation of hyperfine couplings—possibly driven by intramolecular dynamics or photoexcitation—may substitute for molecular tumbling in solids. Building on this insight, it has become possible to manipulate the Overhauser effect through chemical

3.1 Amplified Overhauser DNP with Selective Deuteration

This section is reproduced from the published article[59]: *Amplified Overhauser DNP with Selective Deuteration: Attenuation of Double-Quantum Cross-Relaxation*, **J. Phys. Chem. Lett. 2023**, *14*, 95–100, with minimal formatting changes for thesis integration. The content is included with permission from the publisher.

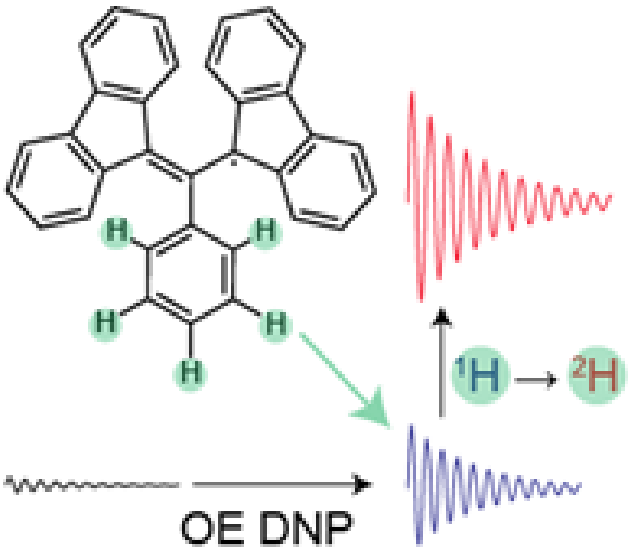

Figure 3.1: Deuteration of phenyl ring on BDPA radical leads to larger OE enhancement.

Nuclear magnetic resonance (NMR) spectroscopy suffers from low sensitivity due to the small size of the nuclear spin energy splittings relative to the thermal energy. Dynamic nuclear polarization (DNP) overcomes this difficulty by using microwave irradiation of electron-nuclear transitions to transfer the polarization of electron spins to the nuclei of interest [19, 60, 61]. The increased sensitivity available from DNP has revolutionized the field of NMR, both in liquids and solids, and has enabled the structural studies[62, 63] of biomolecules and materials in more complex environments than were previously feasible[6, 64–68].

Particularly effective approaches to DNP rely on coherent manipulation of the electron spin polarization and require that the electron Rabi frequency, ω_{1e}, be greater than the spin–spin relaxation rate of the electrons, $1/T_{2e}$, where T_{2e}, the electron transverse relaxation time, and is typically on the order of a few microseconds. ω_{1e} is proportional to the square root of microwave power and with current technology this usually ranges from a few milliwatts to tens of watts. Although higher powers have been achieved[69], microwave power is a limitation frequently encountered at magnetic field strengths exceeding 5 T[70]. Thus, absent a resonance microwave structure to boost efficiency in coupling ω_{1e} to the sample, the electron Rabi frequency is low and coherent transfers are presently not practical. However, the achievable Rabi fields are sufficient to support continuous-wave DNP (CW-DNP) mechanisms[71, 72]. Accordingly, four known CW-DNP mechanisms are typically utilized in DNP experiments on solids: the solid effect (SE) [73, 74], the cross effect (CE) [75–77], thermal mixing (TM) [78–81], and the Overhauser effect (OE) [19, 82]. Detailed discussions of the first three mechanisms – the SE, CE, and TM – are available in review articles[71, 72, 83].

The OE, which is the subject of this paper, requires coupled electron-nuclear spin pairs. Microwave irradiation at the EPR (electron paramagnetic resonance) frequency of a polarizing agent with a narrow line, such as BDPA, drives allowed single-quantum EPR transitions. Subsequent cross-relaxation in the coupled electron-nuclear spin system via zero quantum (ZQ) and double quantum (DQ) pathways with unequal rates, results in enhanced polarization of the nuclear spins. The polarization buildup of the nuclear spins can be positive or negative, depending on whether either the ZQ or the DQ cross-relaxation is dominant, respectively.

The advantages of the OE mechanism are that it scales positively with magnetic field and with increasing spinning frequency. Furthermore, because the EPR spectrum of BDPA is narrow level crossing does not occur during spinning and therefore the OE it is not subject to depolarization as it the CE.

The OE is usually observed in liquids, conducting solids, or doped semiconductors[84, 85], systems where there is mobility of the spins involved, i.e., where translational fluctuations drive cross-relaxation needed for DNP. More recently, OE DNP was surprisingly observed in insulating solids doped with BDPA [10, 86–89]. Cross-relaxation requires time-dependent modulation of the hyperfine couplings, and the source of the modulation in insulating solids is yet to be definitively established. Recently, it was proposed that intramolecular charge transfer by the mixed-valence nature of BDPA could be responsible for the modulation[90] and other mixed-valence polarizing agents that exhibit the OE were recently reported [88, 91]. It was also recently suggested that what is generally identified as an OE in BDPA is in fact due to TM [92]; however, this topic, while extremely interesting, is not the subject of research results presented here.

The primary topic explored here is the role of the ^{1}H nuclei on the polarization agent in facilitating DNP, and ultimately contributing to the diffusive spread of polarization throughout the sample. In a previous study, we investigated this role via the proton spins on the fluorene moieties (Scheme 3.2, top left) in determining OE DNP enhancements using selectively deuterated BDPA variants as the agent[93]. We established that the strongly coupled ($\sim$5.4 MHz) ^{1}H spins at the α and γ positions of the fluorenes are essential for generating positive enhancements, while the weakly coupled ($\sim$1 MHz) ^{1}H spins on the β and δ positions are likely crucial for efficient spin diffusion of the polarization from the ^{1}H spins on the radical to the bulk. We also observed a negative DNP enhancement of the bulk ^{1}H spins for 1,3-[d_{16}-]-BDPA, where all the 16 ^{1}H positions in the fluorenes were deuterated. This suggested that the ^{1}H spins on the phenyl ring, which exhibit small hyperfine couplings and have heretofore been considered inconsequential, cumulatively contributed to the negative enhancement observed in the bulk. However, their relative contributions to the OE DNP were unknown.

In this study, we determine the relative contributions of the ^{1}H spins on the phenyl ring and the ^{1}H spins in immediately surrounding oTP molecules to the overall negative polarization observed in the bulk ^{1}H spins. This was addressed by performing DNP experiments on a fully deuterated sample, and the data suggested that the ^{1}H spins on the phenyl ring and ^{1}H spins in the nearby oTP molecules were negatively polarized via a DQ OE DNP mechanism. Based on this, we used minimial chemistry to synthesize a phenyl-deuterated BDPA radical hypothesizing that it would result in improved positive OE DNP enhancement observed in the bulk. We verified this to be the case with DNP experiments performed at magnetic fields ranging from 5 T to 14.1 T. Furthermore, we confirm that OE enhancments do scale with B0 and that there is no depolarization because of the narrow linewidth of the BDPA EPR spectrum. For these reasons it is important to develop further examples of OE radicals for use in DNP MAS experiments at high fields.

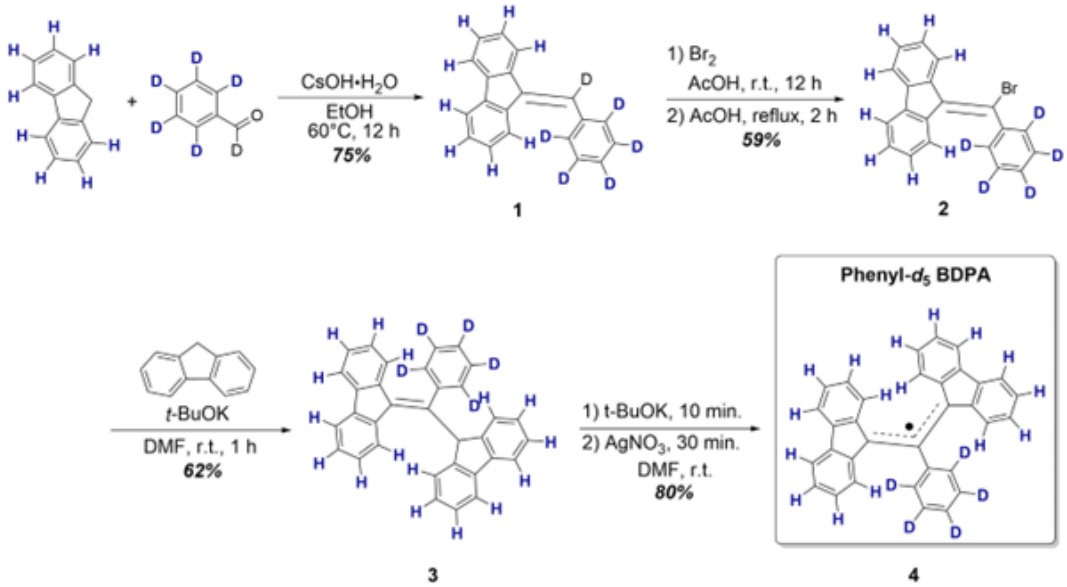

Figure 3.2: Synthetic route to Phe-d_5–BDPA radical.

3.1.1 Synthesis

Scheme 3.2 details the synthetic route used to synthesize Phe-d_5-BDPA, which is based on a previous report[93]. Synthetic routes to BDPA radicals are well established and Phe-d_5-BDPA can be obtained in four steps from readily available fluorene and benzaldehyde-d_6 or benzaldehyde-d_5. First, condensation of fluorene with one equivalent of benzaldehyde-d_5 delivered 9-((phenyl-d_5)methylene)-9H-fluorene (**1**) in 75% yield. Compound **1** was subsequently subjected to a two-step process consisting of an alkene bromination with bromine followed by dehydrobromination to obtain 9-(bromo(phenyl-d_5)methylene)-9H-fluorene (**2**) in 59% yield. Next, **2** was condensed with another equivalent of fluorene via a nucleophilic addition-elimination sequence to form the neutral precursor Phe-d5-BDPA-H (**3**) in 62% yield. Finally, radical formation to obtain Phe-d_5-BDPA was performed by deprotonation of **3**, followed by one-electron oxidation of the resulting anion using silver nitrate. This last step was performed with an 80% yield. For further experimental details on the synthesis of Phe-d_5-BDPA radical, we refer the reader to the Supporting Information.

3.1.2 DNP Experiments

The DNP experiments were performed using four different NMR/DNP spectrometers operating at the following fields, ^{1}H frequencies, and microwave frequencies for g=2 electrons: 5.0 T/211 MHz/140 GHz, 8.9 T/380 MHz/250 GHz, 9.4 T/400 MHz/263 GHz, and 14.1 T/600 MHz/395 GHz. The DNP experiments on the 8.9 T/380 MHz/250 GHz spectrometer were performed with microwave irradiation from a homebuilt 250 GHz gyrotron delivering ∼5 watts of output power, and a low-power 160 mW solid-state source from Virginia Diodes, Inc. (VDI) (**Figure 3.4a**). The low-power microwave system uses an arbitrary waveform generator (Keysight AWG M8190A) and an amplifier multiplier chain (VDI AMC 691) and is capable of producing microwaves over a frequency range of 8 GHz from 246 – 254 GHz. The

details of this instrument will be discussed in detail in a future publication. The gyrotron source of this DNP spectrometer is capable of producing microwaves at 250.02 GHz, which is required to observe the OE DNP in the BDPA samples studied here. The DNP experiments on the 9.4 T/400 MHz/263 GHz spectrometer were performed with microwaves from a 280 mW amplifier multiplier chain (VDI AMC 749). The DNP experiments on the 14.1 T/600 MHz/395 GHz spectrometer were performed with a 30 W gyrotron at a fixed frequency of 395.285 GHz. The NMR magnetic field is swept to obtain DNP Zeeman profiles with a gyrotron, while the microwave frequency is swept at a fixed field with the solid-state sources. All the experiments were performed at a MAS frequency of $\omega_r/2\pi = 5$ kHz, except for the experiments on the 5 T spectrometer which was performed at a MAS frequency of $\omega_r/2\pi =$ 3.5 kHz. The temperature of the sample was 90 K (5 T and 8.9 T) or 100 K (9.4 T and 14.1 T).

The DNP samples were prepared by doping 2.5 wt% of the radical, h_{21}-BDPA, Phe-d_5-BDPA, or d_{21}-BDPA, all in 1:1 complex with benzene, into a mixture of 95/5 mol% d_14- and h_14-ortho-terphenyl (oTP) [94]. In molar concentrations, this corresponds to ∼60.0 mM of h_{21}-BDPA, ∼59.4 mM of Phe-d_5-BDPA, and ∼57.5 mM of d_{21}-BDPA. h_{21}-BDPA was purchased from Sigma-Aldrich, while the Phe-d_5-BDPA was synthesized as discussed in the previous Section. The perdeuterated d_{21}-BDPA was prepared using procedures described previously[93]. The doped mixture was dissolved in $CDCl_3$ which was removed by evaporation under a vacuum. The resulting thin film was finely ground and packed in a 4 mm sapphire rotor for experiments on the 5 T and 8.9 T DNP spectrometers or a 3.2 mm sapphire rotor for experiments on the 9.4 T and 14.1 T DNP spectrometers. The 4 mm sapphire rotors were subsequently warmed in a sand bath maintained at 60 °C for five minutes to melt the oTP and then quenched in liquid nitrogen to generate a glassy matrix. Subsequently, the sample was inserted into the precooled probe. A similar melt-quench procedure was used for the 3.2 mm sapphire rotors, however, a heat gun was used in place of a sand bath.

The NMR experiments involved a train of saturation pulses on the ^{1}H channel with a Rabi frequency of $\omega_1/2\pi = 83$ kHz and 3 µs (5 T and 8.9 T), $\omega_1/2\pi = 152$ kHz and 1.65 µs (9.4 T), and $\omega_1/2\pi = 100$ kHz and 2.5 µs (14.1 T). In all experiments, the interpulse delay of the saturation pulses was 220 µs. The signal was acquired following a recovery period using a solid-echo sequence. The spin-lattice relaxation times T_1 and the DNP buildup times T_B were estimated by fitting monoexponential buildup curves to the signal intensities with varying recovery periods. The DNP enhancement was determined using $\varepsilon = (I/I_0) - 1$, where I denotes the NMR signal intensity with the microwaves on and I_0 denotes the NMR signal intensity with no microwave irradiation, both obtained at a recovery period of 1.3xT_1 or 1.3xT_B, whichever is longer.

Figure 3.3 shows a superposition of the ^{1}H DNP Zeeman frequency profiles recorded as a function of microwave irradiation frequency for 1,3-[α,β,γ,δ-d_{16}]-BDPA (reproduced from Ref. [93]) and d_{21}-BDPA, the latter newly recorded on the 8.9 T DNP spectrometer with the low-power (160 mW) solid-state source. The d_{21}-BDPA sample was degassed using the procedure employed for the 1,3-[α,β,γ,δ-d_{16}]-BDPA sample with the freeze-pump-thaw protocol reported in our previous study[93]. Deuteration of the fluorene moieties in 1,3-[α,β,γ,δ-d_{16}]-BDPA resulted in a negative OE enhancement of $\varepsilon = -13$. However, perdeuteration to yield d_{21}-BDPA resulted in a smaller negative OE enhancement $\varepsilon = -6.4$. These results indicate (see Discussion section) that the ^{1}H spins on the phenyl ring are polarized negatively due to

dominance of DQ cross-relaxation mechanisms in the e-^{1}H systems. The conclusion led us to propose a version of BDPA with only the phenyl ring deuterated so as to quench its negative contributions to the DNP enhancement and obtain a larger positive DNP enhancement than with h_{21}-BDPA.

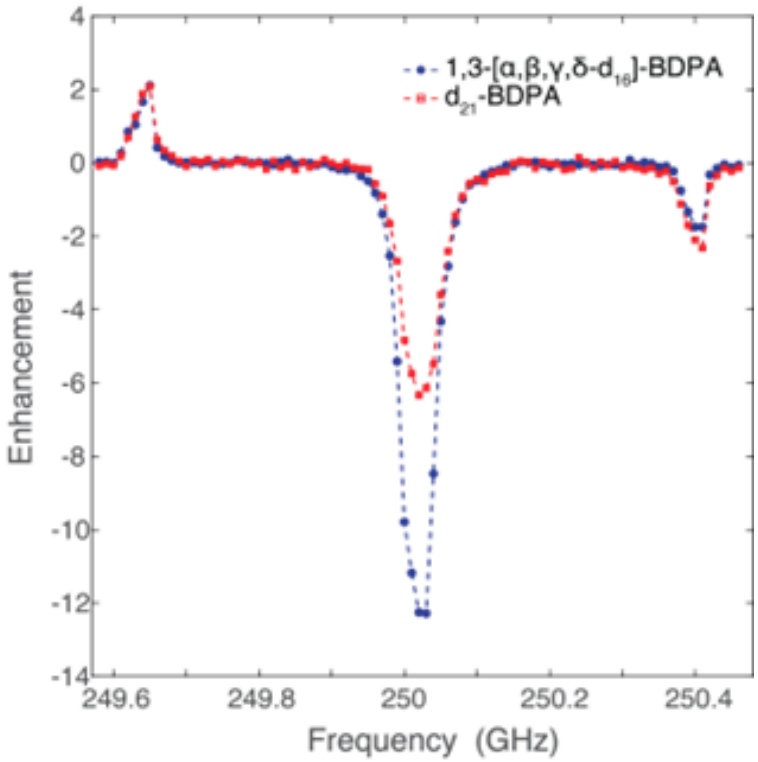

Figure 3.3: DNP frequency profile obtained 8.9 T spectrometer on 1,3-[α,β,γ,δ-d_{16}]-BDPA (blue) and d_{21}-BDPA (red), both spinning at a MAS frequency of 5 kHz and at 90 K. The incident microwave power was 160 mW.

Figure 3.4 shows a series of DNP frequency/field profiles observed for non-degassed h_{21}-BDPA and Phe-d_5-BDPA on the 5 T DNP spectrometer (Figure 3.4a), 8.9 T spectrometer (Figure 3.4b), 9.4 T spectrometer (Figure 3.4c), and the 14.1 T spectrometer (Figure 3.4d). These data were recorded on non-degassed samples as the 5 T and 8.9 T DNP spectrometers utilized a 4 mm rotor, while the 9.4 T and 14.1 T spectrometers utilized a 3.2 mm rotor, for which the samples were transported to a remote lab for experiments, where degassing equipment was not available. The OE enhancements, defined by the intensity of the central peak in each profile, for h_{21}-BDPA and Phe-d_5-BDPA samples were respectively 29 and 64 on the 5 T spectrometer, 36 and 67 on the 8.9 T spectrometer (160 mW), 40 and 70 on the 9.4 T spectrometer, and 49 and 88 on the 14.1 T spectrometer. The results demonstrate that Phe-d_5-BDPA consistently exhibits a higher OE DNP enhancement than the h_{21}-BDPA, at least up to a field strength of 14.1 T.

Table 3.1 summarizes the 1H spin-lattice relaxation times for the sample doped with 2.5% h_{21}-BDPA and Phe-d_5-BDPA as measured at 8.9 T and 14.1 T DNP spectrometers. Table 3.2 lists the enhancement values measured for the two radicals with an incident microwave power of 2 W at 5 T, with an incident microwave power of 160 mW at 8.9 T, and 4.4 W at 250.020

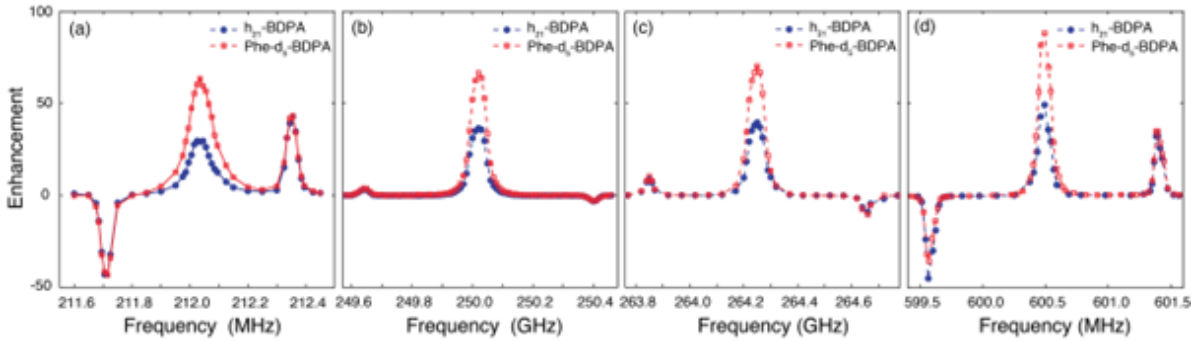

Figure 3.4: (a) DNP field profile obtained at 5 T (b) DNP frequency profile obtained at 8.9 T with a 160 mW low-power microwave source, (c) DNP frequency profile at 9.4 T with a 280 mW low-power microwave source, and (d) DNP field profile at 14.1 T with a gyrotron for h_{21}-BDPA (blue) and Phe-d_5-BDPA (red). The data at 8.9 T was obtained at 90 K, while the data at 9.4 T and 14.1 T were obtained at 100 K. The measurements were made on a sample spinning at a MAS frequency of 3.5 kHz (a) or 5 kHz (b-d).

GHz, with an incident microwave power of 280 mW at 9.4 T and 264.250 GHz, and with an incident microwave power of 30 W at 14.1 T and 395.285 GHz. Using UV-Vis absorption measurements, we determined the relative concentrations of active free radicals between the two samples, both prepared at 2.5 wt%, to be 1.0:1.2 for h_{21}-BDPA and Phe-d_5-BDPA, respectively. The enhancement values adjusted for the relative concentrations are also listed in Table 3.2. This is done since the commercially available BDPA samples were not 100% active. We also note there is no evidence as yet for linear dependence of the enhancement on concentration.

Table 3.1: ^{1}H T_1 and DNP buildup times T_B for h_{21}-BDPA and Phe-d_5-BDPA at 8.9 and 14.1 T.

[Experimentally measured spin-lattice relaxation times (T_1) and DNP buildup times (T_B) for h_{21}-BDPA and Phe-d_5-BDPA at 8.9!T and 14.1 T DNP spectrometers described in the text.]

	h_{21}-BDPA		Phe-d_5-BDPA	
	T_1 (s)	T_B (s)	T_1 (s)	T_B (s)
8.9 T	32.1 ± 2.2	37.5 ± 1.5	38.0 ± 0.4	29.6 ± 0.3
14.1 T	31.9 ± 1.5	30.1 ± 1.5	37.1 ± 3.0	28.9 ± 2.0

Figure 3.5a shows the dependence of the measured DNP enhancement as a function of MAS frequency at the 9.4 T DNP spectrometer. The 3.2 mm sapphire rotor at about 100 K could only spin at a maximum of 12.5 kHz. Figure 3.5b shows the dependence of the measured DNP enhancement as a function of microwave irradiation power at the 9.4 T DNP spectrometer equipped with a solid-state microwave source with a maximum output power of 280 mW (filled circles). There are additional points (empty circles) in the plot showing the DNP enhancements with 14 W of irradiation power for the two polarizing agents obtained on the 8.9 T DNP spectrometer.

Table 3.2: Experimentally measured OE DNP enhancement for 2.5 wt% h_{21}-BDPA and Phe-d_5-BDPA at 5 T with a gyrotron, at 8.9 T with both a low-power microwave source and a gyrotron, at 9.4 T with a low-power source, and 14.1 T with a gyrotron. The enhancement values adjusted for the concentration difference (1.0:1.2) as measured by UV-Vis are listed for h_{21}-BDPA, normalized for Phe-d_5-BDPA.

	h_{21}-BDPA		Phe-d_5-BDPA
	Measured	Adjusted	Measured
5 T / 2 W	29.2	35.0	63.6
8.9 T / 160 mW	36.5	43.8	66.6
8.9 T / 4.4 W	40.7	48.8	70.0
9.4 T / 280 mW	39.7	47.6	70.3
14.1 T / 30 W	49.2	59.0	88.2

3.1.3 Discussion

The OE ideally involves a two-spin system of one electron and one nucleus, hyperfine coupled to each other. The nucleus in our discussion is an ^{1}H spin – either on the BDPA molecule itself or on the surrounding oTP molecules. The excitation of the electron spin transition is followed by unequal cross-relaxation rates in the electron-nuclear two-spin system that can polarize the nuclear spin either positively or negatively. The sign depends on whether the dominant cross-relaxation mechanism is ZQ or DQ, respectively. Cross-relaxation requires time-modulation of the hyperfine coupling and the isotropic component leads to ZQ cross-relaxation while the anisotropic component leads to DQ cross-relaxation. The observed NMR signal is that of the bulk ^{1}H spins in the oTP matrix after they equilibrate with the directly polarized ^{1}H spins in and immediately around the radical. Thus, the observed enhancement in the bulk nuclear spins results from the cumulative contribution of both positive and negative contributions originating in the ^{1}H spins coupled to the electron. In an earlier study, we used the DNP frequency profiles of selectively deuterated BDPA radicals to determine that the strongly coupled ^{1}H spins on the α,γ sites of the fluorene moieties generate a significant positive OE enhancement. In contrast, the weakly hyperfine coupled ^{1}H spins on the β,δ sites on the fluorene moieties primarily aid efficient spin diffusion of the enhanced polarization from the α,γ sites to the bulk ^{1}H spins in the matrix.

Figure 3.3 illustrates an OE enhancement of $\varepsilon = -13$ for 1,3-[α,β,γ,δ-d_{16}]-BDPA, which we reported in our earlier study[93]. This suggests that the ^{1}H spins on the phenyl ring and the oTP molecules in the surrounding matrix cumulatively make a negative contribution to the overall OE enhancement. However, the relative contributions between the ^{1}H spins on the phenyl ring and the surrounding oTP molecules to the overall negative DNP enhancement were unknown. To determine this, in this work, we measured the OE enhancement on d_{21}-BDPA and obtained an enhancement of $\varepsilon = -6.4$. The relative concentrations between the two samples – 1,3-[α,β,γ,δ-d_{16}]-BDPA and d_{21}-BDPA, were determined using UV-vis spectroscopy to be 1.4:1.0, respectively and this is attributed to the partial decay (reduction) of the radicals to different levels. Adjusting for the concentrations, the negative DNP enhancement of 1,3-[α,β,γ,δ-d_{16}]-BDPA was about 45% larger than the negative DNP enhancement obtained

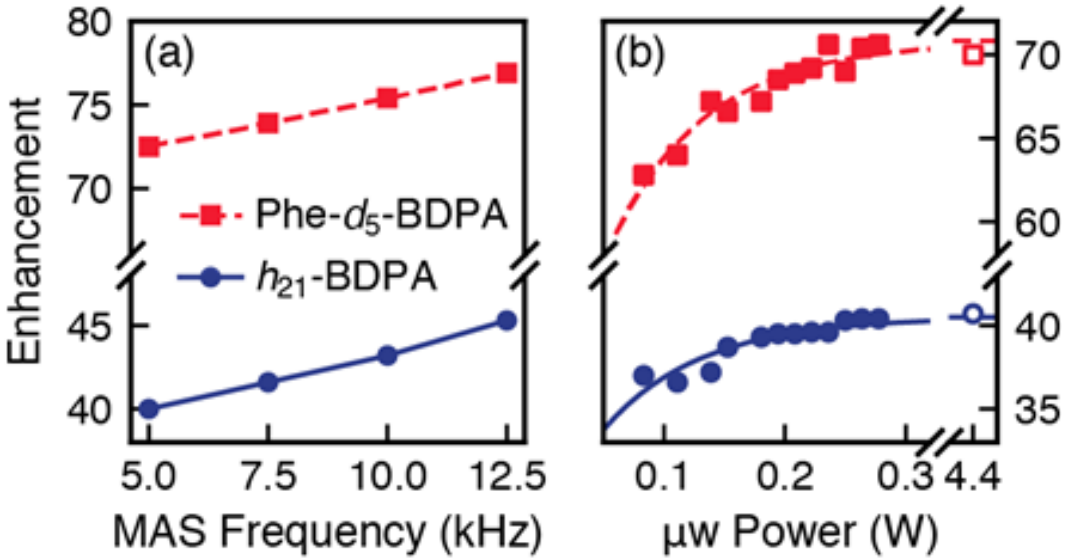

Figure 3.5: Enhancement vs (a) MAS rate and (b) microwave power for h_{21}- and Phe-d_5-BDPA.
Experimental ^{1}H DNP enhancements of h_{21}-BDPA and Phe-d_5-BDPA as a function of (A) MAS frequency and (B) incident microwave power obtained at the 9.4 T DNP spectrometer with a maximum power of 280 mW. The empty circle and square are data points obtained on the 8.9 T DNP spectrometer with an incident microwave power of 4.4 W from a gyrotron. The data in (a) were obtained with an incident microwave power of 280 mW and the data in (b) were obtained with a MAS frequency of 5 kHz.

for d_{21}-BDPA. The result suggests that the ^{1}H spins on the phenyl ring of the BDPA radical and the ^{1}H spins on the surrounding oTP molecules were both individually polarized via a dominant DQ cross-relaxation mechanism in their respective electron-nuclear spin systems. That is, both groups of ^{1}H spins directly contribute to a negative enhancement. This finding leads us to propose that ^{2}H labeling of the phenyl ring in the BDPA radical should lead to higher OE DNP enhancement than observed with the standard h_{21}-BDPA.

Our hypothesis is proven correct, as evidenced by DNP measurements performed in various DNP spectrometers and presented in Figure 3.4. For example, on the 8.9 T DNP spectrometer with the 160 mW microwave source, Phe-d_5-BDPA results in an OE enhancement of 67, in contrast to an enhancement of 36 observed for the standard h_{21}-BDPA. However, UV-vis measurements determined the relative radical concentration between h_{21}-BDPA and Phe-d_5-BDPA samples to be 1.0:1.2. Adjusting for this, Phe-d_5-BDPA exhibits an OE enhancement ∼52% higher than that of h_{21}-BDPA on the 8.9 T spectrometer. Similarly, the increase in enhancement is ∼82%, ∼48%, and ∼50% on the 5 T, 9.4 T, and 14.1 T spectrometers, respectively.

Finally, we verified the dependence of the OE DNP enhancements on MAS frequency and microwave irradiation power for both radicals, as illustrated in Figure 3.5. The experiments were performed on the 9.4 T DNP spectrometer with the low-power microwave source and there is an additional data point in Figure 3.5b performed with 4.4 W microwave irradiation at the 8.9 T DNP spectrometer under otherwise similar experimental conditions. Both the

radicals exhibit increasing enhancement with increasing MAS frequency, while the power dependence appears to saturate with well under 1 W of microwave irradiation, consistent with prior investigations of OE DNP in insulating solids [10, 88, 95]. This is also encouraging for use of compact, lower-cost, low-power solid-state microwave sources.

Based on prior DNP data on selectively deuterated BDPA radicals and newly obtained data on a perdeuterated BDPA radical, we concluded that the ^{1}H spins on the phenyl ring of the BDPA radical participate in OE DNP primarily through DQ cross-relaxation, contributing a negative enhancement. We demonstrated that deuteration of the phenyl ring in the BDPA radical improves the overall positive OE enhancement compared to the standard h_{21}-BDPA by removing contributions to DQ cross-relaxation. We verified the hypothesis by synthesizing the newly proposed Phe-d_5-BDPA radical and examining its DNP properties in several spectrometers. In the magnetic field range of 5 – 14.1 T, the Phe-d_5-BDPA polarizing agent improves the OE DNP enhancement by about 50% when adjusted for the concentrations of active radicals in the sample, compared to the standard h_{21}-BDPA in the oTP matrix and has achieved a maximum enhancement of ∼90 at 14.1 T at a MAS frequency of 5 kHz at 100K – highest OE at these conditions to date for a non-degassed sample and is expected to improve further by a factor of ∼70% with freeze-pump-thaw degassing as demonstrated in our earlier study[93]. These results offer insight into designing new or modifying existing polarizing agents to exhibit amplified OE DNP. Considering the improvement of OE with stronger magnetic field strengths as shown here, in stark contrast to other CW-DNP mechanisms, the results discussed are of prime importance to achieve efficient sensitivity enhancements in high-resolution solid-state NMR of biological macromolecules. The work presented here also underscores the rationale for pursuing low-power solid-state microwave sources for use at high magnetic field strengths.

3.2 Resonant Mixing DNP

This section is reproduced from the published article[96]: *Resonant Mixing Dynamic Nuclear Polarization*, **J. Phys. Chem. Lett. 2023**, *14*, 7007-7013, with minimal formatting changes for thesis integration. The content is included with permission from the publisher.

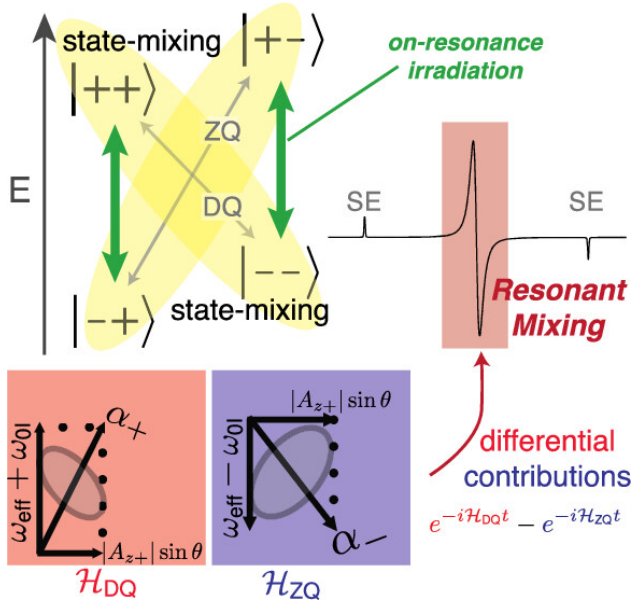

Figure 3.6: Resonant mixing is enabled by differential contributions of DQ and ZQ pathways, which leads to a dispersive feature in the center.

3.2.1 Introduction

Dynamic nuclear polarization (DNP) is used to enhance the polarization of nuclear spins by transferring polarization from unpaired electrons via microwave irradiation. [97] In the last two decades high-frequency DNP has evolved as a powerful and widely applicable technique to mitigate the chronic issue of sensitivity in nuclear magnetic resonance (NMR) spectroscopy. [98, 99] Microwave-driven DNP has been used in protein structural studies, [5, 62, 63, 65, 100–106] to solve a variety of problems in materials science, [107–109] and in applications of magnetic resonance imaging (MRI) of materials [110] and using dissolution-DNP. [111, 112] Descriptions of the theoretical background of DNP can be found in review articles and one monograph. [57, 71, 98, 99, 113–116].

The four well-known mechanisms used in continuous wave (CW) DNP experiments are the Overhauser effect (OE), solid effect (SE), cross effect (CE), and thermal mixing (TM). The conventional understanding of the OE and the related nuclear Overhauser effect (NOE) is that they require rapid molecular motion governing the relaxation of the electron or nuclear spins; accordingly, these effects are expected in conducting solids (metals and low dimensional conductors) and liquids. To arise in insulating solids, the OE requires specific structural details of the radical molecule (e.g., BDPA). [10] In the case of OE DNP using electrons, irradiation near the electron Larmor frequency yields a symmetric absorptive DNP Zeeman

field profile centered on the electron paramagnetic resonance (EPR) line. In contrast, the SE, CE, and TM do not require dynamic spins, are manifested in insulating solids, and yield asymmetric Zeeman profiles. The SE requires off-resonance irradiation to excite the forbidden DNP transitions at $\omega_{0S} \pm \omega_{0I}$, where ω_{0S} and ω_{0I} are the electron and nuclear Larmor frequencies respectively, and is prominent for narrow-line polarizing agents (PAs) for which this condition is more uniformly satisfied. The CE and TM result from three-spin (e-e-n) systems and yield dispersive field profiles whose shape depends on the details of the EPR spectrum.

In this paper, we consider insulating solids in a strong magnetic field and doped with a PA, trityl, whose EPR line width $\Delta\omega_{0S}/2\pi$ is much narrower than the nuclear Larmor frequency $\omega_{0I}/2\pi$. This system should exhibit a strong SE, while other CW mechanisms are not expected. The CE requires pairs of electron spins with their Larmor frequencies separated by the nuclear Larmor frequency; i.e., $\omega_{0S} \geq \omega_{0I}$. We have mentioned that the OE is not expected in insulating solids, but even if it were present, the differing zero quantum (ZQ) and double quantum (DQ) cross-relaxation rates would yield a symmetric enhancement profile centered about the electron Larmor frequency. [10, 59, 86, 88, 93]

However, about a decade ago [98, 117, 118] and more recently in high-field DNP experiments using trityl radicals, a dispersive DNP field profile was observed near the electron Larmor frequency. [119–121] The dispersive shape suggests that it is not OE, leaving only TM among the CW mechanisms. TM is present when strong electron–electron couplings lead to a homogeneously broadened EPR spectrum that must be broader than the nuclear Larmor frequency. These conditions are unlikely in the case of trityl: trityl molecules are bulky, and the coupling between a pair of radicals cannot be much larger than about 50 MHz. [122, 123] Even in a multielectron cluster, the maximum possible EPR frequency shift is well below the 1H Larmor frequency at fields where these profiles have been observed.

Karabanov et al. [121] observed a well-resolved dispersive profile near the EPR center with a trityl concentration of only 15 mM; that this profile appears under these conditions further suggests that the mechanism at play is not TM and probably is an effect involving a single electron spin interacting with surrounding nuclear spins. We have also looked for direct evidence of TM in a trityl system, [124] but we found that even with aggregation of the trityl radicals, the electron–electron interaction is not strong enough to induce three-spin flips involved in TM and that the spin temperature of the ^{13}C is completely decoupled from ^{1}H. The spin temperatures of ^{13}C and ^{1}H can even have different signs with microwave irradiation, completely contrary to the conceptual picture of TM. [124]

In order to rationalize these observations and the dispersive Zeeman DNP field profile, we propose a new mechanism termed resonance mixing (RM). We first present additional experimental profiles illustrating the effect, acquired under conditions under which we argue TM should not be present. Next, we simulate the experimental curves by using a model consisting of a single electron and a single nuclear spin. As these simulations involve only a single electron spin, they cannot support a TM process. We then provide a qualitative analytical derivation explaining the origin of the observed enhancement and show that it yields a dispersive Zeeman profile in accordance with the simulation result.

3.2.2 Experiments and Analysis

We begin with the experimental ^{1}H DNP field profile of 80 mM trityl-OX063 in d_6-DMSO:D_2O:H_2O (6:3:1), recorded at $\omega_{0I}/2\pi = 600$ MHz (Figure **??**). For this experiment, the sample was spun at $\omega_r/2\pi = 8$ kHz at 95 K, and microwave irradiation was provided by a 17 W gyrotron microwave source. We observe the characteristic dispersive profile near the center with a maximum enhancement of ∼5. The relatively high field quenches TM as the nuclear Larmor frequency is too high for the field-independent electron–electron couplings, supporting the argument that the center DNP field profile is due to RM rather than TM. An alternative perspective with the same conclusion is that if the electron–electron coupling were greater than 600 MHz to allow TM at this field, then TM would be much stronger at low fields, which is not the case. We have also recorded a Zeeman field profile for 100 mM trityl-OX063 in d_6-DMSO:D_2O:H_2O (6:3:1) at $\omega_{0I}/2\pi = 380$ MHz, $\omega_r/2\pi = 6$ kHz, and T = 95 K (Figure 3.8). Microwave irradiation was provided by a 160 mW solid state source, [125] and again we observed a modest enhancement ∼5 instead of ∼100 observed at 20 K. [120] The extreme temperature dependence suggests that relaxation properties are critical to the observed dispersive profiles.

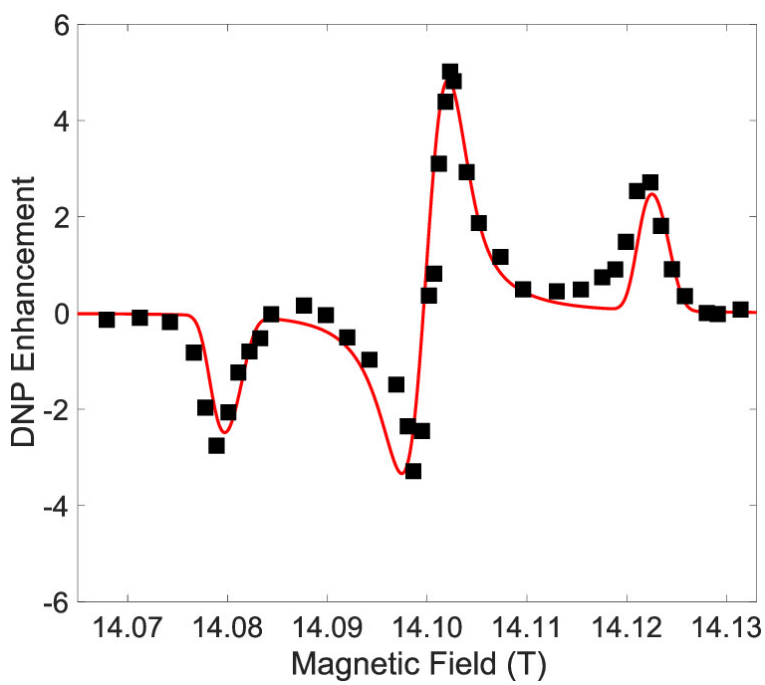

Figure 3.7: DNP field profile for an 80 mM Trityl-OX063 in a d_6-DMSO:D_2O:H_2O (6:3:1) sample at $\omega_{0I}/2\pi = 600$ MHz, 95 K, and $\omega_r/2\pi = 8$ kHz. The sample was irradiated with a gyrotron. The solid line is the Spin Evolution simulation of a dipolar coupled electron–nuclear spin pair using the following parameters: $\omega_1/2\pi = 1.6$ MHz, $T_{1e} = 1$ ms, $T_{2e} = 0.2$ µs and the cross relaxation times $T_{1ZQ} = 0.99975$ ms, $T_{1DQ} = 1$ ms, $T_{2ZQ} = T_{2DQ} = 0.2$ µs.

For further insight into the EPR properties of trityl at high field, echo-detected EPR spectra were recorded with a 140 GHz EPR spectrometer at 80 K for an 80 mM sample and compared to results from an 8 mM sample, as shown in Figure 3.9. We observe a

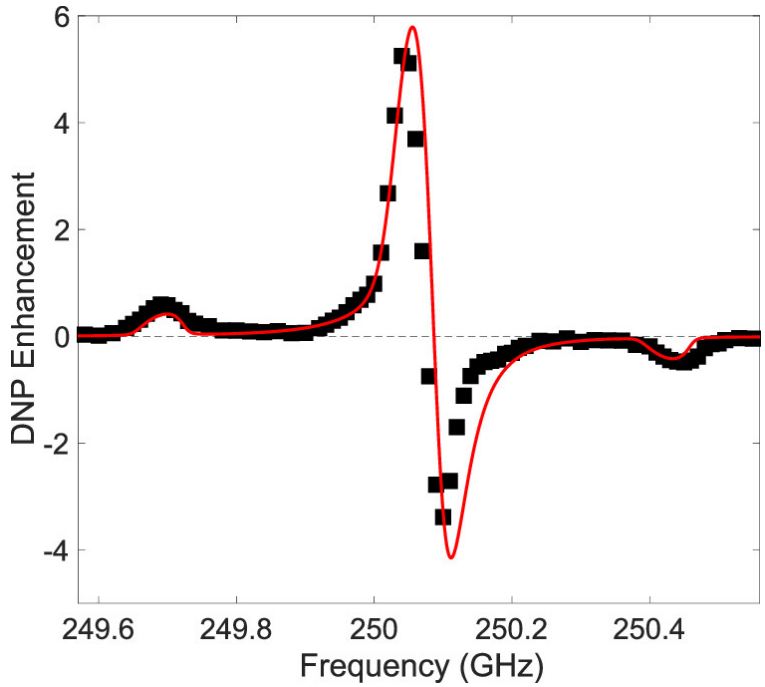

Figure 3.8: DNP field profile for an 100 mM Trityl-OX063 in a d_6-DMSO:D_2O:H_2O (6:3:1) sample at $\omega_{0I}/2\pi$ = 380 MHz, 100 K with a 6 kHz spinning rate, irradiated by a 160 mW solid state source. The solid line is the SpinEvolution simulation of a dipolar coupled electron–nuclear spin pair using the following parameters: $\omega_1/2\pi = 0.25$ MHz, $T_{1e} = 4$ ms, $T_{2e} = 0.05$ µs and the cross relaxations $T_{1ZQ} = 1.9995$ ms, $T_{1DQ} = 2$ ms, and $T_{2ZQ} = T_{2DQ}$ = 0.05 µs.

small asymmetry in the line shape from the g-anisotropy, which should contribute about 140 $GHz \times \frac{2.0032-2.00262}{2} \approx 40\ MHz$ line width (the g-tensor values are taken from the literature [126]). The detected line width is 45 G ≈ 120 MHz for both samples. The extra broadening from 8 to 80 mM is ∼11 MHz. Thus, the electron–electron dipolar interaction should be below 100 MHz as predicted from the size of the trityl radicals. Assuming a homogeneous distribution of radicals in the solvent, we estimate the distance between the electron spins for the 80 mM sample to be 2.7 nm, corresponding to an electron–electron dipolar interaction of 8 MHz and in agreement with the observed additional line broadening from 8 to 80 mM. Therefore, our EPR study argues against the proposition of thermal mixing, as the EPR line width, though broadened by the electron–electron dipolar interaction, remains below the ^{1}H Larmor frequency of 212 MHz. Thus, fundamental triple spin-flip processes for thermal mixing are attenuated. In going from 140 to 395 GHz (^{1}H Larmor frequency 600 MHz), the g-anisotropy of trityl will broaden the EPR line by another ∼60 MHz, while the electron–electron dipolar interaction is invariant, further attenuating TM.

Together with the experimental data in Figure 3.7 and Figure 3.8, we show simulation results for a model system of a simple dipolar coupled electron–nuclear spin pair using the SpinEvolution [35] software. For the simulations, we plot the static nuclear polarization under CW microwave irradiation by using typical T_{1e} and T_{2e} values for samples with these concentrations. A small difference between the ZQ and DQ cross-relaxation rates is introduced

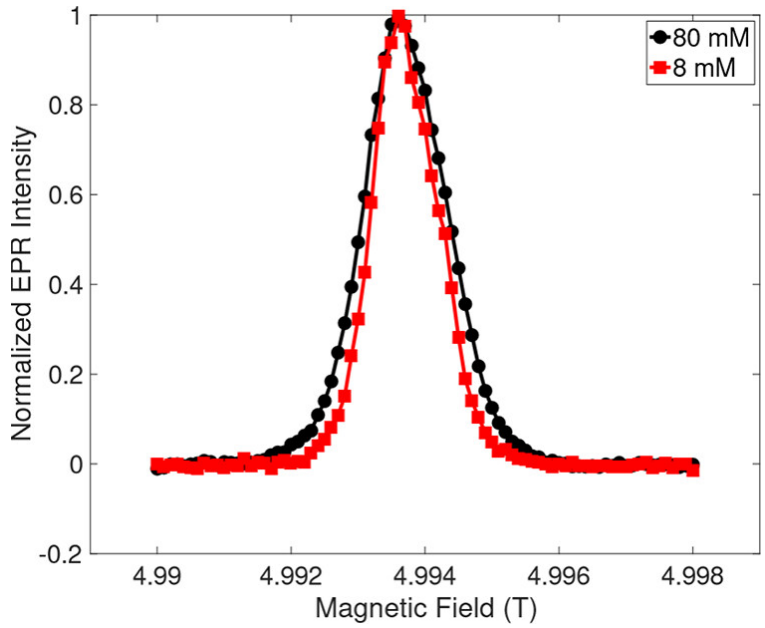

Figure 3.9: Echo detected EPR spectra of 8 and 80 mM trityl in d_6-DMSO, D_2O and H_2O (60:30:10) matrices at 140 GHz and 80 K.

to fit the slight asymmetry between the positive and negative RM enhancements. If the ZQ and DQ cross-relaxation rates are the same, then an antisymmetric RM DNP field profile should be obtained, e.g., the dashed line in Figure 3.10. An even larger difference between the two cross-relaxation rates would lead to an absorptive profile and deemed Overhauser DNP. In SpinEvolution, the transverse cross-relaxation rates are simply defined as the relaxation of the off-diagonal elements of the density matrix as in the Solomon equations. [127]

In an attempt to understand this dispersive shape of the DNP field profile, we further performed simulation studies using SpinEvolution. [35] The results are presented in Figure 3.10 for a system consisting of a single $S = 1/2$ electron spin interacting with a single $I = 1/2$ nuclear spin. Even without any relaxation effects incorporated into the simulation, we observe a weakly dispersive DNP profile at the EPR resonance. In the absence of cross-relaxation, we cannot attribute the enhancement to the OE. As the simulation involves only a single electron and thus no multielectron effects, we also exclude the CE and TM mechanisms. Finally, the position of the dispersive profile precludes the SE.

3.2.3 Theory

In order to obtain further insight, we continue with an analytic treatment of a coupled electron–nuclear spin pair. We assume an initially diagonal density matrix with full electron polarization and zero nuclear polarization. We show that microwave irradiation near the center of the EPR line mixes states resulting in polarization transfer to the nuclear spin and that the polarization profile is dispersive.

Our treatment does not incorporate relaxation or spectral broadening mechanisms, which permit a description of the time development of the nuclear polarization process. However, it does reveal a new DNP mechanism, different from the OE, SE, CE, and TM. Our treatment

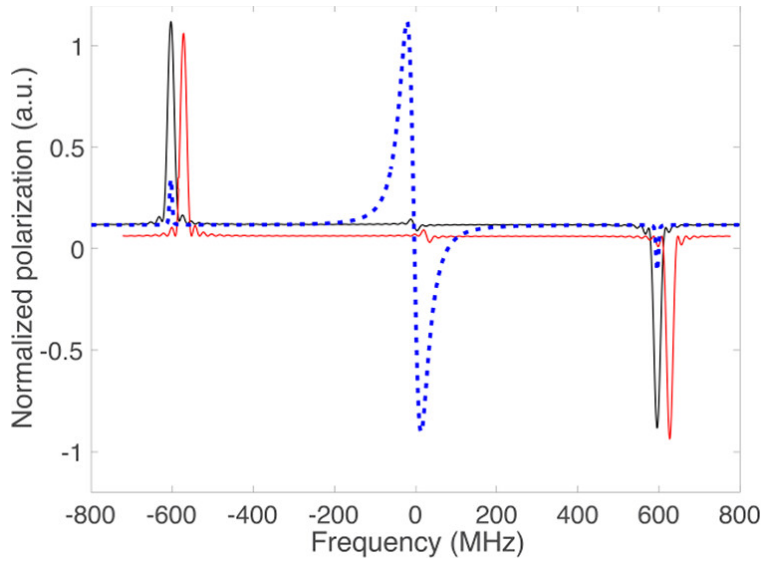

Figure 3.10: DNP Zeeman field profile from a SpinEvolution simulation (black) and an analytical calculation using Equation 3.5 (red) for 1 electron spin interacting with 1 nuclear spin. The red trace is offset from the simulation for clarity. The following parameters are used, $\omega_{0I}/2\pi = 600$ MHz, $\omega_1/2\pi = 0.5$ MHz at t = 50 ns (in the order of the spin coherence time T_{2e}). The dotted line (blue) shows the SpinEvolution simulation in the case of CW irradiation using the following relaxation times: $T_{1e} = 1$ ms and $T_{2e} = 0.2$ µs and the cross relaxations $T_{1ZQ} = T_{1DQ} = 1$ ms and $T_{2ZQ} = T_{2DQ} = 0.2$ µs.

also explains our use of the term ***resonant mixing (RM)***: it originates from state mixing induced by microwave irradiation near the EPR frequency.

We start by following the treatment for coherent DNP described in the references. [57, 80, 123] We consider a system consisting of a single S = 1/2 electron spin interacting with a single I = 1/2 nuclear spin in the presence of a static magnetic and a microwave field. Per usual, we choose the z-axis of the laboratory frame of reference along the static magnetic field and the x-axis along the microwave field. In a frame rotating with the microwave frequency ω_m about the z-axis, and with $\hbar = 1$, the truncated spin Hamiltonian is then,

$$\mathcal{H} = (\omega_{0S} - \omega_m)S_z + \omega_{1S}S_x - \omega_{0I}I_z + S_zA_{zz}I_z + \frac{1}{2}S_z\left(A_{z-}I_+ + A_{z+}I_-\right) \tag{3.1}$$

The first two terms represent the Zeeman and microwave Hamiltonians of the electron spin in the rotating frame, where $\omega_{0S} - \omega_m$ is the electron resonance offset and ω_{1S} the electron Rabi frequency. The next term is the nuclear Zeeman interaction, where ω_{0I} is the nuclear Larmor frequency. Finally, the last term is part of the dipolar interaction between the electron and nuclear spin, where $I_\pm = I_x \pm iI_y$. As in the description of nuclear orientation via electron spin locking (NOVEL) and the integrated solid effect (ISE) we neglect the $S_zA_{zz}I_z$ term in the dipolar interaction. [39, 49, 128]

Our aim is to determine the evolution of the nuclear polarization $P_I(t)$,

$$P_I(t) = \frac{1}{I} \cdot \frac{\mathrm{Tr}\left\{\rho(t)I_z\right\}}{\mathrm{Tr}\left\{\rho(t)\right\}} \tag{3.2}$$

and the electron polarization,

$$P_S(t) = -\frac{1}{S} \cdot \frac{\mathrm{Tr}\left\{\rho(t) S_z\right\}}{\mathrm{Tr}\left\{\rho(t)\right\}} \tag{3.3}$$

after switching on the microwave field, and assuming initial conditions $P_I(0) = 0$ and $P_S(0) = P_0$. Here ρ(t) is the density matrix.

In the first step, we tilt the frame of reference for the electron spin by θ such that $\tan\theta = \omega_{1S}/(\omega_{0S} - \omega_m)$. Thus, the $\tilde{z}$-axis of the tilted rotating frame is aligned along the effective field. Next, we construct the matrix representation of the Hamiltonian using the basis states,

$$|m_{\tilde{S}}, m_I\rangle = \left|+\tfrac{1}{2}, -\tfrac{1}{2}\right\rangle, \quad \left|-\tfrac{1}{2}, -\tfrac{1}{2}\right\rangle, \quad \left|+\tfrac{1}{2}, +\tfrac{1}{2}\right\rangle, \quad \left|-\tfrac{1}{2}, +\tfrac{1}{2}\right\rangle$$

of the $\tilde{z}$-component of $\tilde{S}$ in the tilted rotating frame and the z-component of I in the laboratory frame:

$$\frac{1}{2}\begin{pmatrix} \omega_{\mathrm{e}\square} + \omega_{0I} & 0 & \frac{1}{2}A_{z+}\cos\theta & -\frac{1}{2}A_{z-}\sin\theta \\ 0 & -\omega_{\mathrm{e}\square} + \omega_{0I} & -\frac{1}{2}A_{z-}\sin\theta & -\frac{1}{2}A_{z+}\cos\theta \\ \frac{1}{2}A_{z-}\cos\theta & -\frac{1}{2}A_{z+}\sin\theta & \omega_{\mathrm{e}\square} - \omega_{0I} & 0 \\ -\frac{1}{2}A_{z+}\sin\theta & -\frac{1}{2}A_{z-}\cos\theta & 0 & -\omega_{\mathrm{e}\square} - \omega_{0I} \end{pmatrix} \tag{3.4}$$

Here $\omega_{\mathrm{e}\square} = \sqrt{(\omega_{0S} - \omega_m)^2 + \omega_{1S}^2}$ is the effective resonance frequency of the electron spin in the tilted rotating frame.

The matrix elements $\pm\frac{1}{2}A_{z\pm}\cos\theta$ only mix nuclear spin states, but not nuclear and electron spin states, so these terms do not contribute to polarization transfer between the two spins, and we ignore them in what follows. [39, 128] Thus, the matrix representation reduces to two independent 2×2 submatrices-one corresponding to zero quantum (ZQ) transitions (the central four elements 22, 23, 32, and 33) and one corresponding to double quantum (DQ) transitions (the outer four elements 11, 14, 41, and 44)-allowing us to solve the Liouville–von Neumann equation analytically. The procedure is straightforward; see, for instance, the previous treatment of the solid effect, [57] NOVEL, and ISE. [39, 49, 128] The ZQ and DQ transitions give different signs of the polarization transfer. Accordingly, we subtract the contribution of the ZQ and DQ transitions and find

$$P_I = -P_0 \cos\theta \sin^2\theta \left|\tfrac{1}{2}A_{z+}\right|^2 \times \left[\frac{1}{\alpha_-^2}(1 - \cos(\alpha_- t)) - \frac{1}{\alpha_+^2}(1 - \cos(\alpha_+ t))\right] \tag{3.5}$$

for the evolution of nuclear polarization. Here we define

$$\alpha_\pm = \sqrt{(\omega_{\mathrm{e}\square} \pm \omega_{0I})^2 + \left|\tfrac{1}{2}A_{z+}\right|^2 \sin^2\theta} \tag{3.6}$$

and P_0 as the initial electron polarization.

In the SE and related mechanisms like NOVEL and ISE, the nuclear polarization occurs at $\omega_{eff} \approx \omega_{0I}$, but here we are interested in the growth of nuclear polarization when $\omega_{eff} \ll \omega_{0I}$.

To explore this limit, we rewrite the expression for $P_I(t)$ as

$$\begin{aligned} P_I = & -P_0 \cos\theta \, \sin^2\theta \, \left|\tfrac{1}{2}A_{z+}\right|^2 \times \Bigg\{ \left[\frac{1}{\alpha_-^2} + \frac{1}{\alpha_+^2}\right] \sin\left(\frac{\alpha_- - \alpha_+}{2}t\right) \sin\left(\frac{\alpha_- + \alpha_+}{2}t\right) \\ & + \left[\frac{1}{\alpha_-^2} - \frac{1}{\alpha_+^2}\right] \left[2 - \cos\left(\frac{\alpha_- - \alpha_+}{2}t\right) \cos\left(\frac{\alpha_- + \alpha_+}{2}t\right)\right] \Bigg\} \end{aligned} \tag{3.7}$$

In addition to $\omega_{eff} \ll \omega_{0I}$, we also have $|\frac{1}{2}A_{z+}| \ll \omega_{0I}$, so we can expand

$$\alpha_\pm^2 = \omega_{0I}^2 \left(1 - x_\pm\right) \tag{3.8}$$

where

$$|x_\pm| = \left| \pm \frac{2\omega_{\mathsf{e}\square}}{\omega_{0I}} + \frac{\omega_{\mathsf{e}\square}^2}{\omega_{0I}^2} + \frac{\sigma^2}{\omega_{0I}^2} \right| \ll 1 \tag{3.9}$$

Then

$$\begin{aligned} \frac{1}{\alpha_-^2} - \frac{1}{\alpha_+^2} &\approx \frac{4\omega_{\mathsf{e}\square}}{\omega_{0I}^3} \\ \frac{1}{\alpha_-^2} + \frac{1}{\alpha_+^2} &\approx \frac{2}{\omega_{0I}^2} \\ \alpha_- + \alpha_+ &\approx 2\omega_{0I} \\ \alpha_- - \alpha_+ &\approx -2\omega_{\mathsf{e}\square} \end{aligned} \tag{3.10}$$

and

$$\begin{aligned} P_I = & -P_0 \cos\theta \, \sin^2\theta \, \left|\tfrac{1}{2}A_{z+}\right|^2 \times \Bigg\{ -\frac{2}{\omega_{0I}^2} \sin(\omega_{\mathsf{e}\square} t) \sin(\omega_{0I} t) \\ & + \frac{4\omega_{\mathsf{e}\square}}{\omega_{0I}^3} \left[2 - \cos(\omega_{\mathsf{e}\square} t) \cos(\omega_{0I} t)\right] \Bigg\} \end{aligned} \tag{3.11}$$

We average over the terms oscillating with the NMR frequency in a similar way as is customary in Hamiltonian theory. Then also inserting the definition of θ and ω_{eff}, we find that the polarization is increased from zero to

$$P_I = -P_0 \cdot \frac{2\left|A_{z+}\right|^2 \omega_{1S}^2}{\omega_{0I}^3} \cdot \frac{(\omega_{0S} - \omega_m)}{(\omega_{0S} - \omega_m)^2 + \omega_{1S}^2} \tag{3.12}$$

The resulting polarization has the shape of a derivative of a Lorentzian as a function of the microwave frequency. Thus, our analytical treatment yields the same dispersive field profile for the enhancement as those from our simulations presented above. It moreover shows that this enhancement is due to the mixing of the electron and nuclear spin states induced by the microwave field when it is tuned near the resonance frequency of the electron spins. It is also a differential effect because the resulting nuclear polarization is the difference between the contributions of the ZQ and the DQ submatrices.

The resulting nuclear polarization 3.12 is still small, but as noticed above, our intention is only to demonstrate the existence of RM. A more elaborate treatment yielding the growth of P_I as a function of time and the final polarization that can be reached requires the inclusion

of electron and nuclear relaxation processes, as well as homogeneous and inhomogeneous EPR line broadening. This will be the subject of further investigation.

Since RM and the SE involve the same spin interactions, Equation 3.5 predicts both effects, as is illustrated in the red curve in Figure 3.10, where an analytical calculation of the DNP field profile using 3.5 matches the numerical simulation result in black. Note that running the simulation over a time window T_{2e} corresponds to introducing a homogeneous broadening with $D \sim T_{2e}^{-1}$. From the solid lines in Figures 3.7 and 3.8 as well as the dashed line in Figure 3.10, we already see that RM can dominate the DNP field profile when relaxation and EPR line is incorporated. Furthermore, these simulation results also illustrate that the maxima of eq 3.12 are shifted by the EPR line broadening.

3.2.4 Conclusion

In summary, we propose a new DNP mechanism, Resonant Mixing (RM), mediated by state mixing of microwaves and hyperfine interaction. It results in a dispersive DNP field profile when microwave irradiation is applied near the EPR resonance; hence, the name. The Zeeman field profile is similar to that observed for TM, and we believe that RM explains the DNP Zeeman field profile of some recently published trityl data. [120, 124] RM is induced by the microwave and the hyperfine interaction, just as for the SE. However, SE transitions occur when the microwave field is off-resonance at $\omega_{0S} \pm \omega_{0I}$. In contrast the nuclear polarization in RM is enhanced when the electron and nuclear spin states are mixed by an on-resonance microwave field.

We have provided experimental observations of the RM and justification of its origin through both numerical simulation and analytical calculations. Our analytical treatment does not yet include relaxation, and further studies will require incorporating relaxation in the theory as well as targeted experimental measurements of RM enhancements and relevant parameters.

Finally, we point out that this is the first proposition of the resonant mixing DNP mechanism. RM could be a method to enhance MAS NMR to study biomolecules where high magnetic fields are essential for high-resolution NMR, and where microwave power is limited. Karabanov et al. [121] showed a strong effect with trityl compared to SE, and more recently, an enhancement of 110 has been observed for by Equbal et al., [120] illustrating the potential. We believe that understanding the RM mechanism can provide a new path to improve DNP enhancements and expect advances in understanding this mechanism in the future.

3.3 Resonant Mixing DNP with Overhauser Effect

This section is an article in preparation: *Resonant Mixing Dynamic Nuclear Polarization* with multiple formatting changes for thesis integration.

3.3.1 Introduction

Nuclear magnetic resonance (NMR) is a versatile analytical technique that exploits the magnetic properties of nuclear spins and has become an indispensable tool to probe the chemical and physical properties of a wide range of materials. However, the lower sensitivity of the technique, which is due to the low nuclear spin magnetic moment, is a persistent challenge. For the last two decades, dynamic nuclear polarization (DNP) has become the method of choice to address this issue [6, 98–100]. By transferring polarization from highly polarized electron spins to the surrounding nuclear spins, DNP can dramatically increase the signal intensities in NMR experiments. This polarization transfer is achieved through microwave excitation of electron-nuclear transitions associated with unpaired electrons of a polarizing agent (PA), such as stable free radical or paramagnetic metal complex. The enhanced sensitivity provided by DNP opens new possibilities for studying complex biological systems [5, 62, 63, 65, 100–106], addressing various issues in materials science [107–109], and facilitating applications in magnetic resonance imaging (MRI) [110–112].

The usual explanations of continuous wave (CW) DNP rely on four well-known mechanisms: the Overhauser effect (OE), the solid effect (SE), the cross effect (CE) and thermal mixing (TM). The OE is mediated by cross-relaxation between the electron and the nuclear spins, and involves irradiation close to the electron Larmor frequency to generate a symmetric positive or negative absorptive DNP Zeeman field profile. The SE mechanism requires off-resonance irradiation to excite the forbidden transitions at $\omega_{0S} \pm \omega_{0I}$, where ω_{0S} and ω_{0I} represent the electron and nuclear Larmor frequencies, respectively. The SE Zeeman profile consists of positive and negative enhancements at the two frequencies. The CE mechanism involves a three spin (e-e-n) flip-flop process and yields a dispersive field profile with characteristics dependent on the details of the electron paramagnetic resonance (EPR) spectrum. The TM mechanism is similar, but involves multiple coupled electrons and a homogeneously broaden EPR spectrum.

In addition, the conventional wisdom is that OE is the dominant mechanism in liquids or conducting solids where the electrons are mobile, whereas the SE, CE and TM are dominant in relatively rigid insulating solids. However, recent experimental results have challenged these conventions. In particular, when the PA 1,3-bisdiphenylene-2-phenylallyl (BDPA) and similar molecules are dispersed in a matrix of rigid ortho-terphenyl (oTP), an insulating solid, positive absorptive DNP Zeeman profiles were observed near the electron paramagnetic resonance (EPR) center [10, 59, 88, 91–93]. When the fluorneyl rings of BDPA are perdeuterated, the field profile is negative absorptive[10, 92, 93]. This behavior is indicative of the OE, and contradicts conventional expectations. In contrast, trityl radicals exhibit a weak dispersive shape feature in their DNP Zeeman profiles near the EPR center [10, 96, 119, 120, 124], which cannot be readily explained by the four established DNP mechanisms. Finally, there is other experimental data where BDPA displays a dispersive DNP field profile similar to trityl

near the EPR center instead of an OE. [78, 129, 130]. These intriguing findings underscore the evolving complexities in our understanding of DNP mechanisms, stimulating further exploration and refinement of the existing theoretical frameworks.

Recently, we proposed a novel DNP mechanism, ***Resonant Mixing (RM)*** [96]. in which nuclear polarization enhancement originates from state mixing of the electron and nuclear spins. In addition, it is present for the simplest system of a hyperfine coupled electron-nuclear spin pair and in these respects, RM is similar to the SE. However, RM is optimal when the microwave irradiation is on-resonance with the EPR transitions instead of at the forbidden transitions at $\omega_{0S} \pm \omega_{0I}$ as for the SE. RM should lead to a dispersive shaped DNP field profile, and we believe it is responsible for the DNP enhancement using trityl radicals. In the previous publication [96], the system was addressed using a coherent approach, but relaxation effects were neglected. This permitted a rigorous calculation of the evolution of the density matrix, and provided insights into the underlying mechanisms responsible for the DNP enhancement. However, in practical scenarios involving CW microwave irradiation, relaxation processes must be considered and the focus shifts to determining the stationary solution for nuclear polarization in the presence of these processes. This adjustment in perspective becomes crucial for a more accurate representation of the DNP phenomenon under CW irradiation conditions, recognizing the dynamic interplay between polarization transfer and relaxation processes.

In this paper, we present a theoretical framework to incorporate relaxation processes into the calculation with the aim of deriving the static nuclear polarization for a hyperfine-coupled electron-nuclear spin pair. Our approach utilizes Bloch theory [30], augmented by the inclusion of cross-relaxation processes proposed by Solomon [127]. A similar methodology for treating relaxation was successfully applied by Vega, et al. to explain the CW SE [11] . Our theoretical exploration reveals that OE and RM are fundamentally related. Specifically, if the zero-quantum (ZQ) and double-quantum (DQ) relaxation rates are assumed to be identical (or neglected, as in [96]), a dispersive DNP field profile emerges near the EPR center, i.e. RM. Conversely, when ZQ and DQ relaxation rates differ, an absorptive DNP field profile characteristic of the OE can be observed. This theoretical framework elucidates the origin of an asymmetric dispersive shape, consistent with slightly different cross-relaxation processes observed previously [50, 124].

3.3.2 Theory

Our aim is to incorporate the relaxation and linewidth in the calculation of the stationary nuclear polarization in the presence of a perturbing microwave field. We follow the analytic treatment of a coupled electron-nuclear spin pair and first introduce relaxation terms. We assume an initially diagonal density matrix with full electron polarization and zero nuclear polarization in the absence of microwaves. The Hamiltonian in the rotating frame can be written as

$$\begin{aligned} \mathcal{H} &= \hbar[(\omega_{0S} - \omega_{\mathrm{m}})S_z + \omega_1 S_x + \Gamma - \omega_{0I} I_z \\ &\quad + S_z A_{zz} I_z + \tfrac{1}{2} S_z \left(A_{z-} I_+ + A_{z+} I_-\right)] \\ &= \mathcal{H}_{0S} + \mathcal{Z}_{0I} + A_{zz} S_z I_z + \mathcal{H}_{SI}, \end{aligned} \tag{3.13}$$

The first two terms represent the Zeeman and microwave Hamiltonians of the electron spin in the rotating frame, where $\Omega = \omega_{0S} - \omega_{\mathrm{m}}$ is the electron resonance offset and ω_{m} the electron Rabi frequency. The third term, Γ, accounts for the electron spin lattice relaxation, T_{1e} and the electron spin and the electron spin bath controlling T_{2e}. The next term is the nuclear Zeeman interaction, where ω_{0I} is the nuclear Larmor frequency. Finally, the last terms are the truncated dipolar interaction between the electron and nuclear spin, where $I_{\pm} = I_x \pm iI_y$ and A is the coupling. We denote the first three terms, which only involve electron spin operators, as $\mathcal{H}_{0S}$, the nuclear Zeeman term as Z_{0I}, and the dipolar coupling term as $\mathcal{H}_{SI}$.

Next we construct the matrix representation of the Hamiltonian using the eigenstates, $|m_{\tilde{S}}, m_I\rangle = |+\frac{1}{2}, -\frac{1}{2}\rangle$, $|-\frac{1}{2}, -\frac{1}{2}\rangle$, $|+\frac{1}{2}, +\frac{1}{2}\rangle$, $|-\frac{1}{2}, +\frac{1}{2}\rangle$:

$$\frac{\hbar}{2}\begin{pmatrix} \Omega + \omega_{0I} + A_{zz} & \omega_1 & \frac{1}{2}A_{z+} & 0 \\ \omega_1 & -\Omega + \omega_{0I} - A_{zz} & 0 & -\frac{1}{2}A_{z-} \\ \frac{1}{2}A_{z-} & 0 & \Omega - \omega_{0I} - A_{zz} & \omega_1 \\ 0 & -\frac{1}{2}A_{z-} & \omega_1 & -\Omega - \omega_{0I} + A_{zz} \end{pmatrix} + \Gamma \tag{3.14}$$

This arrangement of eigenstates is not in the typical order of descending energy, but is chosen to facilitate block diagonalization (red blocks).

Our aim is to determine the stationary density matrix $\rho(\infty)$ and the nuclear polarization $P_I(\infty)$,

$$P_I(t) = \frac{1}{I}\frac{\mathrm{Tr}\{\rho(t)I_z\}}{\mathrm{Tr}\{\rho(t)\}}. \tag{3.15}$$

We begin by deriving the stationary solution of $\mathcal{H}_{0S} + \mathcal{Z}_{0I} + A_{zz}S_zI_z$, and subsequently treat the $\mathcal{H}_{SI}$ as a small perturbation. In our prior study [96], where relaxation effects were neglected, we transformed to the tilted rotating frame characterized by the eigenstates of both the electron Zeeman and microwave interactions. In our current analysis, we incorporate an additional contribution from relaxation denoted by Γ. Recalling that the Bloch equations [30] describe the stationary solution of a spin 1/2 system with relaxation, where the Hamiltonian is $\mathcal{H}_{0S} = \hbar[\Omega S_z + \omega_1 S_x + \Gamma]$ with a matrix representation

$$\frac{\hbar}{2}\begin{pmatrix} \Omega & \omega_1 \\ \omega_1 & \Omega \end{pmatrix} + \Gamma. \tag{3.16}$$

The steady state solutions of the Bloch equation are

$$\begin{aligned} P_x &= P_0\frac{\Omega\omega_1 T_{2e}^2}{1 + (\Omega T_{2e})^2 + \omega_1^2 T_{1e}T_{2e}} \\ P_y &= P_0\frac{\omega_1 T_{2e}}{1 + (\Omega T_{2e})^2 + \omega_1^2 T_{1e}T_{2e}} \\ P_z &= P_0\frac{1 + (\Omega T_{2e})^2}{1 + (\Omega T_{2e})^2 + \omega_1^2 T_{1e}T_{2e}}. \end{aligned} \tag{3.17}$$

Here, P_0 represents the Boltzmann electron polarization, while $P_{x,y,z}$ denotes the steady state electron polarization along the x, y, z axes. T_{1e} and T_{2e} correspond to the electron relaxation times.

Hence, we introduce a new tilted frame with $\tilde{z} \parallel \vec{P}(\infty)$, illustrated in Figure 3.11. The selection of this tilted frame ensures that the density matrix $\rho(\infty)$ becomes diagonal. In

accordance with the Liouville equation, the steady state density matrix must commute with the Hamiltonian, i.e. $[\mathcal{H}_{0S}, \rho(\infty)] = 0$. Consequently, in this chosen frame, the Hamiltonian $\mathcal{H}_{0S}$ is diagonal, and the steady state of the system corresponds to the eigenstates of the system.

Comparing (3.14) and (3.16), we obtain two sets of psuedo-magnetizations P_x^+, P_y^+, P_z^+ and P_x^-, P_y^-, P_z^- for the upper $(\Omega + A_{zz})$ and lower $(\Omega - A_{zz})$ diagonal 2×2 sub-matrices, which are treated as two fictitious 1/2 spins (12 and 34),

$$\begin{aligned} P_x^{\pm} &= P_0 \frac{(\Omega \pm A_{zz})\omega_1 T_{2e}^2}{1 + ((\Omega \pm A_{zz})T_{2e})^2 + \omega_1^2 T_{1e} T_{2e}} \\ P_y^{\pm} &= P_0 \frac{\omega_1 T_{2e}}{1 + ((\Omega \pm A_{zz})T_{2e})^2 + \omega_1^2 T_{1e} T_{2e}} \\ P_z^{\pm} &= P_0 \frac{1 + ((\Omega \pm A_{zz})T_{2e})^2}{1 + ((\Omega \pm A_{zz})T_{2e})^2 + \omega_1^2 T_{1e} T_{2e}}. \end{aligned} \tag{3.18}$$

In order to block diagonalize the Hamiltonian $\mathcal{H}$, we can define tilted frames for the two fictitious 1/2 spins (the diagonal 2×2 sub-matrices, see (3.14)) as $\tilde{z}_{\pm} \parallel \vec{P}^{\pm}$. Using the argument $[\mathcal{H}_{0S}, \rho(\infty)] = 0$, in this frame $\mathcal{H}_{0S} + \mathcal{Z}_{0I} + A_{zz} S_z I_z + \Gamma$ is diagonal. This is equivalent to a rotation about $S_x \cos\phi_{\pm} + S_y \sin\phi_{\pm}$ by an angle $\theta_{\pm}$, where $\phi_{\pm}$ and $\theta_{\pm}$ are Euler angles illustrated in Figure 3.11, thus

$$\tan\phi_{\pm} = -\frac{P_x^{\pm}}{P_y^{\pm}}, \tag{3.19}$$

and

$$\sin\theta_{\pm} = \frac{\sqrt{(P_x^{\pm})^2 + (P_y^{\pm 2})}}{\sqrt{(P_x^{\pm})^2 + (P_y^{\pm})^2 + (P_z^{\pm})^2}}. \tag{3.20}$$

Therefore, the actual operators to transform the 2×2 sub-matrices can be written

$$\begin{aligned} u_{\pm} &= e^{i\theta_{\pm}(S_x \cos\phi_{\pm} + S_y \sin\phi_{\pm})} \\ &= \begin{pmatrix} \cos\frac{\theta_{\pm}}{2} & -\sin\frac{\theta_{\pm}}{2} e^{-i(\phi_{\pm} + \frac{\pi}{2})} \\ \sin\frac{\theta_{\pm}}{2} e^{i(\phi_{\pm} + \frac{\pi}{2})} & \cos\frac{\theta_{\pm}}{2} \end{pmatrix}, \end{aligned} \tag{3.21}$$

where we inserted the matrix representation of S_x and S_y. We can calculate the transformed off-diagonal sub-matrices $\mathcal{H}_{\pm\mp}$ (blue blocks in (3.14)), representing the H_{SI} term that is treated as a small perturbation. Using $\mathcal{H}_{+-}$ as an example, it becomes

$$\begin{aligned} u_+ \mathcal{H}_{+-} u_-^{\dagger} &= u_+ \begin{pmatrix} \frac{1}{2}A_{z+} & 0 \\ 0 & -\frac{1}{2}A_{z+} \end{pmatrix} u_-^{\dagger} \\ &= \begin{pmatrix} \frac{1}{2}A_{z+}\cos\theta & -\frac{1}{2}A_{z+}\sin\theta \\ -\frac{1}{2}A_{z+}\sin\theta & -\frac{1}{2}A_{z+}\cos\theta \end{pmatrix}. \end{aligned} \tag{3.22}$$

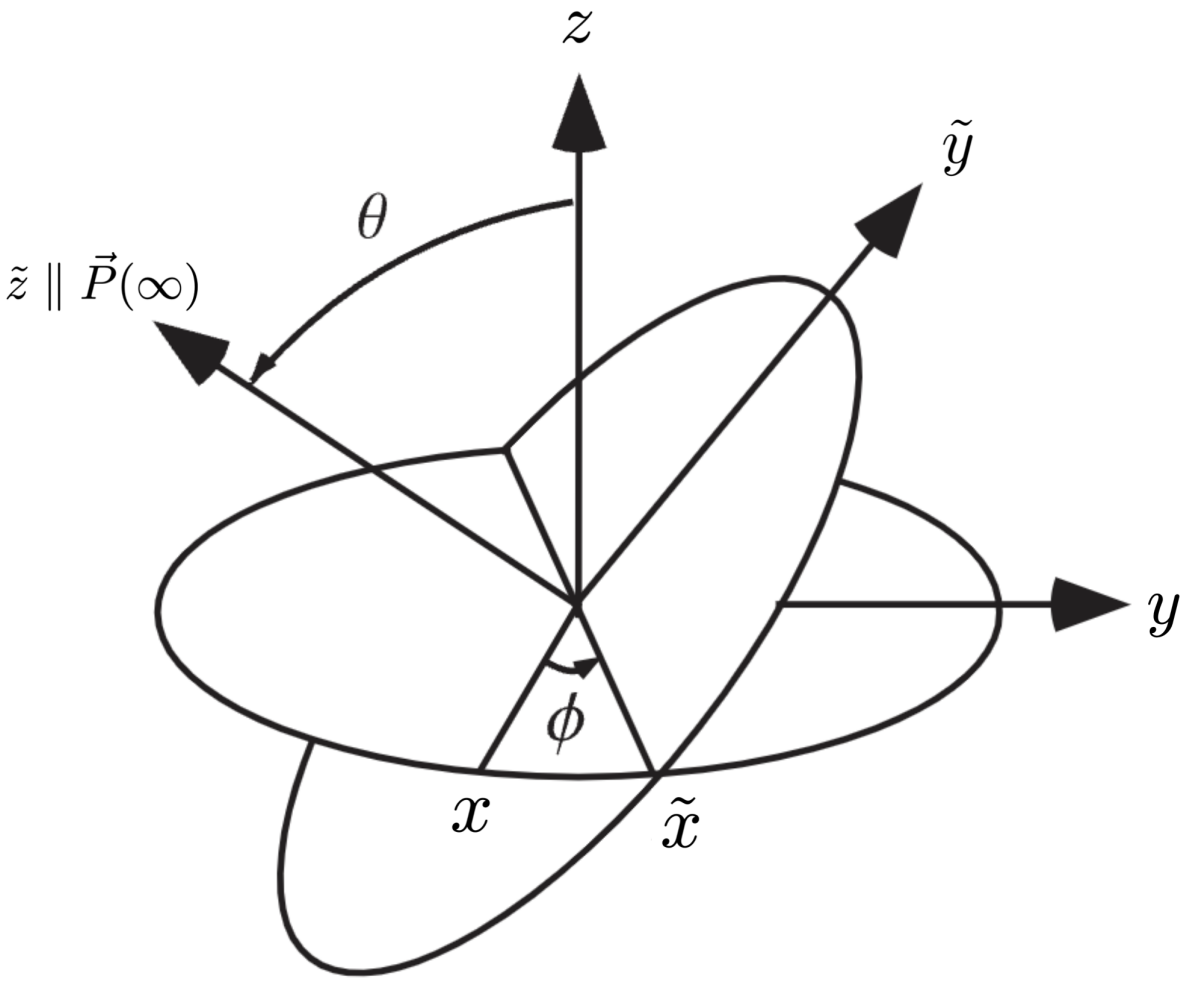

Figure 3.11: Defining a new frame where $\tilde{z} \parallel \vec{P}(\infty)$.

and $\mathcal{H}_{-+}$ is the complex conjugate. Here

$$\begin{aligned}
\sin\theta &= \cos\frac{\theta_+}{2}\sin\frac{\theta_-}{2}e^{-i(\frac{\pi}{2}+\phi_-)} + \sin\frac{\theta_+}{2}\cos\frac{\theta_-}{2}e^{-i(\frac{\pi}{2}+\phi_+)} \\
&= (\frac{\sin\phi_+ + \sin\phi_-}{2}\sin\frac{\theta_+ + \theta_-}{2} \\
&\quad + \frac{\sin\phi_+ - \sin\phi_-}{2}\sin\frac{\theta_+ - \theta_-}{2}) \\
&\quad + i(\frac{\cos\phi_+ + \cos\phi_-}{2}\sin\frac{\theta_+ + \theta_-}{2} \\
&\quad + \frac{\cos\phi_+ - \cos\phi_-}{2}\sin\frac{\theta_+ - \theta_-}{2})
\end{aligned} \tag{3.23}$$

is a complex number (also for $\cos\theta$), but only the absolute values $|A_{z+}|$ and $|\sin\theta|$ is of significance. The expression is structured in this manner for simplicity. It is easy to show

that

$$
\begin{aligned}
|\sin\theta|^2 =& \frac{1}{2}[(\sin^2\frac{\theta_+ + \theta_-}{2} + \sin^2\frac{\theta_+ - \theta_-}{2}) \\
&+ (\sin^2\frac{\theta_+ + \theta_-}{2} - \sin^2\frac{\theta_+ - \theta_-}{2}) \\
&\cos(\phi_+ - \phi_-)] \\
=& \sin^2\frac{\theta_+ + \theta_-}{2}\cos^2\frac{\phi_+ - \phi_-}{2} \\
&+ \sin^2\frac{\theta_+ - \theta_-}{2}\sin^2\frac{\phi_+ - \phi_-}{2}
\end{aligned}
\tag{3.24}
$$

Given that $u_\pm$ is unitary, the product $u_+\mathcal{H}_{+-}u_-^\dagger$ is expected to exhibit a form of $\frac{1}{2}A_{z+}$ multiplied by a unitary matrix. If we neglect A_{zz}, a common approximation as seen in references [39, 49, 128], we have $\phi_+ = \phi_-$ and $\theta_+ = \theta_-$. Consequently, based on (3.23), we find that $\sin\theta = \sin\theta_+ e^{i\phi_+} = \sin\theta_- e^{i\phi_-}$ and $|\sin\theta| = |\sin\theta_+| = |\sin\theta_-|$.

The stationary density matrix for $\mathcal{H}_{0S} + A_{zz}S_zI_z + \mathcal{Z}_{0I}$ in this chosen frame can be expressed as

$$
\begin{pmatrix}
\frac{1+P_+}{4} & 0 & 0 & 0 \\
0 & \frac{1-P_+}{4} & 0 & 0 \\
0 & 0 & \frac{1+P_-}{4} & 0 \\
0 & 0 & 0 & \frac{1-P_-}{4}
\end{pmatrix},
\tag{3.25}
$$

where $P_\pm = \sqrt{(P_x^\pm)^2 + (P_y^\pm)^2 + (P_z^\pm)^2}$. The electron polarization is

$$
P_e = \frac{P_+ + P_-}{2}.
\tag{3.26}
$$

Therefore, in this tilted frame of reference in the basis of eigenstates, $|m_{\tilde{S}}, m_I\rangle = |+\frac{1}{2}, -\frac{1}{2}\rangle$, $|-\frac{1}{2}, -\frac{1}{2}\rangle$, $|+\frac{1}{2}, +\frac{1}{2}\rangle$, $|-\frac{1}{2}, +\frac{1}{2}\rangle$, the matrix representation of the Hamiltonian becomes

$$
\frac{\hbar}{2}\begin{pmatrix}
\Omega_+ + \omega_{0I} & 0 & \frac{1}{2}A_{z+}\cos\theta & -\frac{1}{2}A_{z-}\sin\theta \\
0 & -\Omega_+ + \omega_{0I} & -\frac{1}{2}A_{z-}\sin\theta & -\frac{1}{2}A_{z+}\cos\theta \\
\frac{1}{2}A_{z-}\cos\theta & -\frac{1}{2}A_{z+}\sin\theta & \Omega_- - \omega_{0I} & 0 \\
-\frac{1}{2}A_{z+}\sin\theta & -\frac{1}{2}A_{z-}\cos\theta & 0 & -\Omega_- - \omega_{0I}
\end{pmatrix},
\tag{3.27}
$$

where $\Omega_\pm = \Omega/\cos\theta_\pm$.

As shown in the supporting information of [96] the terms $A_{z\pm}\cos\theta$ only weakly mix the nuclear spin states, which can be neglected.

Now we consider the two transitions (ZQ and DQ) which induce DNP. Taking ZQ as an illustrative example, we can define a fictitious spin $\frac{1}{2}$ denoted as J for the center 2×2 sub-matrix. The ZQ sub-matrix can be expressed as

$$
\begin{aligned}
\mathcal{H}_{\mathcal{ZQ}} &= \frac{\hbar}{2}\begin{pmatrix} (\Omega_+ - \omega_{0I}) & \frac{1}{2}A_{z-}\sin\theta \\ \frac{1}{2}A_{z+}\sin\theta & -(\Omega_- - \omega_{0I}) \end{pmatrix} \\
&= (\Omega' - \omega_{0I})J_z + \tfrac{1}{2}|A_{z-}\sin\theta|J_x + \frac{\Omega_+ - \Omega_-}{2}I,
\end{aligned}
\tag{3.28}
$$

using the operators J_{xyz} for the ZQ fictitious spin 1/2. Here $\Omega' = \frac{\Omega_+ + \Omega_-}{2}$ and I is the identity matrix. Notice that in this representation, we include an absolute value to $A_{z-}\sin\theta$ for the sake of simplicity, eliminating the imaginary part that is actually aligned with S_y. A more rigorous approach would involve an additional rotation about S_z. The last term of the Hamiltonian, which always commutes with the density matrix, can be discarded without modifying the system's evolution.

The initial polarization without the off-diagonal hyperfine term for the ZQ sub-matrix is given by

$$P^0_{ZQ} = \frac{1-P_-}{2} - \frac{1+P_+}{2} = -\frac{P_+ + P_-}{2} = -P_e. \tag{3.29}$$

Similarly, for the DQ sub-matrix, the initial electron polarization is $P^0_{DQ} = P_e$.

The Hamiltonian has exactly the structure of a microwave irradiation $\frac{1}{2}|A_{z-}|\sin\theta$ at an offset frequency $(\Omega' - \omega_{0I})$. We then introduce the T_1^* and T_2^* for both the ZQ and DQ transitions in this frame of electron eigenstates, and we can employ the Bloch equation (3.18) once more to compute the stationary nuclear polarization (note a negative sign as the nulcear Zeeman Hamiltonian is defined as $-\omega_{0I}I_z$),

$$\begin{aligned} P_I^{ZQ} &= P_e \times \\ &\frac{(\frac{1}{2}|A_{z-}|\sin\theta)^2 T^*_{1ZQ} T^*_{2ZQ}}{1 + (\Omega' - \omega_{0I})^2 {T^*_{2ZQ}}^2 + (\frac{1}{2}|A_{z-}|\sin\theta)^2 T^*_{1DQ} T^*_{2DQ}}. \end{aligned} \tag{3.30}$$

The nuclear polarization for the DQ fictitious spin 1/2 can be calculated using the same approach

$$\begin{aligned} P_I^{DQ} &= -P_e \times \\ &\frac{(\frac{1}{2}|A_{z-}|\sin\theta)^2 T^*_{1DQ} T^*_{2DQ}}{1 + (\Omega' + \omega_{0I})^2 {T^*_{2DQ}}^2 + (\frac{1}{2}|A_{z-}|\sin\theta)^2 T^*_{1DQ} T^*_{2DQ}} \end{aligned} \tag{3.31}$$

noticing the sign difference from the initial polarization. Therefore we obtain the final nuclear polarization

$$P_I = P_I^{ZQ} + P_I^{DQ}. \tag{3.32}$$

We define T^*_{1ZQ}, T^*_{1DQ}, T^*_{2ZQ} and T^*_{2DQ} as the T_1 and T_2 cross relaxation times for the ZQ and DQ transitions in the eigenstate frame of the electron Hamiltonian $\mathcal{H}_{0S}$ with microwave irradiation. The notation with the "$*$" signifies that these relaxation times are simply defined as the decay or dephasing of the elements in the density matrix in accordance with the Bloch equations.

For CW irradiation at high magnetic fields, the hyperfine coupling is much smaller than the nuclear Larmor frequency and ω_1 is small. In particular, when $\omega_1 T_{2e} \ll 1$, i.e. ω_1 weaker than the homogenous broadening, we find $P_x << P_z$ and $P_y << P_z$. In this case, the magnetization is still almost aligned along the P_z regardless of the microwave frequency. Thus, θ is small and the new frame of reference is almost the same as the rotating frame, leading to $\Omega' = \Omega$. Additionally, it becomes apparent that for the SE , our results coincide with the result derived by Hovav, et al. [11] (compare (3.30) and (3.31) above to (33) in [11]). Beyond the SE, our derivation also facilitates an understanding of the origin of the RM and OE, which was previously not recognized.

In practical samples, an electron is typically coupled to multiple nuclear spins. Moreover, the electron spin interacts with other electron spins, giving rise to T_{2e}, and the treatment for such an interacting spin system involves the Provotorov equations rather than the Bloch equations. Nevertheless, as we will see below, the calculations for this simple electron-nuclear system already offer valuable insights into understanding several experimental observations. Additionally, any comprehensive approach needs to account for the inhomogeneous broadening such as the g-anisotropy.

With the theory developed above, we can now analytically calculate the DNP Zeeman field profile using (3.32). Shown in Figure 3.12 are the DNP frequency/field profiles for different cross relaxation rates (for the specific parameters see the figure caption). In our analysis, we employ a Gaussian function with a standard deviation of 10 MHz to represent the inhomogeneous broadening. Immediately, the terms in the denominator $(1 + (\Omega' \pm \omega_{0I})^2)$ result in the SE peaks at $\omega_{0S} \pm \omega_{0I}$ and the RM/OE lineshape near the center of the EPR line at ω_{0S}. When $T^*_{1ZQ} = T^*_{1DQ}$, a dispersive shaped DNP Zeeman profile is observed near the EPR center, corresponding to RM. In cases where $T^*_{1ZQ} \neq T^*_{1DQ}$ and/or $T^*_{2ZQ} \neq T^*_{2DQ}$ an absorptive OE DNP profile is obtained, while the SE is less sensitive to these changes. Here, we present the case where $T_{1ZQ} > T_{1DQ}$, resulting in a negative OE. In the Supporting Information, we also discuss the scenario where $T_{1ZQ} > T_{1DQ}$ and the expected positive OE peak is observed. (should put an example of a positive OE enhancement in the text) With the theory developed above, we can now analytically calculate the DNP Zeeman field profile using (3.32). Shown in Figure 3.12 are the DNP frequency/field profiles for different cross relaxation rates (for the specific parameters see the figure caption). In our analysis, we employ a Gaussian function with a standard deviation of 10 MHz to represent the inhomogeneous broadening. Immediately, the terms in the denominator $(1 + (\Omega' \pm \omega_{0I})^2)$ result in the SE peaks at $\omega_{0S} \pm \omega_{0I}$ and the RM/OE lineshape near the center of the EPR line at ω_{0S}. When $T^*_{1ZQ} = T^*_{1DQ}$, a dispersive shaped DNP Zeeman profile is observed near the EPR center, corresponding to RM. In cases where $T^*_{1ZQ} \neq T^*_{1DQ}$ and/or $T^*_{2ZQ} \neq T^*_{2DQ}$ an absorptive OE DNP profile is obtained, while the SE is less sensitive to these changes. Here, we present the case where $T_{1ZQ} > T_{1DQ}$, resulting in a negative OE. In the Supporting Information, we also discuss the scenario where $T_{1ZQ} > T_{1DQ}$ and the expected positive OE peak is observed. It has been demonstrated that by selectively deuterating different proton sites on BDPA molecules, we can effectively tune the cross-relaxation times, which results in both positive and negative Overhauser effects (OE), as illustrated in Figure 3.13.

3.3.3 Numerical Simulation

As illustrated in Figure 3.14, we have conducted numerical simulations using the SpinEvolution software to demonstrate the DNP Zeeman field profiles under different conditions. More details about the simulation are provided in the supporting information. The simulation results qualitatively confirm our analytical calculation. In our simulations, we incorporated g-anisotropy and powder averaging. Moreover, the relaxation in the simulations is defined in the laboratory frame, whereas the analytical calculations are defined in the tilted frame using the eigenstates of the electron Hamiltonian under microwave irradiation. A distortion on the low frequency side of the RM/OE field profile is from the g-anisotropy of the trityl. Here, the simulation uses the g-value of trityl [126], and is compared to the simulation without

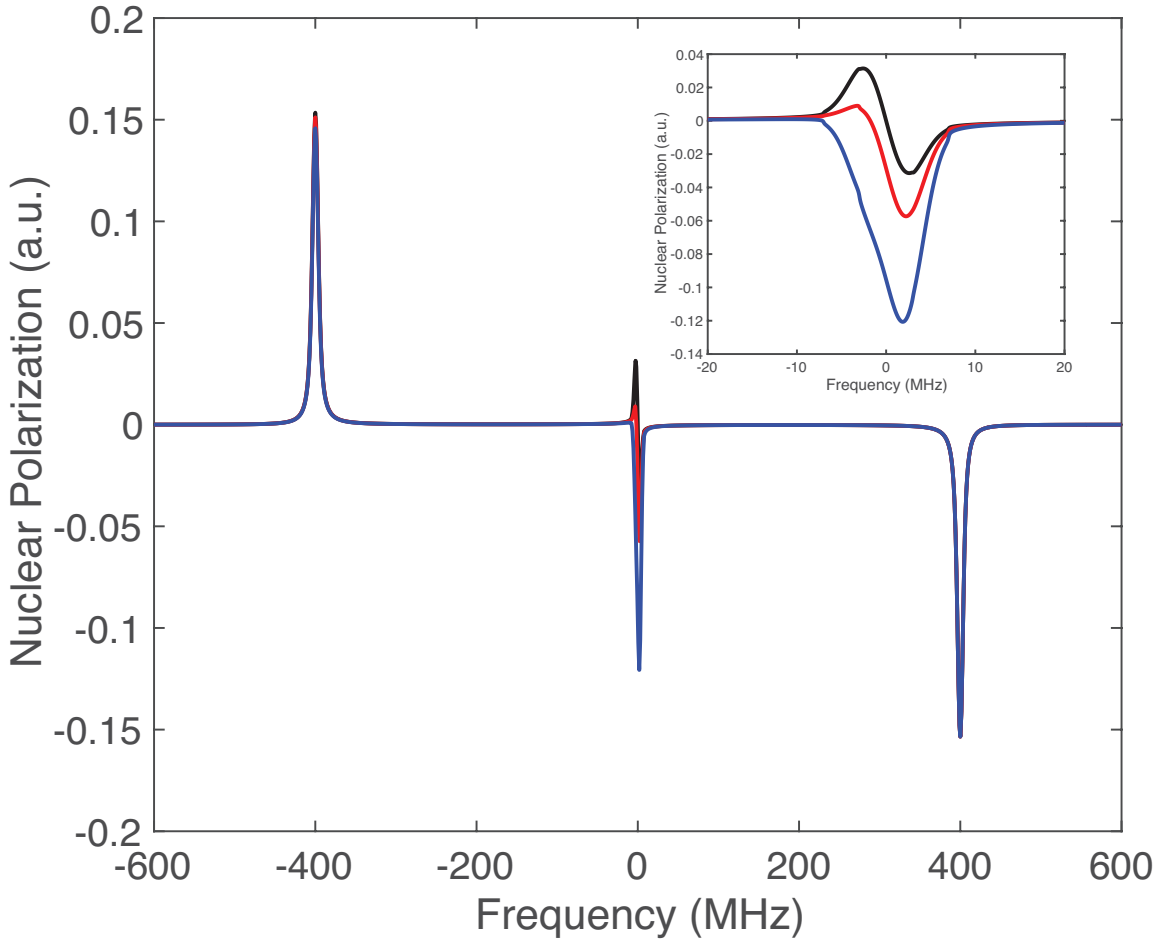

Figure 3.12: DNP Zeeman profiles calculated from (3.32) for $\omega_{0I}/2\pi = 400\,\text{MHz}$, $\omega_1/2\pi = 0.05\,\text{MHz}$, $A_{zz} = 2\,\text{MHz}$, $A_{z+} = 0.5\,\text{MHz}$, $T_{1e} = 1\,\text{ms}$, $T_{2e} = 2\mu\text{s}$, $T^*_{2ZQ} = T^*_{2DQ} = 50\,\text{ns}$ and $T^*_{1ZQ} = 1\,\text{ms}$ with $T^*_{1DQ} = 1$ (black), 0.985 (red) and 0.95 ms (blue). Inset is the expansion of the DNP Zeeman field profile near the electron resonance. A 10 MHz gaussian function is used to broaden the simulation.

g-anisotropy (see Figure S1 in the supporting information) which also removes this distortion. The blue trace shows a curve consisting of two peaks with structure for the center OE. The simulation can describe the DNP Zeeman field profile of trityl samples with different radical concentrations as discussed previously [124]. Furthermore, the center RM/OE peak is broader than the SE as well as the EPR line, which has also been observed experimentally [10, 96, 124]. This can be explained by the static solution of the Bloch equations: the dispersive EPR component (which also contributes to the electron saturation) is broader than the absorptive EPR component [131].

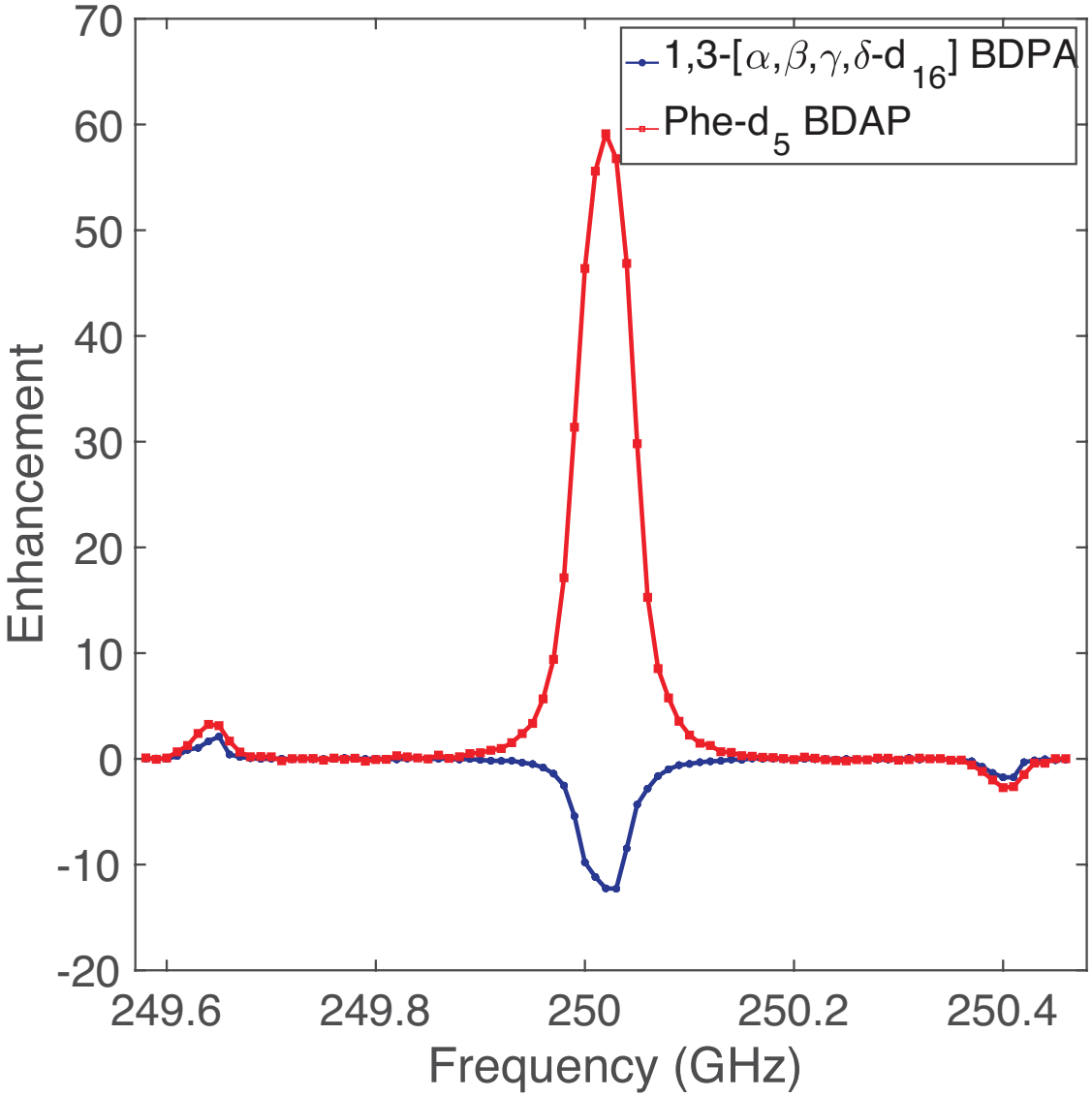

Figure 3.13: DNP Zeeman profiles of selectively deuterated BDPA (2.5 wt %) in 95/5 mol % d14- and h14-ortho-terphenyl, resulting in positive and negative OE. Figure taken from [59].

3.3.4 Experimental Results

DNP study We recorded a Zeeman field profile for 100 mM OX063-trityl in d_6-DMSO:D_2O:H_2O (6:3:1) at $\omega_{0I}/2\pi = 380\,\text{MHz}$, $\omega_r/2\pi = 6\,\text{kHz}$, at different temperatures (Figure 3.15). Microwave irradiation was provided by a 160 mW solid state source [125]. Our focus is primarily on the study near the EPR center, where RM and OE are prominent. The SE lines are outside of the frequency range of the sweep and are comparatively weak and below the threshold for detection in this experimental configuration. The figure includes the ratio between the positive and negative RM peaks. Notably, at a low temperature of 95 K, the DNP field profile exhibits a larger asymmetry than at 125 K. This observation suggests that at low temperatures, the ZQ and DQ cross relaxations are similar, whereas at higher temperatures, they began to

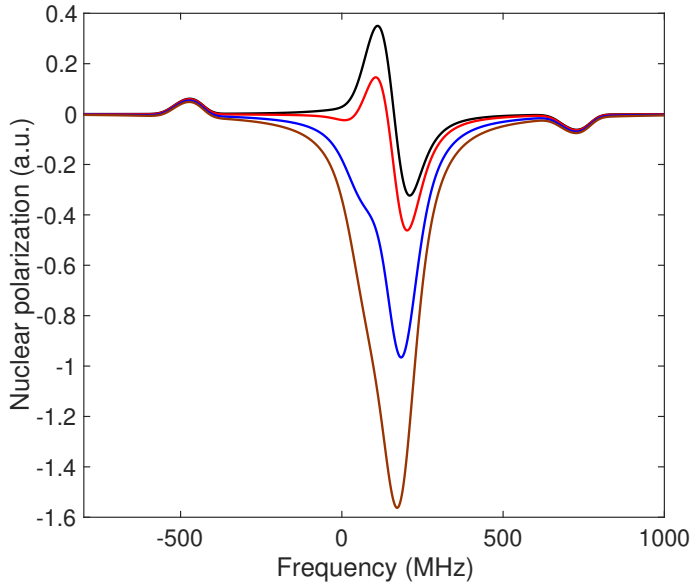

Figure 3.14: Simulated DNP field profiles of an electron-nuclear spin pair with the following parameters: $g = (2.0032, 2.0026, 2.0026)$, $\omega_{1S}/2\pi = 1.0\,\text{MHz}$, $T_{1e} = 1\,\text{ms}$, $T_{2e} = 0.2\,\mu\text{s}$, $T_{1ZQ} = 1\,\text{ms}$, $T_{1DQ} = 1\,\text{ms}$ (black), $0.999\,\text{ms}$ (red), $0.996\,\text{ms}$ (blue), $0.993\,\text{ms}$ (brown), $T_{2ZQ} = T_{2DQ} = 0.2\,\mu\text{s}$.

differ. As proposed in [132], the observed OE in nonconducting solids, which represents the difference between ZQ and DQ cross-relaxations, may be attributed to the molecular motion from methyl groups not frozen out at low temperatures. If the temperature is even lower, then the molecular motion may be quenched leading to a RM DNP Zeeman profile for trityl. In contrast to BDPA, trityl lacks strongly hyperfine-coupled protons, possibly contributing to its more dispersive DNP field profile. Additionally, [125] suggests that modifying the trityl radical can induce a different OE DNP field profile.

Moreover, the proton DNP field profile was measured for a 80 mM OX063-trityl sample in the same glassing matrix sample in a 211 MHz spectrometer using a 4 mm rotor at $\omega_r/2\pi = 5\,\text{kHz}$. A solid-state source provided approximately 20 mW of microwave power at 140 GHz to polarize the nuclear spins. Figure 3.16 depicts the field profiles measured at various temperatures, where the ratio between the positive and negative RM peaks are included. The results confirm the experimental findings at 380 MHz, indicating that the center structure becomes less asymmetric at higher temperatures. This suggests a larger difference in cross-relaxation at elevated temperatures, potentially related to molecular motion [132].

Furthermore, we performed the same DNP field profile measurement with a 80 mM OX071-trityl (fully deuterated OX063-trityl) in the same glassing matrix at 90 K. This is shown in the supporting information. The ratio between the positive and negative RM peaks is larger than the protonated trityl, suggesting the proton on the polarizing agent plays a role in the cross relaxation similar to that found in BDPA/oTP samples [59, 93].

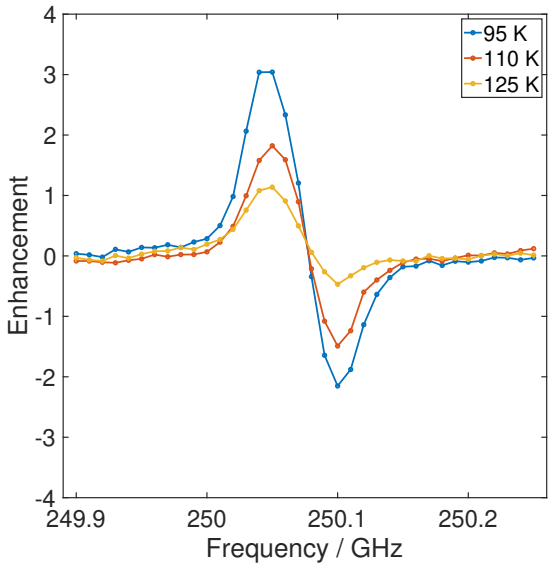

Figure 3.15: DNP field profile for a 100 mM OX063-trityl in d_6-DMSO:D_2O:H_2O (6:3:1) sample at $\omega_{0I}/2\pi = 380\,\text{MHz}$ and different temperatures with $\omega_r/2\pi = 6$ kHz, irradiated by a 160 mW solid state source.

EPR study of Trityl at 395 GHz To gain deeper insights into DNP using trityl as the PA at high magnetic fields, echo-detected EPR spectra were recorded with a 260 (or 263 ?) GHz EPR spectrometer at 80 K. The measurements were conducted for 10 and 100 mM samples in d_6-DMSO:D_2O:H_2O (6:3:1) and d_8-glycerol:D_2O:H_2O (6:3:1), as illustrated in Figure 3.17. For all the samples, the line widths are consistently well below 100 G, i.e. 280 MHz, and notably below the proton NMR frequency 400 MHz (???). In both the glycerol and DMSO matrices, the dominant factor contributing to the EPR line width arises from the g-anisotropy. The broadening effect induced by electron-electron dipolar coupling, resulting from a higher trityl concentration (comparison between 10 mM and 100 mM), is minimal in comparison to the g-anisotropy. This observation is consistent with our calculations, where we estimated that the increase in trityl concentration from 10 mM to 100 mM would result in a 10 MHz contribution to the EPR line width due to electron-electron dipolar coupling [96]. It is intriguing that the line EPR line width of trityl is generally narrower in d_6-DMSO:D_2O:H_2O (6:3:1) than d_8-glycerol:D_2O:H_2O (6:3:1). The broader EPR line width observed in d_8-glycerol:D_2O:H_2O (6:3:1) would intuitively imply that the thermal mixing DNP process should be more easily achievable in this matrix, while the experimental results in [124] suggests otherwise. However, this can be easily explained by RM/OE. We propose that this difference can be attributed to the different solvation configurations of the trityl molecule within each matrix, which leads to variations in the g-anisotropy. This structural difference may, in turn, influence the cross-relaxation mechanisms between the electron and nuclear spins, providing a plausible explanation for the slightly different different DNP behavior of trityl observed in the two matrices, as discussed elsewhere [59].

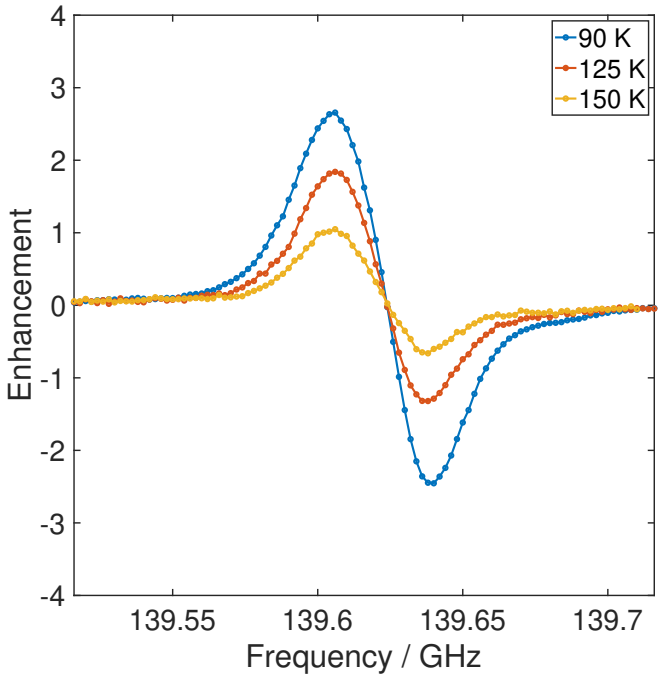

Figure 3.16: DNP field profiles of a 80 mM Trityl in DMSO-d6, D_2O and H_2O (60:30:10) matrix sample at 140 GHz/211 MHz spinning at 5 kHz at 90, 125 and 150 K.

Trityl DNP at 600 MHz with Gd^{3+} doping High-spin transition-metal complexes, such as Gd^{3+} and Mn^{2+}, are also used as polarizing agents [133–137]. They are particularly relevant for inorganic samples and metalloproteins that either naturally contain or can be doped with paramagnetic metal ions. Gd^{3+} is of particular interest due to its narrow central transition, which exhibits promising DNP enhancements at high magnetic fields. Moreover, studies have demonstrated that doping Gd^{3+} into a trityl sample can enhance the ^{13}C DNP performance [138, 139]. This can lead to an increase of ^{13}C polarization and a decrease in DNP buildup time as the presence of Gd^{3+} reduces the trityl electron T_1, facilitating faster recovery of electron polarization and resulting in larger enhancements.

The experimental ^1H DNP field profiles of $\sim$ 80 mM trityl-OX063 dissolved in a mixture of d_6-DMSO:D_2O:H_2O (6:3:1) are recorded at a magnetic field of $\omega_{0I}/2\pi = 600$ MHz. The influence of different Gd^{3+}-DOTA doping concentrations on the DNP field profile was investigated and depicted in Figure 3.18. The samples were prepared by adding 20 mM Gd^{3+} in d_6-DMSO:D_2O:H_2O (6:3:1) solution into the same trityl sample. This is because it is difficult to precisely weigh a small mount of Gd^{3+}-DOTA for doping. Consequently, the precise radical concentrations in the three samples were as follows: (1) 80 mM trityl, 0 mM Gd^{3+}; (2) 76 mM trityl, 1 mM Gd^{3+}; and (3) 72 mM trityl, 2 mM Gd^{3+}. The sample was spun at $\omega_r/2\pi = 8$ kHz, the sample temperature maintained at 95 K, and microwave irradiation provided by a 17 W gyrotron microwave source.

In the absence of Gd^{3+} doping, we observe the characteristic dispersive Resonant Mixing (RM) field profile near the EPR center which has been previously reported [96]. Upon

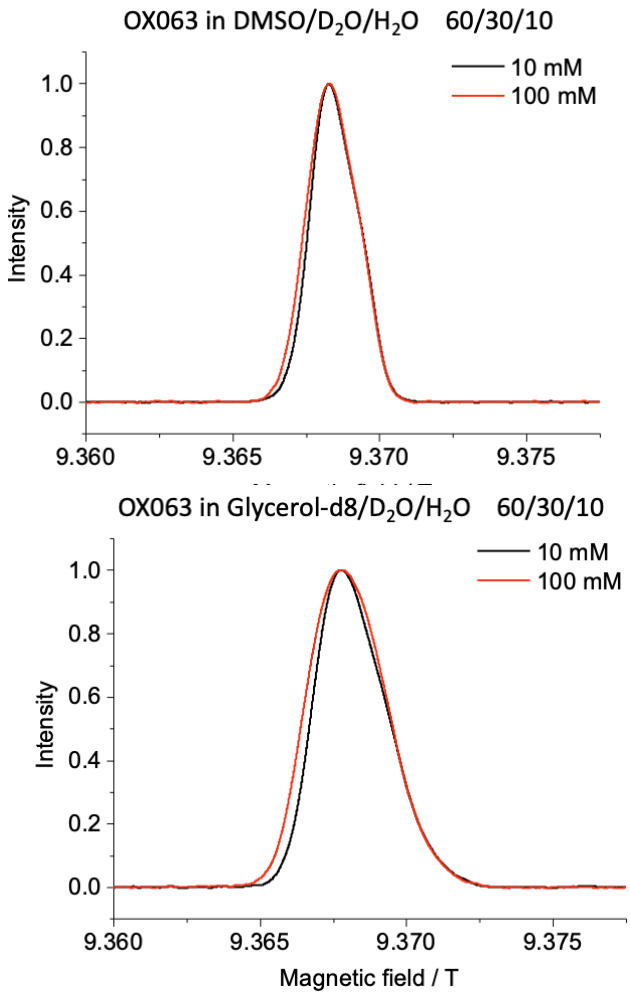

Figure 3.17: 260 GHz echo detected EPR for 10 and 100 mM trityl-OX063 samples in d_6-DMSO:D_2O:H_2O (6:3:1) and d_8-glycerol:D_2O:H_2O (6:3:1) matrices.

introducing 1 mm Gd^{3+}, dispersive field becomes asymmetric and partially transitions to a negative absorptive OE DNP profile. Interestingly, it behaves completely differently from the Gd^{3+3+} doping effect for ^{13}C DNP [138, 139], where improvements of both positive and negative DNP enhancements were observed.

The experimental findings again suggest that RM and OE DNP are related, and align with our theoretical interpretation. When the ZQ and DQ cross-relaxation rates are equal, an asymmetric dispersive RM DNP field profile is expected, whereas a difference between the two cross-relaxation rates leads to an absorptive profile, characteristic of Overhauser DNP. In the case of a small difference between the ZQ and DQ cross-relaxation rates, a asymmetric "absorptive" DNP field profile is obtained. This is also shown in the supporting information. We have fitted the 0 mM and 1 mM Gd^{3+3+} data using SpinEvolution [35] simulations based on a simple electron-nuclear spin pair system, as shown in Figure S5. The 2 mM Gd^{3+} field profile provides a stronger “OE” effect. These results suggest that Gd^{3+3+} reduces the ZQ cross-relaxation rate more significantly than the DQ cross-relaxation rate.

Furthermore, we show that by doping Gd^{3+} into the trityl system, we also improve the ^1H DNP performance by a factor of 2. From simulation we understand that only a small difference between the ZQ and DQ cross-relaxations can lead to a significant DNP enhancement (see S1 and S5), supporting that OE can be highly efficient at high magnetic fields. Gd^{3+} doping provides an approach to tailor the cross-relaxation mechanism and can be a potential tool to improve the effect.

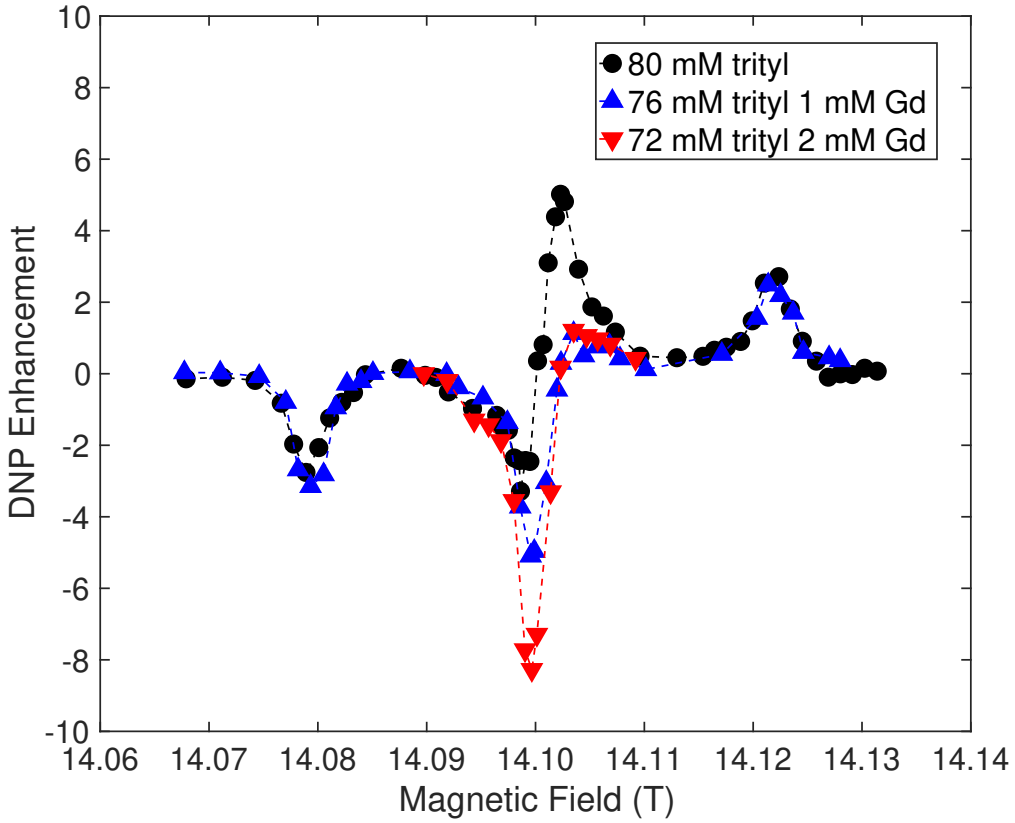

Figure 3.18: DNP field profiles of trityl samples in d_6-DMSO:D_2O:H_2O (6:3:1) matrix sample with different Gd^{3+}-DOTA doping concentration at 600 MHz spinning at 6 kHz at 95 K.

We have also recorded Zeeman field profiles for an 80 mM trityl-OX063 sample in d_6-DMSO:D_2O:H_2O (6:3:1) with Gd^{3+}-DOTA doping concentrations of 4 and 10 mM at $\omega_{0I}/2\pi = 380$ MHz, $\omega_r/2\pi = 6$ kHz, and T = 95 K, shown in Figure 3.19. Microwave irradiation was provided by a 160 mW solid-state source [125]. Note that the sample preparation for this measurement differed from the 600 MHz experiments, as Gd^{3+}-DOTA powder was directly added during sample preparation. The trityl DNP field profile without Gd^{3+} doping can be found in a previous publication [124]. With the introduction of Gd^{3+} into the trityl system, the RM field profile transitions to a non-symmetric dispersive profile and eventually completely transforms into a negative Overhauser Effect (OE) profile, as seen in Figure 3.14. This behavior is similar to the observations in the 600 MHz data. The experimental results suggest a continuous increase in the difference between the ZQ and DQ cross-relaxation rates with the addition of Gd^{3+}. The introduction of Gd^{3+} leads to a twofold improvement in

the enhancement factor. Additionally, experimental data from another trityl sample doped with 2 mM Gd^{3+} is presented in the supporting information. This sample exhibits direct OE behavior. It indicates that the sample preparation can influence the DNP performance to some extent. However, the measurements conducted at both 600 and 380 MHz consistently demonstrate that Gd^{3+} doping can initiate a transition from the RM to the OE by changing the relaxation parameters.

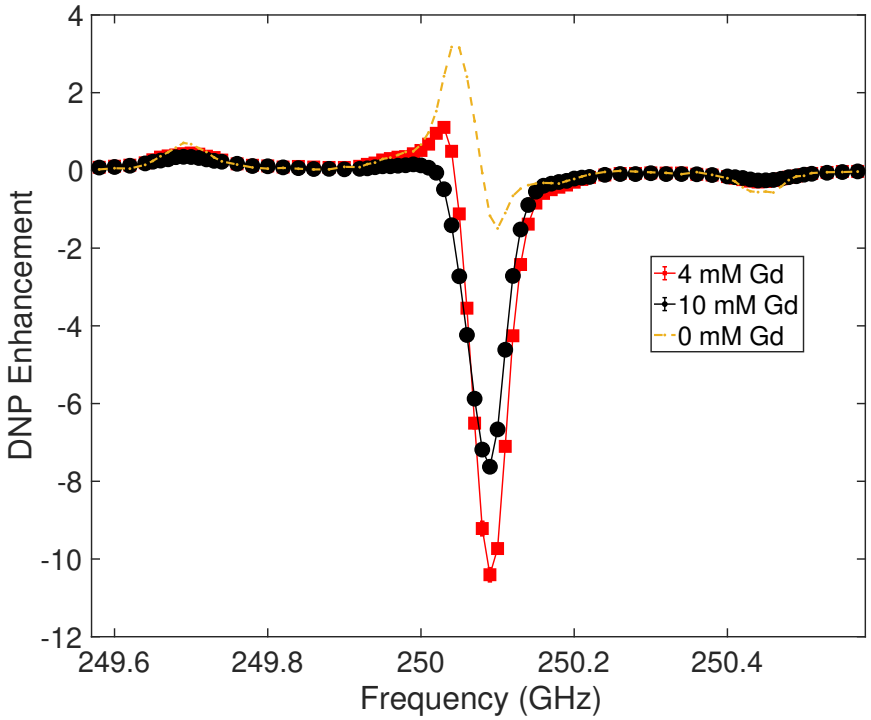

Figure 3.19: DNP field profiles of an 80 mM trityl sample in d_6-DMSO:D_2O:H_2O (6:3:1) matrix with different Gd^{3+}-DOTA doping at 250 GHz/380 MHz spinning at 6 kHz at 95 K. Dashed yellow line is taken from [124].

Furthermore, we would note that at 600 MHz (395 GHz for electrons), the trityl EPR and the Gd^{3+} central transitions are separated by 395 GHz $\times$ $(2.003 - 1.991)/2.003 \sim 2.4$ GHz. This separation, while substantial, does not exclude the potential occurrence of a truncated cross effect [140], involving interactions between the trityl and Gd^{3+} species. Conducting experiments at NMR frequencies exceeding 1 GHz NMR frequency would allow a more complete truncation of the cross effect. However, we remark that Gd^{3+} doping can improve thermal mixing DNP for both positive and negative enhancements [138, 139], suggesting that Gd^{3+} plays a more important role on the relaxation than simply introducing a cross effect. Moreover, we anticipate that the truncated cross effect will exhibit greater efficacy with increased Gd^{3+} concentration. The disappearance of the positive shoulder when employing 10 mM Gd^{3+} at 380 MHz, in contrast to the 4 mM condition (as depicted in Figure 3.19), requires a stronger truncated cross effect. Nevertheless, it should be noted that using 10 mM Gd^{3+} results in a diminished negative enhancement, indicating a change in relaxation rates, which can also induce the transition from RM to OE as we discussed. We also cannot exclude

the possibility of a collaborative effect of multiple mechanisms, which requires further spin dynamics studies.

The EPR spectra of the trityl samples doped with and without Gd^{3+} were recorded at 80 K using a Q-band EPR spectrometer, and the results are presented in Figure 3.20 and supporting information. Both the trityl and Gd^{3+} lines are observed in the spectrum. Two shoulders were observed for the trityl line, which we believe is the forbidden transitions (at solid effect conditions). It should be noted that at this low magnetic field, the dominant feature in the spectrum arises from the zero field splitting (ZFS) of Gd^{3+}. The pure Gd^{3+} EPR spectrum is provided in the supporting information. The T_1 and T_2 relaxation times of both the trityl and Gd^{3+} electrons were measured and are summarized in Table S1 in the supporting information. We observed that the T_2 of the trityl radical is minimally affected by Gd^{3+} doping. The slight change of the T_2 can likely be attributed to the dilution effect resulting from the addition of Gd^{3+}-DOTA solution. However, as shown in Figure 5 3.20, the saturation recovery curve of the trityl electron clearly indicates that the T_1 of the trityl electron is reduced by a factor of 2 with 1 mM Gd^{3+} doping and further decreases with 2 mM Gd^{3+}. This effect has been previously reported [138, 139] and is explained by the dipolar interaction between the trityl radical and the fast relaxing Gd^{3+}.

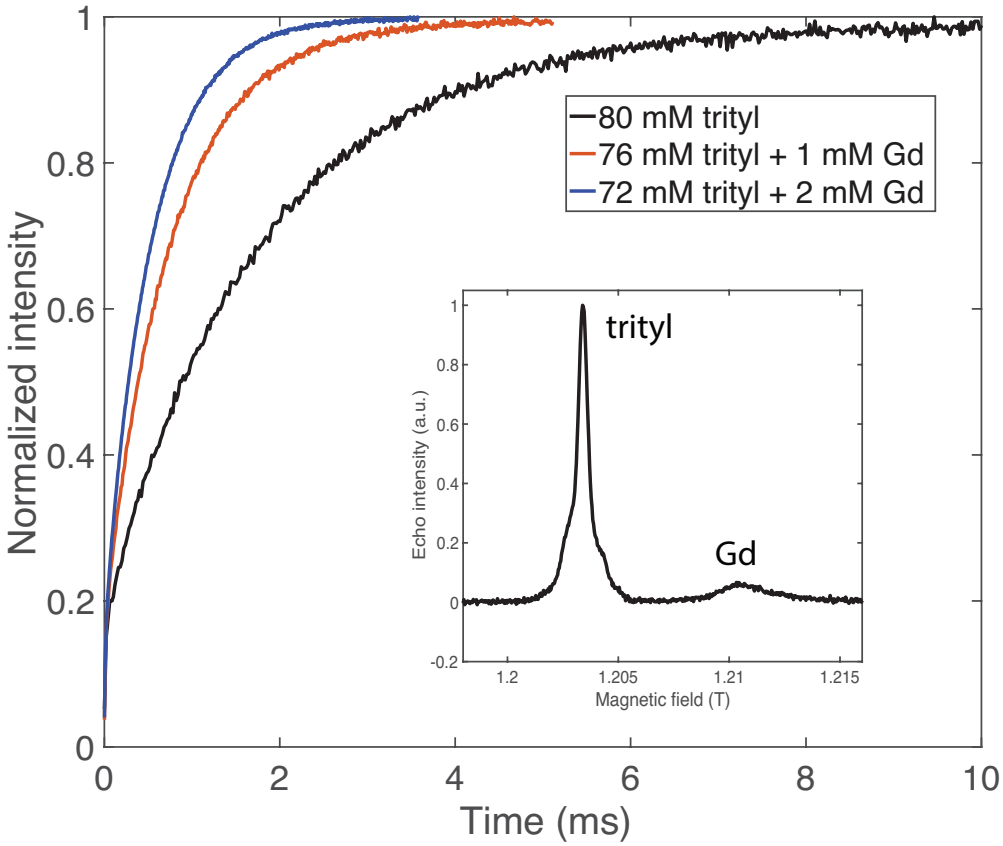

Figure 3.20: Saturation recovery measurement of the trityl electron at Q-band, 80 K with different Gd^{3+} doping concentration. The inset shows a Q-band EPR spectrum of a 72 mM trityl in d_6-DMSO:D_2O:H_2O (6:3:1) matrix sample with 2 mM Gd^{3+}-DOTA doping at 80 K.

3.4 Summary and Discussions

In summary, for the case of insulating solids subject to CW microwave irradiation, we propose a theory based on the Bloch and Solomon equations to explain the Overhauser effect (OE), resonant mixing (RM) DNP, and the solid effect (SE) as well. Our analysis reveals that the SE, OE and RM DNP processes can all be described analytically by a unified equation (3.32). This may explain the DNP field profile near the EPR line of the narrow line radicals, the absorptive shape for BDPA and the dispersive profile for trityl. Specifically, we propose the following theoretical understanding that can explain the experimental observations: a dispersive RM DNP field profile is observed when the ZQ and DQ cross-relaxations are equal, whereas a positive or negative absorptive OE field profile can be detected when they differ. This provides a theoretical basis for interpreting the trityl and BDPA experimental data. Our theory suggests that the observed center enhancement, whether absorptive OE or dispersive RM, is most pronounced at high magnetic fields with weak CW microwave irradiation. Furthermore, it implies that this enhancement can surpass the solid effect under these conditions as observed experimentally. Furthermore, the DNP enhancement profile is sensitive to the differences in cross-relaxation rates, making the OE potentially promising at high magnetic fields. This insight enhances our understanding of these DNP mechanisms and serves as a guide in optimizing the efficiency of DNP processes at high fields.

Experimentally, we show that the RM can transition to an OE when changing the temperature and Gd^{3+} doping. The 260 GHz EPR study reveals that the EPR line width remains well below the nuclear Larmor frequency, with the g-anisotropy continuing to dominate the EPR line, even for 100 mM trityl. Additionally, variations in the g-anisotropy for trityl in different glassing matrices suggest distinct molecular folding. This has already been exemplified through selective deuteration of BDPA [59, 93], and we expect further advances. Notably, at a frequency of 600 MHz, we demonstrate a twofold improvement in the enhancement with 2mM Gd^{3+} doping. Importantly, our experimental results elucidate that Gd^{3+} can at least preferably enhance the DQ cross-relaxation time compared to the ZQ cross-relaxation, thereby resulting in a negative enhancement of OE DNP. However, the understanding of RM and OE in insulating solids is still limited and we expect further advances, which should also help improve the DNP performance.

The impact of Gd^{3+} extends beyond RM utilizing trityl radicals and holds relevance for OE that has been observed in BDPA and other radical systems [59, 93]. Additionally, the ability of Gd^{3+} to reduce the T_1 of trityl radicals presents potential benefits for SE and TM (as demonstrated in [138, 139]) and pulsed DNP [40–45, 47–50, 55, 128, 141]. In the case of pulsed DNP, a repetition delay on the order of electron T_1 is required to recover the electron polarization. Thus, a long T_{1e} can lead to a long repetition delay and a reduction in polarization transfer rate. This issue becomes particularly pertinent at low temperatures. The findings from our EPR study indicate that Gd^{3+} doping has the potential to address this concern, particularly due to its negligible effect on the electron spin coherence time, T_2. This aspect requires further exploration in future investigations. Doping transition metals has demonstrated promising outcomes in enhancing various DNP mechanisms. While Gd^{3+} has exhibited positive results, it is also important to explore the potential contributions of other transition metals as well.

While our current analysis focused on the simple case of a coupled electron-nuclear spin pair, practical DNP involves interacting spin systems with coupled electrons. Addressing such complex scenarios requires accurate treatments, which will be explored in the future through the examination of the Provotorov equations rather than the simpler Bloch equations. This expansion of our theoretical framework aims to obtain a more comprehensive understanding of DNP in practical applications.

Concluding Remarks

The three studies presented in this chapter reveal that dynamic nuclear polarization mechanisms often regarded as distinct—such as the Overhauser effect and the newly introduced resonant mixing—may, in fact, reflect different manifestations of a common underlying principle: polarization transfer mediated by fluctuating hyperfine interactions in the presence of weak microwave irradiation. While the classical Overhauser effect has traditionally been associated with liquids or metals, our observations in insulating solids show that similar enhancements can arise when specific relaxation pathways are enabled or engineered. Meanwhile, a polarization mechanism that seem to be responsible for spin dynamics may not be the actual pathway. The RM mechanism illustrates how coherent state mixing in a detuned two-spin system can reproduce enhancement profiles typically attributed to thermal mixing or SE.

A central conclusion of this body of work is that *relaxation is not a nuisance but an asset*. By explicitly including electron and cross-relaxation terms, we recover field profiles and polarization dynamics that are otherwise inexplicable by coherent models alone. Furthermore, our results show that even subtle modifications to the spin environment—such as selective deuteration, Gd doping, or tuning microwave detuning—can dramatically affect DNP efficiency. These observations suggest that the apparent diversity of DNP mechanisms may stem less from fundamentally different physics than from the experimental regimes in which particular terms dominate.

Finally, my contribution lies in clarifying these connections across theory and doing specific experiments. By synthesizing deuterated radicals, engineering relaxation rates in simulations, and introducing the RM framework with supporting analytic and simulation tools, we have shown that DNP mechanisms in solids are more unified—and more tunable—than previously appreciated.

Chapter 4

Instrumentation for High-Field Pulsed DNP

4.1 Introduction

Pulsed dynamic nuclear polarization (DNP) offers a path to circumvent many of the fundamental limitations of continuous-wave (CW) DNP mechanisms at high magnetic fields. Unlike CW-DNP, which relies on saturating allowed or forbidden transitions using static microwave irradiation, pulsed-DNP approaches coherently manipulate electron spins using phase- and amplitude-modulated pulses. This distinction enables improved field scalability, access to faster sample spinning rates, and new modes of polarization transfer that do not rely on stochastic relaxation. However, implementing pulsed DNP in the millimeter-wave regime (e.g., 250 GHz / 380 MHz) presents substantial instrumentation challenges. Chief among them are the need for high-speed, high-fidelity pulse generation and efficient delivery of microwave power to the sample while preserving NMR sensitivity under magic-angle spinning (MAS) conditions.

This chapter details the design and implementation of a high-field pulsed-DNP instrumentation platform developed for 8.9 T MAS NMR experiments. The system supports arbitrary waveform generation at 250 GHz, incorporates novel resonator designs to confine and enhance the microwave field, and addresses the compatibility constraints imposed by MAS stator geometry. We describe both the signal generation chain and the mechanical integration of microwave resonators, including additive and modular fabrication approaches. Experimental performance is evaluated through S-parameter measurements and enhancement profiles obtained from various polarizing agents. The design principles and limitations encountered here serve as a foundation for the next generation of high-field MAS-DNP hardware.

4.2 Pulse Generation at 250 GHz

High-field pulsed DNP experiments require generation and delivery of coherent, high-power microwave pulses with precise control over amplitude, phase, and frequency. Unlike continuous-wave setups, where microwave power is fixed and unmodulated, pulsed DNP demands fast, programmable pulse shaping on the nanosecond scale—comparable in complexity to pulsed

NMR on the electron channel. Implementing this capability at 250 GHz poses substantial challenges due to the limited availability of fast-switching components and the narrowband nature of traditional high-power sources like gyrotrons.

To overcome these constraints, we have developed a solid-state microwave source capable of arbitrary waveform generation at 250 GHz. The architecture is modular and scalable, relying entirely on commercially available components and frequency multiplication. The signal chain begins with a high-performance arbitrary waveform generator (AWG) operating at a sampling rate of 12 GSa/s with 12-bit vertical resolution and a bandwidth of approximately 5 GHz. This enables generation of pulses with sub-nanosecond rise times, frequency chirps spanning hundreds of MHz, and precise phase cycling.

The AWG output is combined with a 60 GHz local oscillator in an IQ mixer to generate sidebands in the 61.5–63.5 GHz range. To minimize mixing artifacts, the intermediate frequency (IF) is placed as close as possible to the target band, reducing the multiplication factor required in subsequent stages. A bandpass filter removes higher-order sidebands and image frequencies from the mixer output, after which the signal is amplified and passed through a two-stage frequency multiplier chain to reach the 246–254 GHz range. At the final output, up to 160 mW of power is available, sufficient for generating transverse electron Rabi frequencies exceeding 20 MHz.

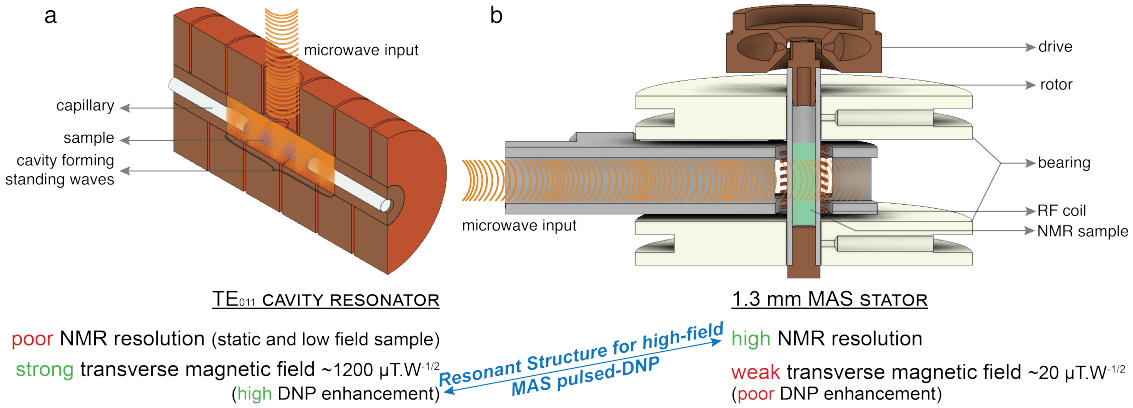

Figure 4.1: Comparison of conventional MAS stator (right) with integrated microwave resonator structure (left). Conventional stators provide excellent gas flow and spinning performance but poor confinement of the microwave magnetic field. A resonator structure offers improved field strength and confinement at the cost of spatial access.

The system's agility enables not only traditional rectangular pulses but also more complex shapes such as adiabatic sweeps, composite pulses, and phase- or frequency-modulated trains. This flexibility is crucial for implementing advanced sequences such as chirped-NOVEL, rotary resonance sweeps, or adiabatic variants of the solid effect. Importantly, the time resolution of 83 ps and full control over phase allow for manipulation of electron spin systems with fine spectral structure, such as those exhibiting anisotropic hyperfine interactions.

Compared to gyrotron-based systems, the all-solid-state design offers significant advantages in spectral purity, timing resolution, and flexibility. The spectral sharpness of the pulse is sufficient to resolve fine oscillatory features in the DNP profile, including hyperfine shoulders and substructure near the EPR center. This fidelity has enabled detailed field-swept studies

of Overhauser and solid-effect DNP in spinning samples, and the identification of new features such as coherent spin evolution or level crossings obscured in conventional measurements.

While the available power is modest compared to gyrotrons, the ability to shape and synchronize microwave pulses with NMR detection renders the system uniquely suited for pulsed DNP. The approach also lowers the barrier to adoption by replacing bulky, high-voltage microwave tubes with compact, modular, and programmable electronics. This opens the door to broader implementation of coherent spin manipulation techniques in DNP-NMR, particularly under MAS and at high magnetic fields.

4.3 Requirements for Pulsed DNP Probes

In pulsed dynamic nuclear polarization (DNP), the transfer of polarization is mediated by well-defined spin rotations of the electron, analogous to heteronuclear polarization transfer in solution-state NMR. However, implementing such control at millimeter-wave frequencies—particularly 250 GHz or higher—introduces stringent demands on the probe and resonator design.

The central requirement is the generation of a strong transverse microwave magnetic field B_1 at the position of the electron spin. For a typical pulse duration of 10–20 ns, achieving a flip angle of π requires Rabi frequencies on the order of 25–50 MHz, corresponding to $B_1 \approx 1 - 2$ mT. Generating such fields is non-trivial at 250 GHz, where the free-space wavelength is 1.2 mm, and resonator geometries are constrained by both physical size and field distribution. Previous designs without a resonator structure fail to address this issue [142], meaning that a resonating microwave structure is absolutely needed.

In addition to field strength, the bandwidth of the microwave structure becomes critical. Many pulsed DNP sequences, such as chirped solid effect, require frequency sweeps of several hundred MHz. With shaped sequences this becomes a greater issue since if the sideband of sequences lie out of the bandwidth, then the pulse become distorted and spin dynamics become practically unpredictable. Structures that provide high B_1 through resonance enhancement—such as cylindrical cavities—tend to be narrowband. Conversely, non-resonant structures offer broader bandwidth but poor field confinement, reducing polarization efficiency.

These challenges are compounded by the use of magic-angle spinning (MAS), which introduces further geometric constraints. The rotor must be spun stably at least 5–15 kHz under cryogenic conditions, with continuous gas flow for bearing, drive, and variable temperature regulation. Conventional stators are designed to optimize these parameters but offer minimal electromagnetic confinement. Moreover, they are made of materials and geometries incompatible with high-Q microwave resonance.

Thus, an ideal pulsed DNP probe must balance the following competing requirements:

- **High transverse microwave field** B_1: to allow short, coherent pulses on the electron spin.
- **Broad bandwidth**: to support chirped and shaped pulses, especially for mechanisms with frequency-modulated pulses such as ASE.

- **MAS compatibility**: including a central bore for the rotor, gas channels, and thermal insulation, and putting requirement on rotor material.
- **RF integration**: since the same structure is ideally used for NMR signal detection on nuclei (e.g., ^{1}H, ^{13}C), it must also function as an RF coil.
- **Minimal microwave loss**: to preserve power and avoid heating up unwanted parts of the probe, especially in cryogenic operation.

These constraints preclude the use of conventional high-frequency cavities and necessitate new design strategies that combine the performance of a microwave resonator with the practical requirements of a MAS stator. The following sections describe two such approaches pursued in our laboratory: (1) a monolithic helical-cut copper resonator produced via additive manufacturing, and (2) a modular, disc-assembled structure that can be tuned and assembled in situ.

4.4 Resonator Designs Developed

To meet the demanding requirements outlined in the previous section, we developed two custom microwave resonator structures that enable strong transverse fields at 250 GHz while maintaining compatibility with MAS NMR. Each approach prioritizes different aspects of performance—mechanical simplicity, tunability, bandwidth, and integration potential—and provides complementary advantages for future DNP probe development.

4.4.1 Helical-Cut Resonator

The first approach utilizes additive manufacturing to create a monolithic resonator in high-purity copper. The geometry is based on a modified cylindrical TE_{011} cavity, which is perturbed by a helical cut along its axis.[143] The cut makes the cavity essentially behave like an rf coil, greatly reducing the space requirement and minimizes rf circuit's effect on microwaves. However, these cuts introduces a non-cylindrical asymmetry and a possible leak pathway of microwave power. While making the cut thinner partially addresses the latter issue, care must be taken because high voltage in the rf circuit may cause occasional arcs, ruining NMR signal. Plus, thin cuts that doesn't follow a single surface but rather spirals up is very hard to manufacture. Nevertheless if carefully implemented, this allows the structure to support both the microwave excitation near 250 GHz and the NMR detection at lower frequencies (e.g., 380 MHz for ^{1}H) within a single element.

The helical cut also provides enhanced accessibility for integrating the MAS rotor and gas handling components, which would otherwise be obstructed in a conventional high-Q cavity. CST simulations of the helical-cut design show a pronounced resonance in the 248–252 GHz range, with a quality factor $Q \sim 100\breve{}150$, sufficient to generate B_1 fields exceeding 1 mT with moderate input power.

Experimental verification was performed using vector network analyzer (VNA) S_{11} reflection measurements. We observed resonance structure, matching well and confirms that the structure is suitable for pulse delivery in the 250 GHz band. The design offers a viable

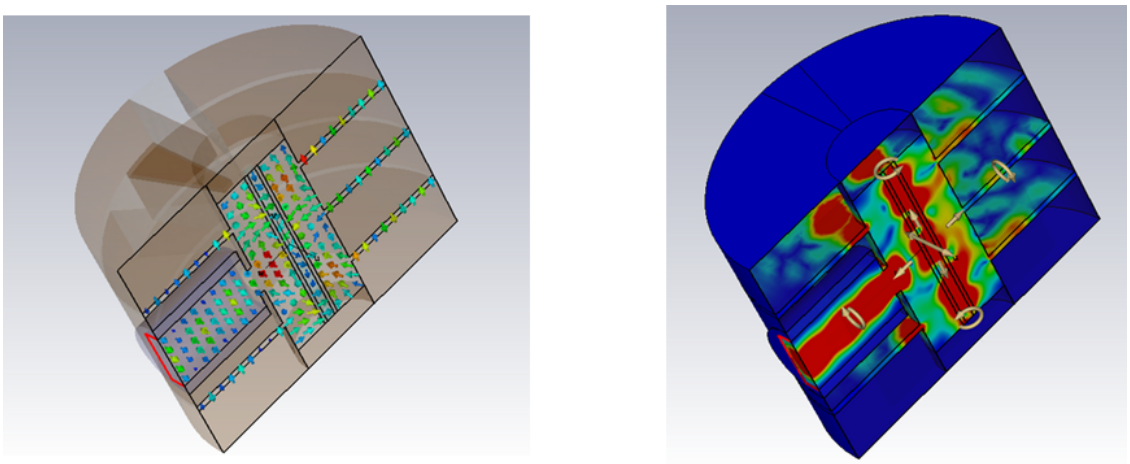

Figure 4.2: Simulated electric field distribution (left) and microwave power distribution (right). The waveguide introduces the microwave from the bottom-left side. Note the axial component in electric field, which should not appear if the resonator is perfectly cylindrical symmetric.

solution for MAS-compatible resonator construction, particularly when advanced geometries and tight tolerances are required. However, the tight tolerance is hard to manufacture in practice, and the resulting frequency is shifted to a higher field. This reminds us that a subtle tuning scheme must be designed along with the resonator.

As shown in Figure 4.3, the resonator structure gives a desirable Q-factor of around 300. The coarse tuning scheme of two movable plungers at each end of the resonator provides tuning capabilities, but certainly not optimal and neither practical with a rotor insert. This demands us to develop methods to (1) slightly modify the size parameter of the setup to allow for better tuning and (2) try to understand the underlying structure to give larger tolerances for manufacturing.

4.4.2 Disc-Assembled Resonator (Machined Modular Design)

The second approach uses a modular architecture in which individual copper discs are precision-machined and stacked to form a resonant cavity. Each disc is designed with a central aperture to accommodate the MAS rotor and dielectric spacers between the discs act as both tuning elements and dielectric loading.

The disc-assembled resonator is easier to prototype and modify than the monolithic design, allowing for rapid iterations during development. It also reduces axial surface current by being mostly cylindrical, with many number of layers. Simulations and VNA measurements demonstrate a resonance near 250 GHz, though the observed quality factor and tunability are slightly inferior to the additive variant.

Despite its modularity and tuning flexibility, the disc-assembled resonator exhibits serious limitations that fundamentally constrain its performance as an integrated NMR–EPR probe. The primary drawback does not arise from the EPR resonance alone—though the quality factor suffers from structural discontinuities—but from the demands placed on the RF circuit used for nuclear detection. The assembly relies on mechanical contact between stacked brass

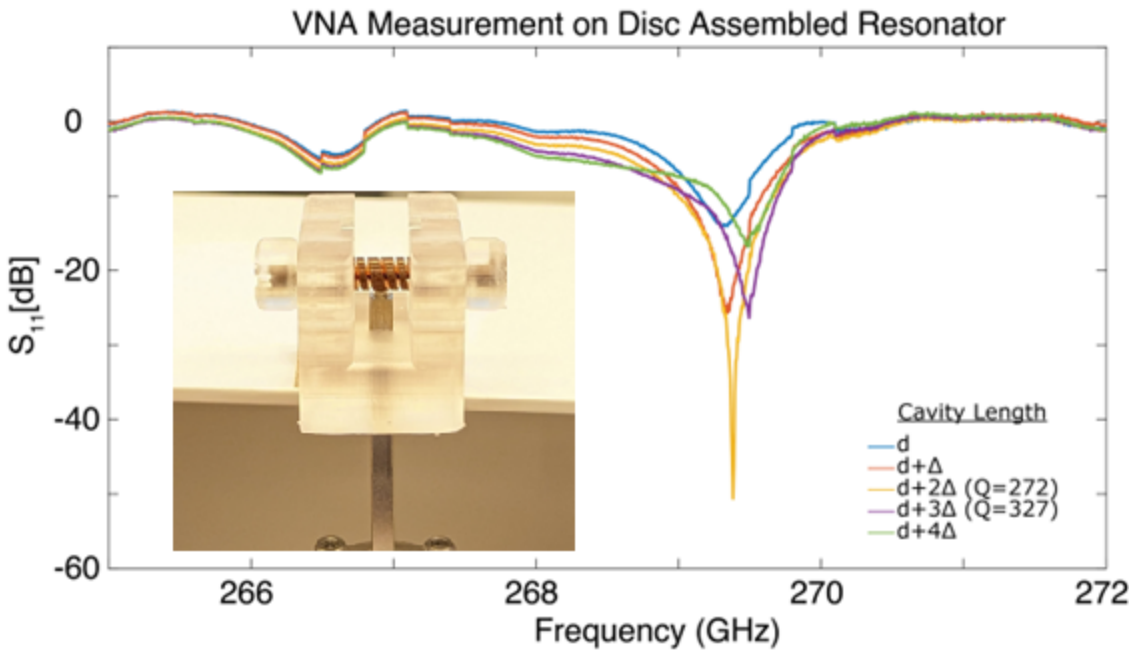

Figure 4.3: Testing of an early resonator design.

or copper discs, with no soldering or continuous metallization across interfaces. This results in a highly variable and pressure-sensitive electrical connection. Because brass is a relatively soft metal, even small changes in torque or compression during assembly or thermal cycling can lead to visible deformation, misalignment, or loss of resonance.

These imperfections already degrade the microwave resonance, broadening the line and reducing field confinement. However, their impact on the NMR channel is even more severe. Nuclear magnetic resonance detection operates at vastly lower signal-to-noise ratios and is highly sensitive to losses in the RF chain. Any increase in resistive losses at the contact points directly translates into decreased Q, reduced voltage step-up, and compromised sensitivity. Unlike EPR, which can tolerate some degree of detuning or asymmetry, NMR performance degrades rapidly if the coil is not perfectly matched and the RF field is not efficiently delivered.

Moreover, the modular geometry makes it difficult to maintain consistent electromagnetic boundary conditions. Minor shifts in disc spacing or alignment—imperceptible at millimeter scale—can disrupt the mode structure of the cavity or RF coil and break the resonance condition entirely. As a result, while the disc-based design is useful for rapid prototyping and proof-of-concept testing, it is not well suited to applications requiring reliable RF performance under MAS, particularly for multi-nuclear or broadband detection. Future iterations would require either improved mechanical stabilization, use of harder metals or plated interfaces, or a transition to a fully metallized and monolithic structure to meet the stringent demands of pulsed MAS-DNP at high fields.

Taken together, these two resonator architectures represent firm paths toward fully integrated, MAS-compatible high-field DNP probes. The helical design offers higher performance and monolithic construction, while the disc resonator provides modularity and accessibility for development and testing.

Figure 4.4: [
The disc-assembled resonator design.]

4.5 MAS Compatibility and Integration Challenges

Integrating high-frequency microwave resonators into a magic-angle spinning (MAS) NMR environment remains one of the most fundamental engineering obstacles in the development of high-field pulsed DNP systems. Unlike static solid-state NMR, MAS introduces a strict set of spatial, mechanical, and thermal constraints that severely limit design freedom. These constraints often conflict directly with the requirements for generating strong, confined microwave fields and efficient radio frequency detection.

The first major constraint is geometric: MAS stators require an unobstructed central bore for the rotor, as well as dedicated channels for bearing gas, drive gas, and variable temperature regulation. The dimensions of the rotor, typically 1.3–3.2 mm in diameter, leave very limited room for any surrounding resonant structure. Furthermore, the microwave and RF fields must be confined close to the sample, while avoiding field distortion due to nearby dielectric materials (rotor walls, gas channels) and conductive boundaries. Plus, the rotor itself serves as a pathway of microwave leakage, further diminishing the microwave efficiency.

Second, MAS operation introduces mechanical instability. The rotor spins faster than 5–15 kHz under cryogenic conditions, and the entire probe must withstand thermal contraction, mechanical vibration, and long-term rotation without detuning. In this context, mechanically fragile or pressure-sensitive resonator designs—such as the disc-assembled structure—are inherently risky. Even minor shifts in contact pressure or alignment can detune the cavity or disrupt the mode structure, especially at 250 GHz where tolerances are sub-millimeter. And large-scale movement may even lead to rotor crashes and completely destroyed probes.

Third, MAS imposes RF constraints. Any resonant structure used for microwave delivery must also function as an NMR coil for signal detection. This requires careful impedance

matching and isolation between the RF and microwave paths. However, many microwave resonator geometries are incompatible with broadband, low-loss RF operation. For instance, designs that include solenoid coil blocks almost always block most of the microwave from entering the rotor.

Finally, thermal management becomes critical. Pulsed DNP sequences involve high peak microwave power, and any excess dielectric or resistive heating must be dissipated without disturbing MAS performance. The temperature gradiant may cause unwanted distortion and friction, rendering MAS unstable. However, the materials and interfaces that make this possible—e.g., low-loss ceramics or even diamond, vacuum gaps, or heat sinks—can further complicate the electromagnetic design or reduce microwave coupling efficiency.

These MAS-related constraints are not secondary—they define the engineering envelope within which all high-field DNP hardware must be built. The resonator designs described in this chapter represent efforts to navigate these limitations by prioritizing different trade-offs: the monolithic helical-cut design offers better stability and confinement, while the disc-assembled design enables faster iteration and adjustment. However, neither solution fully resolves the MAS integration problem, and future work must continue to develop geometries that are inherently MAS-compatible, mechanically robust, and electromagnetically efficient across both EPR and NMR domains. With development of 3D printing technologies, the future seem to be brighter than before.

4.6 Summary and Outlook

This chapter has presented the design and implementation of a high-field pulsed DNP system operating at 250 GHz, with particular emphasis on the pulse generation chain and microwave resonator structures compatible with MAS NMR. The architecture developed here leverages solid-state microwave components and arbitrary waveform control to enable nanosecond-resolved amplitude and frequency modulation, offering a flexible alternative to traditional gyrotron sources. This platform has already enabled coherent pulsed-DNP experiments with enhanced spectral resolution and controllability.

The challenge of delivering these pulses to a spinning sample remains a central bottleneck. Conventional MAS stators, optimized for rotor stability and thermal control, offer poor microwave field confinement and are fundamentally incompatible with high-Q resonator geometries. To address this, two complementary resonator designs were developed: a monolithic helical-cut structure fabricated via additive manufacturing, and a modular disc-assembled resonator. While each offers distinct advantages—mechanical integrity versus tunability—both fall short of simultaneously achieving strong microwave delivery and stable NMR detection under MAS conditions.

In particular, the RF limitations of the disc-based design underscore the difficulty of merging EPR and NMR performance in a single structure. Poor electrical contact between stacked components introduces variable losses that are fatal for nuclear detection, where signal-to-noise ratios are inherently low. Even small distortions due to pressure or thermal changes can disrupt resonance and degrade performance. These constraints, exacerbated by the spinning environment, highlight the need for resonator designs that are intrinsically robust, monolithic, and compatible with the confined geometry of MAS rotors.

Looking forward, future probe development must aim to unify microwave efficiency, RF sensitivity, and MAS compatibility. This will likely require new hybrid geometries, improved materials for metallization and support, and tighter integration between resonator simulation, mechanical tolerancing, and NMR coil design. The work presented here defines the engineering envelope for such systems and offers foundational solutions to many of the most critical challenges. Continued refinement of these designs will be essential to realize the full potential of pulsed DNP at high fields and enable its widespread adoption in structural biology and materials science.

Chapter 5

Conclusions and Outlook

This thesis has explored dynamic nuclear polarization in solid-state NMR from multiple, deeply integrated perspectives: theoretical modeling, mechanism discovery, experimental validation, and instrumental development. A central theme has been the unification of pulsed and continuous-wave (CW) DNP phenomena through a coherent framework that emphasizes spin dynamics, resonant modulation, and relaxation-mediated transfer.

We began by constructing a theoretical description of spin polarization transfer under strong driving, showing how time-dependent interactions in the rotating and interaction pictures give rise to mechanisms such as NOVEL, the solid effect, and frequency-swept transfer. This framework was extended with a frequency-domain treatment of the spin trajectory and Landau–Zener-style transitions, revealing that many pulsed DNP effects can be interpreted as resonance phenomena within a driven two-level system. The trajectory-based model not only provided intuition for coherent pulse design but also highlighted the critical role of hyperfine structure. Most importantly, the Landau-Zener type sweeps found its theoretical root and provides strong improvement upon existing pulse sequences.

Chapter 3 demonstrated that the Overhauser effect, often assumed to be inactive in insulating solids, can be revived under MAS conditions when local relaxation pathways are properly engineered. We showed that selective deuteration of BDPA suppresses deleterious double-quantum cross-relaxation, yielding record enhancements. Furthermore, we introduced the concept of resonant mixing as a distinct DNP mechanism: one that shares features with both the Overhauser effect and solid effect but originates from coherent modulation near the electron–nuclear level anti-crossing. These results collectively suggest that many DNP effects—previously labeled separately—may in fact reflect different regimes of a shared, relaxation-coupled Hamiltonian.

Chapter 4 focused on the hardware required to realize such experiments at high field. We described the development of a 250 GHz pulse generation system capable of arbitrary waveform synthesis with nanosecond resolution. Two resonator structures were constructed to deliver these pulses under MAS: a monolithic helical-cut cavity and a modular disc-assembled design. Each offers a distinct compromise between microwave performance, mechanical stability, and NMR detection efficiency. The practical limitations encountered—especially in maintaining RF quality and MAS compatibility—highlight the need for tighter integration between resonator physics and rotor-based sample delivery.

Together, these studies establish a rigorous and flexible foundation for high-field DNP in

solids. They show that coherent control, hyperfine engineering, and thoughtful instrumentation are not isolated components but must work in concert to realize reliable, scalable signal enhancements.

Outlook. Several challenges remain. Relaxation remains both an enabler and a constraint; future work should incorporate it explicitly into spin transfer modeling. Instrumentation must continue to evolve toward compact, MAS-compatible designs that support both EPR excitation and broadband NMR detection. Finally, the possibility that OE, RM, SE, and CE mechanisms can be understood as points in a unified dynamical phase space opens the door to a more general theory of polarization transfer—one that does not merely classify mechanisms but predicts and designs them. This thesis lays the groundwork for such a perspective.

Appendix A

Code listing

This part summarizes typical kinds of code used in Section 2, one typical file picked from one catagory.

NMR programming:

Listing A.1: qband.rnmrm

```
; qband.rnmrm

gblarg qbandhost wallace
gblarg qbandport 4321

goto .&1

.freq
  macarg ,freq
  lclarg command "freq &freq"
  msg "&command"
  dcl "echo &command | nc -w1 %qbandhost %qbandport"
  goto .reply
mexit

.power
  macarg ,pow
  lclarg command "power &pow"
  msg "&command"
  dcl "echo &command | nc -w1 %qbandhost %qbandport"
  goto .reply
mexit

.shape
  macarg ,shp1,shp2
  lclarg command "shape &shp1 &shp2"
  msg "&command"
```

```
  dcl "echo &command | nc -w1 %qbandhost %qbandport"
  goto .reply
mexit

.param
  macarg ,ndnp,tsw,tco
  lclarg command "param &ndnp &tsw &tco"
  msg "&command"
  dcl "echo &command | nc -w1 %qbandhost %qbandport"
  goto .reply
mexit

.span
  macarg ,span
  lclarg command "span &span"
  msg "&command"
  dcl "echo &command | nc -w1 %qbandhost %qbandport"
  goto .reply
mexit

.len
  macarg ,len
  lclarg command "length &len"
  msg "&command"
  dcl "echo &command | nc -w1 %qbandhost %qbandport"
  goto .reply
mexit

.stop
  dcl "echo stop | nc -w1 %qbandhost %qbandport"
  msg "q-band stop signal sent"
mexit

.start
  dcl "echo start | nc -w1 %qbandhost %qbandport"
  msg "q-band start signal sent"
mexit

.abort
  dcl "echo abort | nc -w1 %qbandhost %qbandport"
  msg "q-band end signal sent"
mexit

.reply
  dcl "nc -l %qbandport > qband_response.wrt"
  opnrd qband_response.wrt
  rdwrt reply
```

```
  clsrd
  ifeq &reply "FAIL" . .+2
    msg "FAILED"
    ABORT
mexit
```

Listing A.2: satrecmm.rnmrm

```
macarg submac
dflt submac options 'enter submacro'
goto .&submac
mexit

.options
msg 'submacro options:'
msg '--------Pulse sequence components-------'
msg 'general: sets channel(s) and safe defaults'
msg 'satrec: saturation - tau - 90 - acq'
msg 'invrec: 180 - tau - 90 - acq'
msg 'echo: adds echo detection'
msg '---------------PPMD setup---------------'
msg 'satppmd: 8-step ppmd for saturation pulses'
msg 'invppmd: 8-step ppmd for inversion pulses'
msg 'fidppmd: 8-step ppmd for fid detection'
msg 'echoppmd: 8-step ppmd for echo detection'
msg '-----------included channels------------'
msg 'H1params'
msg 'Br79params'
mexit

.general
msg '(Saturation) (Inversion) Recovery (w/ Echo)'
ex &macro$
!&macro$ Br79params
!&macro$ H1params
!&macro$ H2params
!&macro$ C13params
flag sat off
flag inv off
flag echo off
d tau 250
ls ntau 4
&macro$ fidppmd
mexit

.C13params
nchn 2
chn 12
```

```
suchn 1,c13,0,100,100,50

unit /freq ppm
f 1 150

p satpls 5
pwx 1 satpls 65 ; satpls ~pi/2
p satdly 264 ; delay between pulses, just > rotor
ls nsat 12 ; x3 = # of pulses

supls 1,inv,65,10.0 ; pi pulse
supls 1,detect,65,5.0 ; pi/2 pulse for readout
d tauecho 0.250
p sub 20.8
supls 1,echo,65,5.0

suacq 20,256,15,50,32,0,10

&macro$ H1decparams
mexit

.H1decparams
suchn 2,h1,0,100,100,50
super 2,sample,on,*,%ph25,18.2
supsxval 2,sample,tppm,23,0
psxex 2 *&macro$
mexit

.Br79params
nchn 1
chn 1
suchn 1,br79,0,100,100,50

unit /freq ppm
f 1 75

p satpls 5
pwx 1 satpls 65 ; satpls ~pi/2
p satdly 264 ; delay between pulses, just > rotor
ls nsat 12 ; x3 = # of pulses

supls 1,inv,65,10.0 ; pi pulse
supls 1,detect,65,5.0 ; pi/2 pulse for readout
d tauecho 0.250
p sub 20.8
supls 1,echo,65,5.0

```

```
suacq 10.4,1024,0.3,50,64,0,10

mexit

.H1params
nchn 1
chn 3
suchn 1,h1,0,100,100,50

unit /freq ppm
f 1 0

p satpls 2.5
pwx 1 satpls 100 ; satpls ~pi/2
p satdly 225 ; delay between pulses, just > rotor
ls nsat 12 ; x3 = # of pulses

supls 1,inv,100,2.5 ; pi pulse
supls 1,detect,100,2.5 ; pi/2 pulse for readout
d tauecho 0.2
p sub 20
supls 1,echo,100,2.5

suacq 10,1024,0.2,30,8,0,10

mexit

.H2params
  nchn 1
  chn 3
  suchn 1,h2,0,100,100,50

  unit /freq ppm
  f 1 0

  p satpls 5      ; saturation pulse length (us)
  pwx 1 satpls 78 ; satpls ~pi/2
  p satdly 153    ; delay between pulses, just > rotor
  ls nsat 12      ; times 3 = # of pulses

  supls 1,inv,78,10.0   ; pi pulse
  supls 1,detect,78,5.0 ; pi/2 pulse for readout
  d tauecho 0.2
  p sub 20              ; ?
  supls 1,echo,78,10.0

  suacq 10,1024,0.2,30,8,0,10
```

```
mexit

.satrec
flag sat on
&macro$ satppmd
mexit

.echo
flag echo on
p 8 0
&macro$ echoppmd
mexit

.fidppmd
namd 8
ppmd detect1 1234 1234
amd 1234 1234
mexit

.echoppmd4
namd 4
PPMD detect1  1122
PPMD echo1    2431
AMD           4411
mexit

.echoppmd
namd 8
PPMD detect1,1234 1234
PPMD echo1,2341 4123
AMD 1234 1234
mexit

.satppmd
ppmd 1 1122
ppmd 2 2233
ppmd satpls 13
mexit

.t1init
tst lst t1
dltlst t1
endtst
crtlst t1 12
apnlst t1
;;0
;;1
```

```
;;2
;;3
;;4
;;8
;;12
;;16
;;20
;;40
;;60
;;80

tst lst ns
dltlst ns
endtst
crtlst ns 12
apnlst ns
;;32
;;32
;;32
;;32
;;32
;;16
;;16
;;8
;;8
;;4
;;4
;;4
mexit

.kbrt1
&macro$ t1init
opnwrt t1
&macro$ general
&macro$ Br79params
&macro$ satrec
titlea 'KBr T1 Measurement (SatRec)'
unit /freq ppm
f 1 79.3
rd 0.2
d tau 25
&macro$ t1loop
clswrt
mexit

.t1loop
set info lcl tmp sz
```

```
  sizlst t1
d tau >>taus
calc 3 ndec &taus 1000.0 div >>taus
size >>sz2
ptra >>rdrec >>wrrec
mtools targetrec &wrrec &dstrec
  rtnarg dstrec
allb &dstrec 2 &sz2 &sz 1
do /lcl 1 &sz block
  lst t1 &block >>ntau
  lst ns &block >>na
  calc 3 ndec &ntau &taus mul >>curtau
  msg "&block / &sz : tau = &curtau s"
  na &na
  ls ntau &ntau
  run
  gav
  ai
  sb &dstrec &block
  mag
  bc
  set info lcl ri
    intrg
  wrt "&curtau &ri"
enddo
mexit

.PSXEX2
SUPSXEX 2,SAMPLE,TPPM
MEXIT
```

Listing A.3: a202406.rnmrm

```
This file is too long - see /var/rnmr/rnmra/mardini/macro/a202406.
   rnmrm
```

EPR generation:

Listing A.4: Adphigen.py

```
import numpy as np
import sys

def gen_pp(pulseDuration, angle, N, phisweep, tco):
    # Write the file
    tot = pulseDuration * 4 * N
    fileMaxLen = 3840
    fileCnt = (tot + fileMaxLen - 1) // fileMaxLen
    curNo = 0
    curSec = -1
```

```
    deltaphi = phisweep / 2 * np.tan((-1 + (2 * float(curNo)) / (N - 1)) * tco) / np.tan(tco)
    deltaTe = 2 * pulseDuration # + int(round(deltaTs))
    for x in range(fileCnt):
    saveNo = 41 + x
    filename = "/home/xuser/xeprFiles/Shapes/TPPM/TPPM"+str(pulseDuration)+\
      "_"+str(int(angle))+"_"+str(N)+"_"+str(saveNo)+".shp"
    cnt = min(fileMaxLen, tot - x * fileMaxLen)
    try:
      with open(filename, 'w') as file:
        file.write("begin shape"+str(saveNo)+" \"TPPM"+str(N)+"_"+str(x)+"\"\n")
        for i in range(cnt):
          curSec = curSec + 1
          if curSec == 2 * deltaTe:
            curNo = curNo + 1
            curSec = 0
            deltaphi = phisweep / 2 * np.tan((-1 + (2 * float(curNo)) / (N - 1)) * tco) / np.tan(tco)
            #deltaTe = 2 * pulseDuration + int(round(deltaTs))
          if curSec % (2 * deltaTe) < deltaTe:
            file.write("{Re:.2f},{Im:.2f}\n".format(\
              Re = np.cos(np.pi * (angle + deltaphi) / 360),\
                Im = np.sin(np.pi * (angle + deltaphi) / 360)))
          else:
            file.write("{Re:.2f},{Im:.2f}\n".format(\
              Re = np.cos(np.pi * (angle + deltaphi) / 360),\
                Im = -np.sin(np.pi * (angle + deltaphi) / 360)))
        file.write("end shape"+str(saveNo)+"\n")
    except Exception as e:
      print "An error occurred: {}".format(e)
      return None
    return fileCnt

if __name__ == "__main__":
    # Extract command line arguments
    if len(sys.argv) == 6:
        pulseDuration = int(sys.argv[1])
        angle = int(sys.argv[2])
        N = int(sys.argv[3])
        phisweep = float(sys.argv[4])
        tco = float(sys.argv[5]) * np.pi / 180
        filename = gen_pp(pulseDuration, angle, N, phisweep, tco)
        print "Files generated:", filename
    else:
        print "Usage: python gen_pp.py <tp> <phi> <N> <phisweep> <tco
```

```
            >"
```

XEPR control:

Listing A.5: Adphigen.py

```
import socket
import time
import math
import os,sys
sys.path.insert(0, os.popen("Xepr --apipath").read().rstrip())
import XeprAPI
Xepr=XeprAPI.Xepr()
exp_Name = 'Experiment'
XExp=Xepr.XeprExperiment(name_or_vp = exp_Name)
pattEdit = XExp["*ftEpr.PatternEdit"]

qband_host = socket.gethostname()
rnmr_host = "speca.cmr.mit.edu"
rnmr_port = 4321
# Initializing pulses
center_Freq = 33.745440
#tau_P = 10
#tau_D = 14
#pulseNo = 0
Xepr.XeprCmds.aqParSet(exp_Name,'*ftEpr.StopPlsPrg','True')
#for blockNo in range(0,150):
  #tau_r = 2 * (blockNo // 25) + 2
  #pattEdit[pulseNo,0] = blockNo * 2 * (tau_D + tau_P) + tau_r
  #time.sleep(0.05)
  #pattEdit[pulseNo,1] = tau_P
  #time.sleep(0.05)
  #pulseNo = pulseNo + 1
  #pattEdit[pulseNo,0] = blockNo * 2 * (tau_D + tau_P) + 38 - tau_r
  #time.sleep(0.05)
  #pattEdit[pulseNo,1] = tau_P
  #time.sleep(0.05)
  #pulseNo = pulseNo + 1

#exit()
receiving_socket = socket.socket()
receiving_socket.bind((qband_host, rnmr_port))
receiving_socket.listen(1)


def set_Param(row,col,val):
  while pattEdit[col,row] != val:
    Xepr.XeprCmds.aqParSet(exp_Name,'*ftEpr.PatternEdit['+str(row)+'
       ]['+str(col)+']',str(val))
```

```
    time.sleep(0.5)

def pad(arr,num):
  Z = [0]*num
  Z[:len(arr)]=arr
  return Z

# Initializing to avoid error
Shape1 = 16
Shape2 = 0
N = 2
swangle = 0
swco = 45

while True:
  # Trigger here
  # listen for command from speca
  conn, addr = receiving_socket.accept()
  print "waiting..."
  command = conn.recv(1024)
  if not command:
    print "No message?"
    continue
  # strip line break
  command = command.strip('\n')
  # parse command as containing a frequency
  command_words = command.split(' ')
  if command_words[0] == "freq":
    Freq = float(command_words[1])
    Xepr.XeprCmds.aqParSet(exp_Name,'*ftEpr.StopPlsPrg','True')
    time.sleep(1)
    Xepr.XeprCmds.aqParSet(exp_Name,'*ftEpr.ChannelSlct','AWG1')
    time.sleep(1)
    for col in range(10):
      set_Param(4,col,Freq)
      set_Param(5,col,Freq)
    Xepr.XeprCmds.aqParSet(exp_Name,'*ftEpr.ChannelSlct','AWG2')
    time.sleep(1)
    for col in range(10):
      set_Param(4,col,Freq)
      set_Param(5,col,Freq)
    print "Freq"+str(Freq)
    time.sleep(2)
    Xepr.XeprCmds.aqParSet(exp_Name,'*ftEpr.StartPlsPrg','True')
  elif command_words[0] == "stop":
    print "STOP received"
    Xepr.XeprCmds.aqParSet(exp_Name,'*ftEpr.StopPlsPrg','True')
```

```
    continue
    #break
  elif command_words[0] == "start":
    print "START received"
    Xepr.XeprCmds.aqParSet(exp_Name,'*ftEpr.StartPlsPrg','True')
    continue
    #break
  elif command_words[0] == "abort":
    print "ABORT received"
    break
  elif command_words[0] == "power":
    Power = float(command_words[1])
    print Power
    time.sleep(2)
    Xepr.XeprCmds.aqParSet('AcqHidden','*cwBridge.PowerAtten',str(
        Power))
  elif command_words[0] == "shape":
    Shape1 = int(command_words[1])
    angle = int(command_words[2])
    # N = 76800 // (4 * Shape1)
    print "Shape"+str(Shape1)+","+str(angle)+","+str(swangle)

    tot = (Shape1) * 4 * N
    fileMaxLen = 3840
    fileCnt = (tot + fileMaxLen - 1) // fileMaxLen

    if fileCnt > 20:
      print "N="+str(N)+"too long..."
      time.sleep(2)
    else:
      S1 = []
      L1 = []
      P1 = []
      S2 = []
      L2 = []
      P2 = []
      Xepr.XeprCmds.aqParSet(exp_Name,'*ftEpr.StopPlsPrg','True')
      os.system("python /home/xuser/xeprFiles/Shapes/TPPM/Adphigen.py
          "+str(Shape1) \
      +" "+str(angle)+" "+str(N)+" "+" "+str(swangle)+" "+str(swco))
      time.sleep(1)
      for x in range(fileCnt):
        Xepr.XeprCmds.aqParFromFile('AcqHidden','*sysConf.ShapeImport
            ',\
                '/home/xuser/xeprFiles/Shapes/TPPM/TPPM'+\
                  str(Shape1)+'_'+str(angle)+'_'+str(N)+'_'+\
                    str(41+x)+'.shp')
```

```
        singleTime = 2400
        curLen = min(fileMaxLen, tot - fileMaxLen * x)
        curTime = round(curLen * 0.625)
        if x % 2 == 0:
          S1.append(singleTime * x)
          L1.append(curTime)
          P1.append(41+x)
        else:
          S2.append(singleTime * x)
          L2.append(curTime)
          P2.append(41+x)
      S1 = pad(S1,10)
      L1 = pad(L1,10)
      P1 = pad(P1,10)
      S2 = pad(S2,10)
      L2 = pad(L2,10)
      P2 = pad(P2,10)
      Xepr.XeprCmds.aqParSet(exp_Name,'*ftEpr.ChannelSlct','AWG1')
      time.sleep(1)
      for col in range(9,-1,-1):
        set_Param(0,col,S1[col])
        set_Param(1,col,L1[col])
        set_Param(11,col,P1[col])
      Xepr.XeprCmds.aqParSet(exp_Name,'*ftEpr.ChannelSlct','AWG2')
      time.sleep(1)
      for col in range(9,-1,-1):
        set_Param(0,col,S2[col])
        set_Param(1,col,L2[col])
        set_Param(11,col,P2[col])
      time.sleep(1)
  elif command_words[0] == "param":
    N = int(command_words[1])
    swangle = float(command_words[2])
    swco  = int(command_words[3])
    print "param"+str(swangle)+","+str(swco)
    time.sleep(2)
  # write back to RNMR saying it's good to go
  sending_socket = socket.socket()
  sending_socket.connect((rnmr_host, rnmr_port))
  sending_socket.send("READY")
  sending_socket.close()

Xepr.XeprCmds.aqParSet(exp_Name,'*ftEpr.StopPlsPrg','True')
receiving_socket.shutdown(socket.SHUT_RDWR)
receiving_socket.close()
```

Spinach simulation:

Listing A.6: TPPM$_par_scan.m$

```
import socket
import time
import math
import os,sys
sys.path.insert(0, os.popen("Xepr --apipath").read().rstrip())
import XeprAPI
Xepr=XeprAPI.Xepr()
exp_Name = 'Experiment'
XExp=Xepr.XeprExperiment(name_or_vp = exp_Name)
pattEdit = XExp["*ftEpr.PatternEdit"]

qband_host = socket.gethostname()
rnmr_host = "speca.cmr.mit.edu"
rnmr_port = 4321
# Initializing pulses
center_Freq = 33.745440
#tau_P = 10
#tau_D = 14
#pulseNo = 0
Xepr.XeprCmds.aqParSet(exp_Name,'*ftEpr.StopPlsPrg','True')
#for blockNo in range(0,150):
  #tau_r = 2 * (blockNo // 25) + 2
  #pattEdit[pulseNo,0] = blockNo * 2 * (tau_D + tau_P) + tau_r
  #time.sleep(0.05)
  #pattEdit[pulseNo,1] = tau_P
  #time.sleep(0.05)
  #pulseNo = pulseNo + 1
  #pattEdit[pulseNo,0] = blockNo * 2 * (tau_D + tau_P) + 38 - tau_r
  #time.sleep(0.05)
  #pattEdit[pulseNo,1] = tau_P
  #time.sleep(0.05)
  #pulseNo = pulseNo + 1

#exit()
receiving_socket = socket.socket()
receiving_socket.bind((qband_host, rnmr_port))
receiving_socket.listen(1)


def set_Param(row,col,val):
  while pattEdit[col,row] != val:
    Xepr.XeprCmds.aqParSet(exp_Name,'*ftEpr.PatternEdit['+str(row)+'
       ]['+str(col)+']',str(val))
    time.sleep(0.5)

def pad(arr,num):
  Z = [0]*num
```

```
  Z[:len(arr)]=arr
  return Z

# Initializing to avoid error
Shape1 = 16
Shape2 = 0
N = 2
swangle = 0
swco = 45

while True:
  # Trigger here
  # listen for command from speca
  conn, addr = receiving_socket.accept()
  print "waiting..."
  command = conn.recv(1024)
  if not command:
    print "No message?"
    continue
  # strip line break
  command = command.strip('\n')
  # parse command as containing a frequency
  command_words = command.split(' ')
  if command_words[0] == "freq":
    Freq = float(command_words[1])
    Xepr.XeprCmds.aqParSet(exp_Name,'*ftEpr.StopPlsPrg','True')
    time.sleep(1)
    Xepr.XeprCmds.aqParSet(exp_Name,'*ftEpr.ChannelSlct','AWG1')
    time.sleep(1)
    for col in range(10):
      set_Param(4,col,Freq)
      set_Param(5,col,Freq)
    Xepr.XeprCmds.aqParSet(exp_Name,'*ftEpr.ChannelSlct','AWG2')
    time.sleep(1)
    for col in range(10):
      set_Param(4,col,Freq)
      set_Param(5,col,Freq)
    print "Freq"+str(Freq)
    time.sleep(2)
    Xepr.XeprCmds.aqParSet(exp_Name,'*ftEpr.StartPlsPrg','True')
  elif command_words[0] == "stop":
    print "STOP received"
    Xepr.XeprCmds.aqParSet(exp_Name,'*ftEpr.StopPlsPrg','True')
    continue
    #break
  elif command_words[0] == "start":
    print "START received"
```

```
    Xepr.XeprCmds.aqParSet(exp_Name,'*ftEpr.StartPlsPrg','True')
    continue
    #break
  elif command_words[0] == "abort":
    print "ABORT received"
    break
  elif command_words[0] == "power":
    Power = float(command_words[1])
    print Power
    time.sleep(2)
    Xepr.XeprCmds.aqParSet('AcqHidden','*cwBridge.PowerAtten',str(Power))
  elif command_words[0] == "shape":
    Shape1 = int(command_words[1])
    angle = int(command_words[2])
    # N = 76800 // (4 * Shape1)
    print "Shape"+str(Shape1)+","+str(angle)+","+str(swangle)

    tot = (Shape1) * 4 * N
    fileMaxLen = 3840
    fileCnt = (tot + fileMaxLen - 1) // fileMaxLen

    if fileCnt > 20:
      print "N="+str(N)+"too long..."
      time.sleep(2)
    else:
      S1 = []
      L1 = []
      P1 = []
      S2 = []
      L2 = []
      P2 = []
      Xepr.XeprCmds.aqParSet(exp_Name,'*ftEpr.StopPlsPrg','True')
      os.system("python /home/xuser/xeprFiles/Shapes/TPPM/Adphigen.py "+str(Shape1) \
      +" "+str(angle)+" "+str(N)+" "+" "+str(swangle)+" "+str(swco))
      time.sleep(1)
      for x in range(fileCnt):
        Xepr.XeprCmds.aqParFromFile('AcqHidden','*sysConf.ShapeImport',\
                '/home/xuser/xeprFiles/Shapes/TPPM/TPPM'+\
                  str(Shape1)+'_'+str(angle)+'_'+str(N)+'_'+\
                    str(41+x)+'.shp')
        singleTime = 2400
        curLen = min(fileMaxLen, tot - fileMaxLen * x)
        curTime = round(curLen * 0.625)
        if x % 2 == 0:
```

```
          S1.append(singleTime * x)
          L1.append(curTime)
          P1.append(41+x)
        else:
          S2.append(singleTime * x)
          L2.append(curTime)
          P2.append(41+x)
      S1 = pad(S1,10)
      L1 = pad(L1,10)
      P1 = pad(P1,10)
      S2 = pad(S2,10)
      L2 = pad(L2,10)
      P2 = pad(P2,10)
      Xepr.XeprCmds.aqParSet(exp_Name,'*ftEpr.ChannelSlct','AWG1')
      time.sleep(1)
      for col in range(9,-1,-1):
        set_Param(0,col,S1[col])
        set_Param(1,col,L1[col])
        set_Param(11,col,P1[col])
      Xepr.XeprCmds.aqParSet(exp_Name,'*ftEpr.ChannelSlct','AWG2')
      time.sleep(1)
      for col in range(9,-1,-1):
        set_Param(0,col,S2[col])
        set_Param(1,col,L2[col])
        set_Param(11,col,P2[col])
      time.sleep(1)
  elif command_words[0] == "param":
    N = int(command_words[1])
    swangle = float(command_words[2])
    swco  = int(command_words[3])
    print "param"+str(swangle)+","+str(swco)
    time.sleep(2)
  # write back to RNMR saying it's good to go
  sending_socket = socket.socket()
  sending_socket.connect((rnmr_host, rnmr_port))
  sending_socket.send("READY")
  sending_socket.close()

Xepr.XeprCmds.aqParSet(exp_Name,'*ftEpr.StopPlsPrg','True')
receiving_socket.shutdown(socket.SHUT_RDWR)
receiving_socket.close()
% 2D parameter scan of a TPPM DNP experiment. <I_z> after a set
% contact time is calculated as a function of electron pulse
% amplitude and offset. Further information in:
%
%                  [submitted for publication]
%
```

```
% Calculation time: minutes (a large powder grid is needed).
%
% venkata-subbarao.redrouthu@uni-konstanz.de
% guinevere.mathies@uni-konstanz.de

%function tppm_parameter_scan()

% Q-band magnet
sys.magnet=1.2142;

% Electron and two protons
sys.isotopes={'E','1H','1H'};

% Zeeman interactions (g-tensor for trityl, ppm guess for 1H)
inter.zeeman.eigs={[2.00319 2.00319 2.00258],[0 0 5],[0 5 0]};
inter.zeeman.euler=(pi/180)*{[0 10 0],[0 0 10],[100 0 0]};

% Cartesian coordinates
inter.coordinates={[0.000 0.000 0.000];
                   [0.000 3.500 0.000];
                   [2.475 2.475 0.000]};

% Spin temperature
inter.temperature=80;

% Basis set
bas.formalism='zeeman-hilb';
bas.approximation='none';

% Spinach housekeeping
spin_system=create(sys,inter);
spin_system=basis(spin_system,bas);

% Detection state
parameters.coil=state(spin_system,'Lz','1H');

% Experiment parameters
parameters.spins={'E','1H'};
parameters.pulse_dur=26.25e-9;              % pulse duration, seconds
parameters.nloops=900;                    % number of TPPM DNP blocks
parameters.phase=pi/3;                  % Second pulse 120 degrees off
parameters.grid='rep_2ang_400pts_sph';  % Spherical averaging grid
parameters.needs={'aniso_eq'};          % Sequence needs rho_eq

% Microwave resonance offset grid, Hz
offsets=linspace(-20e6,20e6,41);
reference_point=-13e6;
```

```
% Electron pulse nutation frequency grid, Hz
nutfrqs=linspace(10e6,70e6,30);

% Hush the output
spin_system.sys.output='hush';

% Generate axis ticks
[X,Y]=meshgrid(offsets/1e6,nutfrqs/1e6);

% Get the figure going
figure(); dnp_surf=zeros(numel(nutfrqs),numel(offsets));

% Loop over offsets
for m=1:numel(offsets)

    % Set the offsets
    parameters.offset=[offsets(m)+reference_point 0];

    % Parallel loop over nutation freqs
    parfor n=1:numel(nutfrqs)

        % Localise parameter array
        localpar=parameters;

        % Set electron nutation frequency
        localpar.irr_powers=nutfrqs(n);

        % Compute the contact curve
        contact_curve=powder(spin_system,@xixdnp,localpar,'esr');

        % Take the last point
        dnp_surf(n,m)=real(contact_curve(end));

    end

    % Update the plot
    contourf(X,Y,dnp_surf,100,'edgecolor','none');
    kylabel('Electron nutation frequency, MHz');
    kxlabel('Microwave resonance offset, MHz');
    kcolourbar('$I_\textrm{z}$ expectation value on $^{1}$H');
    shading flat; colormap jet; drawnow;

end

%end
```

SpinEvolution simulation:

Listing A.7: adTPPM

```
***** The System
   ********************************************************************

spectrometer(MHz)  51.7
spinning_freq(kHz) *
channels           e H1
nuclei             e H1 H1
atomic_coords      0.000 0.000 0.000 0.000 3.500 0.000 2.475 2.475
   0.000
cs_isotropic       0 1.66667 1.66667 ppm
csa_parameters     2 5 0 0 0 0 ppm
csa_parameters     3 5 0 0 90 100 ppm
g-tensor           1 2.00319 2.00319 2.00258 0 10 0
j_coupling         *
spin-spin_coupling *
quadrupole         *
dip_switchboard    *
csa_switchboard    *
exchange_nuclei    *
bond_len_nuclei    *
bond_ang_nuclei    *
tors_ang_nuclei    *
groups_nuclei      *
******* Pulse Sequence ******************************
CHN 1
timing(usec)     (top.pp)
power(kHz)         *
phase(deg)         *
freq_offs(kHz)     *
CHN 2
timing(usec)       2500
power(kHz)         0
phase(deg)         0
freq_offs(kHz)     0
******* Variables ***********************************

spin_temp=80

scan_par1d x/-100:2:100/
freq_1_1 = x*1e3

*T2SQ_1=0.0022    // T2e, ms
*T2SQ_2=1       // T2n, ms
*T2SQ_3=1       // T2n, ms

*T1SQ_1=3       // T1e, ms
```

```
*T1SQ_2=13000     // T1n, ms
*T1SQ_3=13000     // T1n, ms


** Additional T2 relaxation parameters to use with -rmz model
*T2ZQ_1_2_1=0.01
*T2DQ_1_2_1=0.01

******* Options ************************************************
rho0                Ieq
observables         F2z
EulerAngles         zcw89
n_gamma             *
line_broaden(Hz)    *
zerofill            *
FFT_dimensions      *
options             -ns1 -dp -re -id1e6 -lv -obsn
*****************************************************************************

-- Option -id1e6 is required here to prevent SpinEvolution from
   interpreting pulses with power >=500kHz as ideal; the option sets
   this limit to 1000MHz
-- The simulatiom is performed via the Liouville space propagator (
   option -lv)
```

Listing A.8: gen$_p p.py$

```
import numpy as np
import sys

def gen_pp(pulseDuration, pulsePower, N, tsweep, tco):
    # Define constants
    #pulseDuration = 0.010
    #cycleTime = 0.024
    cycleTime=pulseDuration * 2

    # Generate deltaT list
    # deltaTs = [tsweep / 2 * np.tan((-1 + 2 * float(i - 1) / (N - 1)
       ) * tco) / np.tan(tco) for i in range(1, N + 1)]

    # Generate column vectors for each deltaT and round to three
       decimal points
    column_vectors = []
    for i in range(1,N+1):
        column_vectors.append( [pulseDuration, pulseDuration])

    # Flatten the list of column vectors to create the first column
       of the file
```

```
    first_column = [item for sublist in column_vectors for item in sublist]

  # Modified second column: sequentially 0, 20000, 0 repeated
    second_column = [pulsePower,pulsePower] * (len(first_column) // 2)
    # Adjust length if necessary
    second_column = second_column[:len(first_column)]

    # Third and fourth columns: all zeros
    third_column = [0,120] * (len(first_column)//2)
    fourth_column = [0] * len(first_column)

    # Recalculate sum after rounding and adjust the last line value
    sum_first_column = sum(first_column)
    last_line_value = round(2500 - sum_first_column, 3)
    first_column.append(last_line_value)

    # Extend other columns with the corresponding values for the last line
    second_column.append(0)
    third_column.append(0)
    fourth_column.append(0)

    # Write the file
    filename = 'top.pp'
    try:
        with open(filename, 'w') as file:
            for i in range(len(first_column)):
                file.write("{}\t{}\t{}\t{}\n".format(first_column[i], second_column[i], third_column[i], fourth_column[i]))
        return filename
    except Exception as e:
        print "An error occurred: {}".format(e)
        return None

if __name__ == "__main__":
    # Extract command line arguments
    if len(sys.argv) == 6:
        pulseDuration = float(sys.argv[1])
        pulsePower = float(sys.argv[2])
        N = int(sys.argv[3])
        tsweep = float(sys.argv[4])
        tco = float(sys.argv[5])
        filename = gen_pp(pulseDuration, pulsePower, N, tsweep, tco)
        print "File generated:", filename
```

```
    else:
        print "Usage: python gen_pp.py <tp> <B1> <N> <tsweep> <tco>"
```

Listing A.9: TPPM.sh

```
#!/bin/bash

# Create a directory for raw data if it doesn't exist
mkdir -p raw_data

# Log file and processed combinations file
log_file="tppw_max_values_log.txt"
tppw_processeds_file="d_tppw_processeds.txt"

# Check if log_file exists, if not, create it
if [ ! -f "$log_file" ]; then
    touch "$log_file"
fi

# Check if tppw_processeds_file exists, if not, create it
if [ ! -f "$tppw_processeds_file" ]; then
    touch "$tppw_processeds_file"
fi

# Function to generate N values
generate_N_values() {
    for i in {625..100..625}; do
        echo $i
    done
}

# Function to check if the current triplet has already been processed
is_processed() {
    local current_triplet="N=${1}_tp=${2}_pw=${3}"
    if grep -Fxq "$current_triplet" "$tppw_processeds_file"; then
        return 0 # True, combination has been processed
    else
        return 1 # False, combination has not been processed
    fi
}

# Function to read existing maximums from the log file
declare -A max_values
read_existing_maximums() {
    while IFS= read -r line; do
        if [[ $line =~ ^Global\ Maximum\ for\ N=([0-9]+):\ (.*)$ ]]; then
            max_values[${BASH_REMATCH[1]}]="${BASH_REMATCH[2]}"
```

```
        fi
    done < "$log_file"
}

# Read existing maximums
if [ -f "$log_file" ]; then
    read_existing_maximums
fi

# Main loop
for N in $(generate_N_values); do
    # Retrieve existing global max value for this N, if available
    existing_max_info="${max_values[$N]}"
    if [[ $existing_max_info ]]; then
        # Extract the maximum value from the existing info
        global_max=$(echo "$existing_max_info" | awk '{print $NF}') # Extract the last element
        global_max_info="$existing_max_info"
        echo "Resuming with Global Maximum for N=${N}: $global_max_info"
    else
        global_max=0
        global_max_info=""
    fi

    for tp in $(seq 0.016 0.001 0.016); do
        for pw in $(seq 0 1000 52000); do
            if is_processed $N $tsweep $tco; then
                echo "Skipping already processed triplet: N=${N}, tpulse=${tp}, power=${pw}. Check data folder."
                continue
            fi

            while true; do
        echo -e "Processing triplet: N=${N}, tp=${tp}, pw=${pw}\n"

                # Call the python function with tp, pw, N, tsweep, and tco
                python gen_pp.py $tp $pw $N 0 0

        # read -n 1 -s -r -p "Press any key to continue"

                # Run spinev program
                if spinev adTOP_tppw; then
                    # Check if adTOP_tppw_re.dat exists after running spinev
                    if [ ! -f adTOP_tppw_re.dat ]; then
```

```
                        echo "adTOP_tppw_re.dat not found for N=${N}, tp=${tp}, pw=${pw}"
                        problem_occurred=true
                    else
                        problem_occurred=false
                    fi
                else
                    echo "Error in spinev command for N=${N}, tp=${tp}, pw=${pw}"
                    problem_occurred=true
                fi

                # If a problem occurred, prompt the user to retry or skip
        if [ "$problem_occurred" = true ]; then
            echo "Press 'r' to retry immediately, any other key to skip, or wait for 30 minutes to automatically retry."
            read -t 1800 -p "Enter your choice: " user_input  # 1800 seconds = 30 minutes
            if [[ $user_input == "r" ]]; then
                echo "Retrying immediately..."
                continue # Retry the same iteration
            elif [[ -z $user_input ]]; then
                echo "Automatically retrying after timeout..."
                continue # Automatic retry after timeout
            else
                echo "Skipping this triplet."
                break # Exit the loop and continue with the next triplet
            fi
        fi

                # Find the row with the maximum value in the second column of adTOP_tppw_re.dat
        max_row=$(awk 'BEGIN{max=0; line=""} $2>max{max=$2; line=$0} END{print line}' adTOP_tppw_re.dat)
        max_value=$(echo $max_row | awk '{print $2}' | sed 's/[^0-9.-]//g')  # Remove non-numeric characters

        if [[ -n $max_value && "$max_value" =~ ^-?[0-9]+(\.[0-9]+)?$ ]]; then
            if (( $(echo "$max_value > $global_max" | bc -l) )); then
                global_max=$max_value
                global_max_info="N=${N}, tp=${tp}, pw=${pw}, max_row=${max_row}"
```

```

                    # Update the log file with new global maximum
                    sed -i "/^Global Maximum for N=${N}:/d" "$log_file"
                    echo "Global Maximum for N=${N}: $global_max_info" >> "$log_file"
                fi
            else
                echo "Invalid data for comparison, skipping..."
                continue
            fi

        # Display the max_row for the current triplet
                echo -e "Triplet: N=${N}, tp=${tp}, pw=${pw}, Max Row: ${max_row}\n"
        echo -e "Global Maximum for N=${N}: $global_max_info\n"
        echo -e "==========================================\n"

                # Rename and move the file to raw_data folder
                mv adTOP_tppw_re.dat "raw_data/adTOP_tppw_re_${N}_${tp}_${pw}.dat"

        # Correctly format and log this combination as processed
        tppw_processed="N=${N}_tp=${tp}_pw=${pw}"
        if ! grep -Fxq "$tppw_processed" "$tppw_processeds_file"; then
            echo "$tppw_processed" >> "$tppw_processeds_file"
        fi
        break # Successfully processed, exit the retry loop
            done
        done
    done

    # Print the global maximum information for the current N
    echo -e "Global Maximum for N=${N}: $global_max_info\n"
done
```

Hand-written simulation:

Listing A.10: Traj$_p ow.py$

```
import numpy as np
import matplotlib.pyplot as plt
from matplotlib import cm

# --- Parameters ---
N_cycles = 1000
tau = 21 * 1.25e-9                # half-period in seconds
T = 2 * tau                        # full period (TPPM cycle)
Omega = 21e6 * 2 * np.pi           # Rabi frequency in rad/s
```

```
phi = np.pi * 60 / 360           # phase modulation (+/-)

# --- Time grid (high resolution) ---
N = 1048576                        # number of points for fine resolution
t = np.linspace(0, T * N_cycles, N, endpoint=False)
dt = t[1] - t[0]

# Phase modulation: TPPM style
phi_t = np.where(t % T < tau, phi, -phi)

# --- Rotation matrices ---
def rotation_matrix(axis, angle):
    """Return a 3x3 rotation matrix for a rotation of 'angle' radians around 'axis'."""
    axis = axis / np.linalg.norm(axis)
    x, y, z = axis
    c = np.cos(angle)
    s = np.sin(angle)
    C = 1 - c
    return np.array([
        [c + x * x * C,     x * y * C - z * s, x * z * C + y * s],
        [y * x * C + z * s, c + y * y * C,     y * z * C - x * s],
        [z * x * C - y * s, z * y * C + x * s, c + z * z * C]
    ])

# Compute R(t): 3x3xN
# Initialize R_t with identity at t=0
R_t = np.zeros((3, N))
R_t[:, 0] = np.array([0, 0, 1])

# Time step
dtheta = Omega * dt

# Recursive construction of rotation matrices
for i in range(1, N):
    axis = np.array([np.cos(phi_t[i]), np.sin(phi_t[i]), 0])  # Define the rotation axis
    dR = rotation_matrix(axis, dtheta)  # Small rotation over dt
    R_t[:, i] = np.dot(dR, R_t[:, i - 1])

# Extract x, y, z components from R_t
z_data = R_t[2, :]
x_data = (R_t[0, :] + R_t[1, :] * 1j) / np.sqrt(2)
y_data = (R_t[0, :] - R_t[1, :] * 1j) / np.sqrt(2)

# --- Perform FFT ---
```

```
# Compute the frequency axis for FFT
frequencies = np.fft.fftfreq(N, dt)

# Perform FFT on each component (x, y, z)
fft_x = np.fft.fft(x_data)
fft_y = np.fft.fft(y_data)
fft_z = np.fft.fft(z_data)

# Compute the magnitude of the FFT for each component
fft_x_magnitude = np.abs(fft_x)
fft_y_magnitude = np.abs(fft_y)
fft_z_magnitude = np.abs(fft_z)

# Combine the FFT magnitudes by taking the root of the sum of squares (RSS)
fft_rss_magnitude = np.sqrt(fft_x_magnitude**2 + fft_y_magnitude**2 + fft_z_magnitude**2)

# Plotting the FFTs of the components and RSS combined with log scale on y-axis
fig, axes = plt.subplots(4, 1, figsize=(10, 8), sharex=True)

# Plot the FFT for combined RSS in black (on top)
axes[0].plot(frequencies[:N // 2] / 1e6, fft_rss_magnitude[:N // 2], color='k', label='Total Amplitude', linestyle='--')
axes[0].set_ylabel('Magnitude (log scale)', fontsize=14)
axes[0].yaxis.label.set_position((-0.1, -1.5))
axes[0].set_yscale('log')
axes[0].set_ylim(0.1, 10000000)  # Set x-axis range from 0 to 100 MHz
axes[0].set_xlim(0, 100)  # Set x-axis range from 0 to 100 MHz
axes[0].legend()

# Plot the FFT for x-component in red
axes[1].plot(frequencies[:N // 2] / 1e6, fft_x_magnitude[:N // 2], color='r', label='FT of + component')
#axes[1].set_ylabel('Magnitude (log scale)', fontsize=14)
axes[1].set_yscale('log')
axes[1].set_ylim(0.1, 10000000)  # Set x-axis range from 0 to 100 MHz
axes[1].set_xlim(0, 100)  # Set x-axis range from 0 to 100 MHz
axes[1].legend()

# Plot the FFT for y-component in green
axes[2].plot(frequencies[:N // 2] / 1e6, fft_y_magnitude[:N // 2], color='g', label='FT of - component')
#axes[2].set_ylabel('Magnitude (log scale)', fontsize=14)
axes[2].set_yscale('log')
axes[2].set_ylim(0.1, 10000000)  # Set x-axis range from 0 to 100 MHz
```

```
axes[2].set_xlim(0, 100)  # Set x-axis range from 0 to 100 MHz
axes[2].legend()

# Plot the FFT for z-component in blue
axes[3].plot(frequencies[:N // 2] / 1e6, fft_z_magnitude[:N // 2], color='b', label='FT of z component')
axes[3].set_xlabel('Frequency (MHz)', fontsize=14)
#axes[3].set_ylabel('Magnitude (log scale)', fontsize=14)
axes[3].set_yscale('log')
axes[3].set_ylim(0.1, 10000000)  # Set x-axis range from 0 to 100 MHz
axes[3].set_xlim(0, 100)  # Set x-axis range from 0 to 100 MHz
axes[3].legend()
# Make sure the x-tick labels are visible on the last plot
axes[3].set_xticks(np.linspace(0, 100, 11))  # Set specific ticks for last plot

# Set combined x-tick and y-label for all subplots
axes[0].set_ylabel('Magnitude (log scale)', fontsize=14)  # Y-axis label only for the first subplot
axes[3].set_xlabel('Frequency (MHz)', fontsize=14)  # X-axis label only for the last subplot

# Remove X-axis from the first three subplots
for ax in axes[0:2]:
    # ax.set_xticklabels([])  # Removes the x-tick labels
    ax.set_xlabel('')  # Remove the x-label

for ax in axes[1:]:
    ax.set_xlabel('')  # Remove the x-label

# Center the y-label
# axes[0].yaxis.set_label_position('center')

# Set x-label only for the last subplot
axes[3].set_xlabel('Frequency (MHz)', fontsize=14)

for ax in axes:
    ax.axvline(x=50.5, color='k', linestyle='--', linewidth=1)

axes[3].text(50.5 + 1, ax.get_ylim()[1] * 0.5, r'$\omega_n$',
        verticalalignment='center', fontsize=18, color='k')


# Adjust layout to make the plots even tighter
plt.subplots_adjust(hspace=0.2, wspace=0.1, left=0.2, right=0.8, top=0.99, bottom=0.1)  # Reduce spaces more

```

```python
# Show the plot
plt.tight_layout(pad = 3)  # Ensure everything is packed tightly

# Save the plot to the current directory as an SVG file
plt.savefig('fft_overlay_trajectory_pm.svg', format='svg')

# Show the plot
plt.show()
```

Listing A.11: TPPM$_{p}ow.m$

```
% Parameters
tau_ns = 21 * 1.25;
tau = tau_ns * 1e-9;
T = 2 * tau;

phi_list = linspace(40, 80, 41);  % 1 deg step
N_phi = length(phi_list);

N = 2^18;
dt = 0.032e-9;
t = (0:N-1) * dt;
fs = 1/dt;
f_axis = (0:N-1)/N * fs / 1e6;  % MHz
f_win = (f_axis >= 40) & (f_axis <= 60);
f_range = f_axis(f_win);

% Prepare GIF
gif_name = 'Splus_fft_phi_sweep.gif';

% Animation loop
figure;
set(gcf,'Color','w');
for j = 1:N_phi
    phi = deg2rad(phi_list(j))/2;

    % Modulation
    phi_t = phi * ones(1, N);
    phi_t(mod(t, T) >= tau) = -phi;

    % Spin propagation
    R = zeros(3, N); R(:,1) = [0; 0; 1];
    for k = 2:N
        axis = [cos(phi_t(k)); sin(phi_t(k)); 0];
        axis = axis / norm(axis);
        angle = 2 * pi * 21e6 * dt;
        dR = cos(angle) * eye(3) + sin(angle) * skew(axis) + ...
             (1 - cos(angle)) * (axis * axis');
```

```
        R(:,k) = dR * R(:,k-1);
    end

    % FFT
    Splus = (R(1,:) + 1i * R(2,:)) / sqrt(2);
    fft_Splus = abs(fft(Splus));
    spectrum = fft_Splus(f_win);

    % Plot (log scale)
    semilogy(f_range, spectrum, 'k', 'LineWidth', 1.5); hold on;
    xline(50.5, 'r--', 'LineWidth', 1.2);  % vertical marker at 51 MHz
    hold off;

    xlabel('Frequency (MHz)');
    ylabel('|S_+(\omega)|');
    title('S_+ spectrum (40-60 MHz)');
    ylim([3e-1 1e4]);
    xlim([40 60]);
    grid on;

    % Phase slider (as text or annotation arrow)
    text(40, 3000, sprintf('\\phi = %.1f', phi_list(j)), ...
        'FontSize', 12, 'FontWeight', 'bold','HorizontalAlignment', 'left', 'VerticalAlignment', 'bottom');

    drawnow;

    % Capture frame
    frame = getframe(gcf);
    img = frame2im(frame);
    [imind, cm] = rgb2ind(img, 256);

    if j == 1
        imwrite(imind, cm, gif_name, 'gif', 'Loopcount', inf, 'DelayTime', 0.15);
    else
        imwrite(imind, cm, gif_name, 'gif', 'WriteMode', 'append', 'DelayTime', 0.15);
    end
end

% Helper
function S = skew(v)
    S = [  0      -v(3)   v(2);
          v(3)    0      -v(1);
         -v(2)    v(1)    0   ];
```

```
end
```

References

[1] S. Piazza. "First 1.2 GHz NMR Spectrometer in the United States at The Ohio State University funded by the U.S. National Science Foundation". In: *Ohio State University News* (Dec. 2023). Accessed: 2025-05-19. url: https://artsandsciences.osu.edu/news/first-1.2-ghz-nmr-spectrometer-united-states-ohio-state-university-funded-u.s.-national.

[2] D. Beriashvili, J. Zhou, Y. Liu, G. E. Folkers, and M. Baldus. "Cellular applications of DNP solid-state NMR–state of the art and a look to the future". In: *Chemistry–A European Journal* 30.28 (2024), e202400323.

[3] B. Reif, S. E. Ashbrook, L. Emsley, and M. Hong. "Solid-state NMR spectroscopy". In: *Nature Reviews Methods Primers* 1.1 (2021), p. 2.

[4] Y. Su, L. Andreas, and R. G. Griffin. "Magic angle spinning NMR of proteins: high-frequency dynamic nuclear polarization and 1H detection". In: *Annual review of biochemistry* 84.1 (2015), pp. 465–497.

[5] K. Jaudzems, T. Polenova, G. Pintacuda, H. Oschkinat, and A. Lesage. "DNP NMR of biomolecular assemblies". In: *Journal of structural biology* 206.1 (2019), pp. 90–98.

[6] T. Biedenbänder, V. Aladin, S. Saeidpour, and B. Corzilius. "Dynamic nuclear polarization for sensitivity enhancement in biomolecular solid-state NMR". In: *Chemical Reviews* 122.10 (2022), pp. 9738–9794.

[7] A. J. Rossini, A. Zagdoun, M. Lelli, J. Canivet, S. Aguado, O. Ouari, P. Tordo, M. Rosay, W. E. Maas, C. Copéret, et al. "Dynamic nuclear polarization enhanced solid-state NMR spectroscopy of functionalized metal–organic frameworks". In: *Angewandte Chemie International Edition* 51.1 (2012), pp. 123–127.

[8] S. Haber and M. Leskes. "Dynamic Nuclear Polarization in battery materials". In: *Solid state nuclear magnetic resonance* 117 (2022), p. 101763.

[9] I. B. Moroz and M. Leskes. "Dynamic nuclear polarization solid-state NMR spectroscopy for materials research". In: *Annual Review of Materials Research* 52.1 (2022), pp. 25–55.

[10] T. V. Can, M. A. Caporini, F. Mentink-Vigier, B. Corzilius, J. J. Walish, M. Rosay, W. E. Maas, M. Baldus, S. Vega, T. M. Swager, et al. "Overhauser effects in insulating solids". In: *The Journal of chemical physics* 141.6 (2014).

[11] Y. Hovav, A. Feintuch, and S. Vega. "Theoretical aspects of dynamic nuclear polarization in the solid state–the solid effect". In: *Journal of Magnetic Resonance* 207.2 (2010), pp. 176–189.

[12] Y. Hovav, A. Feintuch, and S. Vega. "Theoretical aspects of dynamic nuclear polarization in the solid state–the cross effect". In: *Journal of Magnetic Resonance* 214 (2012), pp. 29–41.

[13] L. Niccoli, G. Casano, G. Menzildjian, M. Yulikov, T. Robinson, S.-E. Akrial, Z. Wang, C. Reiter, A. Purea, D. Siri, et al. "Efficient DNP at high fields and fast MAS with antenna-sensitized dinitroxides". In: *Chemical Science* 15.40 (2024), pp. 16582–16593.

[14] S. Badoni, P. Berruyer, and L. Emsley. "Optimal sensitivity for 1H detected relayed DNP of organic solids at fast MAS". In: *Journal of Magnetic Resonance* 360 (2024), p. 107645.

[15] A. Venkatesh, G. Casano, R. Wei, Y. Rao, H. Lingua, H. Karoui, M. Yulikov, O. Ouari, and L. Emsley. "Rational design of dinitroxide polarizing agents for dynamic nuclear polarization to enhance overall NMR sensitivity". In: *Angewandte Chemie International Edition* 63.9 (2024), e202317337.

[16] N. Schröder, E. Bartalucci, B. U. Yazgi, and T. Wiegand. "Solid-state NMR Spectroscopy and Dynamic Nuclear Polarization". In: *Integrated Structural Biology*. Royal Society of Chemistry, Dec. 2023. isbn: 978-1-83916-183-4. doi: 10.1039/BK9781837670154-00043. url: https://doi.org/10.1039/BK9781837670154-00043.

[17] S. Paul, E. Bouleau, Q. Reynard-Feytis, J.-P. Arnaud, F. Bancel, B. Rollet, P. Dalban-Moreynas, C. Reiter, A. Purea, F. Engelke, et al. "Sustainable and cost-effective MAS DNP-NMR at 30 K with cryogenic sample exchange". In: *Journal of Magnetic Resonance* 356 (2023), p. 107561.

[18] F. J. Scott, E. P. Saliba, B. J. Albert, N. Alaniva, E. L. Sesti, C. Gao, N. C. Golota, E. J. Choi, A. P. Jagtap, J. J. Wittmann, et al. "Frequency-agile gyrotron for electron decoupling and pulsed dynamic nuclear polarization". In: *Journal of Magnetic Resonance* 289 (2018), pp. 45–54.

[19] A. W. Overhauser. "Polarization of nuclei in metals". In: *Physical Review* 92.2 (1953), p. 411.

[20] A. Comment, B. van den Brandt, K. Uffmann, F. Kurdzesau, S. Jannin, J. Konter, P. Hautle, W. T. Wenckebach, R. Gruetter, and J. Van Der Klink. "Design and performance of a DNP prepolarizer coupled to a rodent MRI scanner". In: *Concepts in Magnetic Resonance Part B: Magnetic Resonance Engineering: An Educational Journal* 31.4 (2007), pp. 255–269.

[21] N. Alnajar and A. Equbal. "Dynamic Nuclear Polarization-Enabled Quantum Sensing for Investigating Peptide Configurations". In: *Applied Magnetic Resonance* 55.1 (2024), pp. 239–250.

[22] K. O. Tan, M. Mardini, C. Yang, J. H. Ardenkjær-Larsen, and R. G. Griffin. "Three-spin solid effect and the spin diffusion barrier in amorphous solids". In: *Science advances* 5.7 (2019), eaax2743.

[23] E. Ravera, C. Luchinat, and G. Parigi. "Basic facts and perspectives of Overhauser DNP NMR". In: *Journal of Magnetic Resonance* 264 (2016), pp. 78–87.

[24] A. Leavesley, S. Jain, I. Kamniker, H. Zhang, S. Rajca, A. Rajca, and S. Han. "Maximizing NMR signal per unit time by facilitating the e–e–n cross effect DNP rate". In: *Physical Chemistry Chemical Physics* 20.43 (2018), pp. 27646–27657.

[25] F. Mentink-Vigier, S. Vega, and G. De Paëpe. "Fast and accurate MAS–DNP simulations of large spin ensembles". In: *Physical Chemistry Chemical Physics* 19.5 (2017), pp. 3506–3522.

[26] R. G. Griffin, T. M. Swager, and R. J. Temkin. "High frequency dynamic nuclear polarization: New directions for the 21st century". In: *Journal of magnetic resonance* 306 (2019), pp. 128–133.

[27] W. T. Wenckebach. "Electron spin–spin interactions in DNP: Thermal mixing vs. the cross effect". In: *Applied Magnetic Resonance* 52.7 (2021), pp. 731–748.

[28] K. O. Tan, S. Jawla, R. J. Temkin, and R. G. Griffin. "Pulsed dynamic nuclear polarization". In: *Handbook of High Field Dynamic Nuclear Polarization* (2019), pp. 71–86.

[29] D. Lee, S. Hediger, and G. De Paëpe. "Is solid-state NMR enhanced by dynamic nuclear polarization?" In: *Solid State Nuclear Magnetic Resonance* 66 (2015), pp. 6–20.

[30] F. Bloch. "Nuclear induction". In: *Physical review* 70.7-8 (1946), p. 460.

[31] M. Goldman. "Formal theory of spin–lattice relaxation". In: *Journal of Magnetic Resonance* 149.2 (2001), pp. 160–187.

[32] M. Leskes, P. Madhu, and S. Vega. "Floquet theory in solid-state nuclear magnetic resonance". In: *Progress in nuclear magnetic resonance spectroscopy* 57.4 (2010), pp. 345–380.

[33] G.-M. Camenisch, N. Wili, G. Jeschke, and M. Ernst. "Pulsed dynamic nuclear polarization: a comprehensive Floquet description". In: *Physical Chemistry Chemical Physics* 26.25 (2024), pp. 17666–17683.

[34] Z. Pang, S. Jain, C. Yang, X. Kong, and K. O. Tan. "A unified description for polarization-transfer mechanisms in magnetic resonance in static solids: Cross polarization and DNP". In: *The Journal of Chemical Physics* 156.24 (2022).

[35] M. Veshtort and R. G. Griffin. "SPINEVOLUTION: a powerful tool for the simulation of solid and liquid state NMR experiments". In: *Journal of Magnetic Resonance* 178.2 (2006), pp. 248–282.

[36] H. J. Hogben, M. Krzystyniak, G. T. Charnock, P. J. Hore, and I. Kuprov. "Spinach–a software library for simulation of spin dynamics in large spin systems". In: *Journal of magnetic resonance* 208.2 (2011), pp. 179–194.

[37] C. Yang, K. O. Tan, and R. G. Griffin. "DNPSOUP: A simulation software package for dynamic nuclear polarization". In: *Journal of Magnetic Resonance* 334 (2022), p. 107107.

[38] S. K. Jawla, R. G. Griffin, I. A. Mastovsky, M. A. Shapiro, and R. J. Temkin. "Second harmonic 527-GHz gyrotron for DNP-NMR: Design and experimental results". In: *IEEE transactions on electron devices* 67.1 (2019), pp. 328–334.

[39] A. Henstra and W. T. Wenckebach. "The theory of nuclear orientation via electron spin locking (NOVEL)". In: *Molecular Physics* 106.7 (2008), pp. 859–871.

[40] T. V. Can, R. T. Weber, J. J. Walish, T. M. Swager, and R. G. Griffin. "Frequency-Swept Integrated Solid Effect". In: *Angewandte Chemie* 129.24 (2017), pp. 6848–6852.

[41] T. Can, R. Weber, J. Walish, T. Swager, and R. Griffin. "Ramped-amplitude NOVEL". In: *The journal of chemical physics* 146.15 (2017).

[42] K. O. Tan, C. Yang, R. T. Weber, G. Mathies, and R. G. Griffin. "Time-optimized pulsed dynamic nuclear polarization". In: *Science advances* 5.1 (2019), eaav6909.

[43] V. S. Redrouthu and G. Mathies. "Efficient pulsed dynamic nuclear polarization with the X-inverse-X sequence". In: *Journal of the American Chemical Society* 144.4 (2022), pp. 1513–1516.

[44] V. S. Redrouthu, S. Vinod-Kumar, and G. Mathies. "Dynamic nuclear polarization by two-pulse phase modulation". In: *The Journal of Chemical Physics* 159.1 (2023).

[45] N. Wili, A. B. Nielsen, L. A. Völker, L. Schreder, N. C. Nielsen, G. Jeschke, and K. O. Tan. "Designing broadband pulsed dynamic nuclear polarization sequences in static solids". In: *Science Advances* 8.28 (2022), eabq0536.

[46] J. P. Carvalho, D. L. Goodwin, N. Wili, A. B. Nielsen, and N. C. Nielsen. "Optimal control design strategies for pulsed dynamic nuclear polarization". In: *The Journal of Chemical Physics* 162.5 (2025).

[47] A. Henstra, P. Dirksen, J. Schmidt, and W. T. Wenckebach. "Nuclear spin orientation via electron spin locking (NOVEL)". In: *Journal of Magnetic Resonance (1969)* 77.2 (1988), pp. 389–393.

[48] K. O. Tan, R. T. Weber, T. V. Can, and R. G. Griffin. "Adiabatic solid effect". In: *The journal of physical chemistry letters* 11.9 (2020), pp. 3416–3421.

[49] Y. Quan, J. Steiner, Y. Ouyang, K. O. Tan, W. T. Wenckebach, P. Hautle, and R. G. Griffin. "Integrated, stretched, and adiabatic solid effects". In: *The journal of physical chemistry letters* 13.25 (2022), pp. 5751–5757.

[50] Y. Quan, M. V. Subramanya, Y. Ouyang, M. Mardini, T. Dubroca, S. Hill, and R. G. Griffin. "Coherent dynamic nuclear polarization using chirped pulses". In: *The Journal of Physical Chemistry Letters* 14.20 (2023), pp. 4748–4753.

[51] R. Shankar, M. Ernst, P. K. Madhu, T. Vosegaard, N. C. Nielsen, and A. B. Nielsen. "A general theoretical description of the influence of isotropic chemical shift in dipolar recoupling experiments for solid-state NMR". In: *The Journal of chemical physics* 146.13 (2017).

[52] A. B. Nielsen, M. R. Hansen, J. E. Andersen, and T. Vosegaard. "Single-spin vector analysis of strongly coupled nuclei in TOCSY NMR experiments". In: *The Journal of Chemical Physics* 151.13 (2019).

[53] A. B. Nielsen, J. Carvalho, D. L. Goodwin, N. Wili, and N. C. Nielsen. "Dynamic nuclear polarization pulse sequence engineering using single-spin vector effective Hamiltonians". In: *Physical Chemistry Chemical Physics* 26.44 (2024), pp. 28208–28219.

[54] C. Vinod Chandran, P. Madhu, N. D. Kurur, and T. Bräuniger. "Swept-frequency two-pulse phase modulation (SWf-TPPM) sequences with linear sweep profile for heteronuclear decoupling in solid-state NMR". In: *Magnetic Resonance in Chemistry* 46.10 (2008), pp. 943–947.

[55] T. Can, J. McKay, R. Weber, C. Yang, T. Dubroca, J. Van Tol, S. Hill, and R. Griffin. "Frequency-swept integrated and stretched solid effect dynamic nuclear polarization". In: *The journal of physical chemistry letters* 9.12 (2018), pp. 3187–3192.

[56] A. Abragam and B. Bleaney. *Electron paramagnetic resonance of transition ions*. OUP oxford, 2012.

[57] T. W. Wenckebach. *Essentials of Dynamic Nuclear Polarization*. Springer, 2016. doi: 10.1007/978-3-319-33621-5.

[58] H.-P. Breuer and F. Petruccione. *The theory of open quantum systems*. OUP Oxford, 2002.

[59] R. S. Palani, M. Mardini, L. Delage-Laurin, D. Banks, Y. Ouyang, E. Bryerton, J. G. Kempf, T. M. Swager, and R. G. Griffin. "Amplified Overhauser DNP with Selective Deuteration: Attenuation of Double-Quantum Cross-Relaxation". In: *The Journal of Physical Chemistry Letters* 14.1 (2023). PMID: 36573841, pp. 95–100. doi: 10.1021/acs.jpclett.2c03087. eprint: https://doi.org/10.1021/acs.jpclett.2c03087. url: https://doi.org/10.1021/acs.jpclett.2c03087.

[60] A. Abragam. *The principles of nuclear magnetism*. 32. Oxford university press, 1961.

[61] C. P. Slichter. *Principles of magnetic resonance*. Vol. 1. Springer Science & Business Media, 2013.

[62] J. M. Griffiths and R. G. Griffin. "Nuclear-Magnetic-Resonance Methods for Measuring Dipolar Couplings in Rotating Solids". In: *Anal. Chim. Acta* 283 (1993), p. 1081.

[63] A. E. Bennett, R. G. Griffin, and S. Vega. "Recoupling of Homo- and Heteronuclear Dipolar Interactions in Rotating Solids". In: *NMR Basic Principles and Progress* 33 (1994), p. 1.

[64] D. A. Hall, D. C. Maus, G. J. Gerfen, S. J. Inati, L. R. Becerra, F. W. Dahlquist, and R. G. Griffin. "Polarization-enhanced NMR spectroscopy of biomolecules in frozen solution". In: *Science* 276 (1997), p. 930.

[65] S. Bahri, R. Silvers, B. Michael, K. Jaudzems, D. Lalli, G. Casano, O. Ouari, A. Lesage, G. Pintacuda, and S. Linse. "1H detection and dynamic nuclear polarization-enhanced NMR of Aβ1–42 fibrils". In: *Proc. Natl. Acad. Sci. U. S. A.* 119 (2022), e2114413119.

[66] E. J. Koers, E. A. van der Cruijsen, M. Rosay, M. Weingarth, A. Prokofyev, C. Sauvée, O. Ouari, J. van der Zwan, O. Pongs, and P. Tordo. "NMR-based structural biology enhanced by dynamic nuclear polarization at high magnetic field". In: *Journal of biomolecular NMR* 60 (2014), p. 157.

[67] A. G. Rankin, J. Trébosc, F. Pourpoint, J.-P. Amoureux, and O. Lafon. "Recent developments in MAS DNP-NMR of materials". In: *Solid State Nucl. Magn. Reson.* 101 (2019), p. 116.

[68] B. J. Albert, C. Gao, E. L. Sesti, E. P. Saliba, N. Alaniva, F. J. Scott, S. T. Sigurdsson, and A. B. Barnes. "Dynamic nuclear polarization nuclear magnetic resonance in human cells using fluorescent polarizing agents". In: *Biochemistry* 57 (2018), p. 4741.

[69] C. Gao, N. Alaniva, E. P. Saliba, E. L. Sesti, P. T. Judge, F. J. Scott, T. Halbritter, S. T. Sigurdsson, and A. B. Barnes. "Frequency-chirped dynamic nuclear polarization with magic angle spinning using a frequency-agile gyrotron". In: *J. Magn. Reson.* 308 (2019), p. 106586.

[70] M. Rosay, M. Blank, and F. Engelke. "Instrumentation for solid-state dynamic nuclear polarization with magic angle spinning NMR". In: *J. Magn. Reson.* 264 (2016), p. 88.

[71] T. Can, Q. Ni, and R. Griffin. "Mechanisms of dynamic nuclear polarization in insulating solids". In: *J. Magn. Reson.* 253 (2015), p. 23.

[72] K. Kundu, F. Mentink-Vigier, A. Feintuch, and S. Vega. "In DNP mechanisms". In: *Handbook of High Field Dynamic Nuclear Polarization* (2019), p. 15.

[73] C. Jeffries. "Dynamic orientation of nuclei by forbidden transitions in paramagnetic resonance". In: *Phys. Rev.* 117 (1960), p. 1056.

[74] T. Schmugge and C. Jeffries. "High dynamic polarization of protons". In: *Phys. Rev.* 138 (1965), A1785.

[75] C. F. Hwang and D. A. Hill. "Phenomenological model for the new effect in dynamic polarization". In: *Phys. Rev. Lett.* 19 (1967), p. 1011.

[76] A. Kessenikh, V. Lushchikov, A. Manenkov, and Y. V. Taran. "Proton polarization in irradiated polyethylenes". In: *Soviet Phys.-Solid State (English Transl.)* 5 (1963), p. 321.

[77] A. Kessenikh, A. Manenkov, and G. Pyatnitskii. "On explanation of experimental data on dynamic polarization of protons in irradiated polyethylenes". In: *Soviet Phys.-Solid State (English Transl.)* 6 (1964), p. 641.

[78] W. de Boer. "Dynamic orientation of nuclei at low temperatures". In: *Journal of Low Temperature Physics* 22 (1976), p. 185.

[79] M. Borghini. "Spin-temperature model of nuclear dynamic polarization using free radicals". In: *Phys. Rev. Lett.* 20 (1968), p. 419.

[80] W. T. Wenckebach. "Dynamic nuclear polarization via the cross effect and thermal mixing: A. The role of triple spin flips". In: *J. Magn. Reson.* 299 (2019), p. 124.

[81] W. T. Wenckebach. "Dynamic nuclear polarization via the cross effect and thermal mixing: B. Energy transport". In: *J. Magn. Reson.* 299 (2019), p. 151.

[82] T. R. Carver and C. P. Slichter. "Experimental verification of the Overhauser nuclear polarization effect". In: *Phys. Rev.* 102 (1956), p. 975.

[83] B. Corzilius. "High-field dynamic nuclear polarization". In: *Annu. Rev. Phys. Chem.* 71 (2020), p. 143.

[84] A. E. Dementyev, D. G. Cory, and C. Ramanathan. "High-field Overhauser dynamic nuclear polarization in silicon below the metal-insulator transition". In: *J. Chem. Phys.* 134 (2011), p. 154511.

[85] J. Järvinen, D. Zvezdov, J. Ahokas, S. Sheludiakov, L. Lehtonen, S. Vasiliev, L. Vlasenko, Y. Ishikawa, and Y. Fujii. "Dynamic nuclear polarization and ESR hole burning in As doped silicon". In: *Phys. Chem. Chem. Phys.* 22 (2020), p. 10227.

[86] O. Haze, B. Corzilius, A. A. Smith, R. G. Griffin, and T. M. Swager. "Water-soluble narrow-line radicals for dynamic nuclear polarization". In: *J. Am. Chem. Soc.* 134 (2012), p. 14287.

[87] X. Ji, T. Can, F. Mentink-Vigier, A. Bornet, J. Milani, B. Vuichoud, M. Caporini, R. G. Griffin, S. Jannin, and M. Goldman. "Overhauser effects in non-conducting solids at 1.2 K". In: *J. Magn. Reson.* 286 (2018), p. 138.

[88] A. Gurinov, B. Sieland, A. Kuzhelev, H. Elgabarty, T. D. Kühne, T. Prisner, J. Paradies, M. Baldus, K. L. Ivanov, and S. Pylaeva. "Mixed-Valence Compounds as Polarizing Agents for Overhauser Dynamic Nuclear Polarization in Solids". In: *Angew. Chem., Int. Ed.* 60 (2021), p. 15371.

[89] F. A. Perras, D. F. Flesariu, S. A. Southern, C. Nicolaides, J. D. Bazak, N. M. Washton, T. Trypiniotis, C. P. Constantinides, and P. A. Koutentis. "Methyl-Driven Overhauser Dynamic Nuclear Polarization". In: *J. Phys. Chem. Lett.* 13 (2022), p. 4000.

[90] S. Pylaeva, K. L. Ivanov, M. Baldus, D. Sebastiani, and H. Elgabarty. "Molecular mechanism of Overhauser dynamic nuclear polarization in insulating solids". In: *J. Phys. Chem. Lett.* 8 (2017), p. 2137.

[91] S. Pylaeva, P. Marx, G. Singh, T. D. Kühne, M. Roemelt, and H. Elgabarty. "Organic Mixed-Valence Compounds and the Overhauser Effect in Insulating Solids". In: *J. Phys. Chem. A* 125 (2021), p. 867.

[92] Y. Li, A. Equbal, T. Tabassum, and S. Han. "1H thermal mixing dynamic nuclear polarization with BDPA as polarizing agents". In: *J. Phys. Chem. Lett.* 11 (2020), p. 9195.

[93] L. Delage-Laurin, R. S. Palani, N. Golota, M. Mardini, Y. Ouyang, K. O. Tan, T. M. Swager, and R. G. Griffin. "Overhauser dynamic nuclear polarization with selectively deuterated BDPA radicals". In: *J. Am. Chem. Soc.* 143 (2021), p. 20281.

[94] T.-C. Ong, M. L. Mak-Jurkauskas, J. J. Walish, V. K. Michaelis, B. r. Corzilius, A. A. Smith, A. M. Clausen, J. C. Cheetham, T. M. Swager, and R. G. Griffin. "Solvent-free dynamic nuclear polarization of amorphous and crystalline ortho-terphenyl". In: *J. Phys. Chem. B* 117 (2013), p. 3040.

[95] S. R. Chaudhari, D. Wisser, A. C. Pinon, P. Berruyer, D. Gajan, P. Tordo, O. Ouari, C. Reiter, F. Engelke, and C. Copéret. "Dynamic nuclear polarization efficiency increased by very fast magic angle spinning". In: *J. Am. Chem. Soc.* 139 (2017), p. 10609.

[96] Y. Quan, Y. Ouyang, M. Mardini, R. S. Palani, D. Banks, J. Kempf, W. T. Wenckebach, and R. G. Griffin. "Resonant mixing dynamic nuclear polarization". In: *The Journal of Physical Chemistry Letters* 14.31 (2023), pp. 7007–7013.

[97] T. R. Carver and C. P. Slichter. "Polarization of nuclear spins in metals". In: *Physical Review* 92.1 (1953), p. 212.

[98] T. Maly, G. T. Debelouchina, V. S. Bajaj, K.-N. Hu, C.-G. Joo, M. L. Mak–Jurkauskas, J. R. Sirigiri, P. C. Van Der Wel, J. Herzfeld, R. J. Temkin, et al. "Dynamic nuclear polarization at high magnetic fields". In: *The Journal of chemical physics* 128.5 (2008).

[99] A. Barnes, G. De Paëpe, P. Van Der Wel, K.-N. Hu, C.-G. Joo, V. Bajaj, M. Mak-Jurkauskas, J. Sirigiri, J. Herzfeld, R. Temkin, et al. "High-field dynamic nuclear polarization for solid and solution biological NMR". In: *Applied magnetic resonance* 34 (2008), pp. 237–263.

[100] A. S. L. Thankamony, J. J. Wittmann, M. Kaushik, and B. Corzilius. "Dynamic nuclear polarization for sensitivity enhancement in modern solid-state NMR". In: *Progress in nuclear magnetic resonance spectroscopy* 102 (2017), pp. 120–195.

[101] K. R. Thurber and R. Tycko. "Prospects for sub-micron solid state nuclear magnetic resonance imaging with low-temperature dynamic nuclear polarization". In: *Physical Chemistry Chemical Physics* 12.22 (2010), pp. 5779–5785.

[102] I. V. Sergeyev, S. Bahri, L. A. Day, and A. E. McDermott. "Pf1 bacteriophage hydration by magic angle spinning solid-state NMR". In: *The Journal of Chemical Physics* 141.22 (2014).

[103] J. Becker-Baldus, C. Bamann, K. Saxena, H. Gustmann, L. J. Brown, R. C. Brown, C. Reiter, E. Bamberg, J. Wachtveitl, H. Schwalbe, et al. "Enlightening the photoactive site of channelrhodopsin-2 by DNP-enhanced solid-state NMR spectroscopy". In: *Proceedings of the National Academy of Sciences* 112.32 (2015), pp. 9896–9901.

[104] I. V. Sergeyev, B. Itin, R. Rogawski, L. A. Day, and A. E. McDermott. "Efficient assignment and NMR analysis of an intact virus using sequential side-chain correlations and DNP sensitization". In: *Proceedings of the National Academy of Sciences* 114.20 (2017), pp. 5171–5176.

[105] Q. Z. Ni, T. V. Can, E. Daviso, M. Belenky, R. G. Griffin, and J. Herzfeld. "Primary transfer step in the light-driven ion pump bacteriorhodopsin: An irreversible U-turn revealed by dynamic nuclear polarization-enhanced magic angle spinning NMR". In: *Journal of the American Chemical Society* 140.11 (2018), pp. 4085–4091.

[106] J. Maciejko, J. Kaur, J. Becker-Baldus, and C. Glaubitz. "Photocycle-dependent conformational changes in the proteorhodopsin cross-protomer Asp–His–Trp triad revealed by DNP-enhanced MAS-NMR". In: *Proceedings of the National Academy of Sciences* 116.17 (2019), pp. 8342–8349.

[107] T. Azais, S. Von Euw, W. Ajili, S. Auzoux-Bordenave, P. Bertani, D. Gajan, L. Emsley, N. Nassif, and A. Lesage. "Structural description of surfaces and interfaces in biominerals by DNP SENS". In: *Solid state nuclear magnetic resonance* 102 (2019), pp. 2–11.

[108] P. Berruyer, S. Björgvinsdóttir, A. Bertarello, G. Stevanato, Y. Rao, G. Karthikeyan, G. Casano, O. Ouari, M. Lelli, C. Reiter, et al. "Dynamic nuclear polarization enhancement of 200 at 21.15 T enabled by 65 kHz magic angle spinning". In: *The journal of physical chemistry letters* 11.19 (2020), pp. 8386–8391.

[109] D. J. Kubicki, S. D. Stranks, C. P. Grey, and L. Emsley. "NMR spectroscopy probes microstructure, dynamics and doping of metal halide perovskites". In: *Nature Reviews Chemistry* 5.9 (2021), pp. 624–645.

[110] H.-Y. Chen, C. B. Wilson, and R. Tycko. "Enhanced spatial resolution in magnetic resonance imaging by dynamic nuclear polarization at 5 K". In: *Proceedings of the National Academy of Sciences* 119.22 (2022), e2201644119.

[111] J. H. Ardenkjær-Larsen, B. Fridlund, A. Gram, G. Hansson, L. Hansson, M. H. Lerche, R. Servin, M. Thaning, and K. Golman. "Increase in signal-to-noise ratio of> 10,000 times in liquid-state NMR". In: *Proceedings of the National Academy of Sciences* 100.18 (2003), pp. 10158–10163.

[112] K. Golman, R. i. Zandt, M. Lerche, R. Pehrson, and J. H. Ardenkjaer-Larsen. "Metabolic imaging by hyperpolarized 13C magnetic resonance imaging for in vivo tumor diagnosis". In: *Cancer research* 66.22 (2006), pp. 10855–10860.

[113] V. A. Atsarkin. "Dynamic polarization of nuclei in solid dielectrics". In: *Soviet Physics Uspekhi* 21.9 (1978), p. 725.

[114] A. Abragam and M. Goldman. "Principles of dynamic nuclear polarisation". In: *Reports on Progress in Physics* 41.3 (1978), p. 395.

[115] A. Abragam and M. Goldman. *Nuclear magnetism: order and disorder*. Clarendon Press, 1982.

[116] T. O. Niinikoski. *The Physics of Polarized Targets*. Cambridge University Press, 2020.

[117] K.-N. Hu, V. S. Bajaj, M. Rosay, and R. G. Griffin. "High-frequency dynamic nuclear polarization using mixtures of TEMPO and trityl radicals". In: *The Journal of chemical physics* 126.4 (2007).

[118] K.-N. Hu, G. T. Debelouchina, A. A. Smith, and R. G. Griffin. "Quantum mechanical theory of dynamic nuclear polarization in solid dielectrics". In: *The Journal of chemical physics* 134.12 (2011).

[119] B. Corzilius, A. A. Smith, and R. G. Griffin. "Solid effect in magic angle spinning dynamic nuclear polarization". In: *The Journal of chemical physics* 137.5 (2012).

[120] A. Equbal, Y. Li, T. Tabassum, and S. Han. "Crossover from a solid effect to thermal mixing 1H dynamic nuclear polarization with trityl-OX063". In: *The Journal of Physical Chemistry Letters* 11.9 (2020), pp. 3718–3723.

[121] A. Karabanov, G. Kwiatkowski, C. U. Perotto, D. Wiśniewski, J. McMaster, I. Lesanovsky, and W. Köckenberger. "Dynamic nuclear polarisation by thermal mixing: quantum theory and macroscopic simulations". In: *Physical Chemistry Chemical Physics* 18.43 (2016), pp. 30093–30104.

[122] I. Marin-Montesinos, J. C. Paniagua, M. Vilaseca, A. Urtizberea, F. Luis, M. Feliz, F. Lin, S. Van Doorslaer, and M. Pons. "Self-assembled trityl radical capsules–implications for dynamic nuclear polarization". In: *Physical Chemistry Chemical Physics* 17.8 (2015), pp. 5785–5794.

[123] W. T. Wenckebach, A. Capozzi, S. Patel, and J. Ardenkjær-Larsen. "Direct measurement of the triple spin flip rate in dynamic nuclear polarization". In: *Journal of Magnetic Resonance* 327 (2021), p. 106982.

[124] R. S. Palani, M. Mardini, Y. Quan, and R. G. Griffin. "Dynamic nuclear polarization with trityl radicals". In: *Journal of Magnetic Resonance* 349 (2023), p. 107411.

[125] M. Mardini, R. S. Palani, I. M. Ahmad, S. Mandal, S. K. Jawla, E. Bryerton, R. J. Temkin, S. T. Sigurdsson, and R. G. Griffin. "Frequency-swept dynamic nuclear polarization". In: *Journal of Magnetic Resonance* 353 (2023), p. 107511.

[126] L. Lumata, Z. Kovacs, A. D. Sherry, C. Malloy, S. Hill, J. Van Tol, L. Yu, L. Song, and M. E. Merritt. "Electron spin resonance studies of trityl OX063 at a concentration optimal for DNP". In: *Physical Chemistry Chemical Physics* 15.24 (2013), pp. 9800–9807.

[127] I. Solomon. "Relaxation processes in a system of two spins". In: *Physical Review* 99.2 (1955), p. 559.

[128] A. Henstra and W. T. Wenckebach. "Dynamic nuclear polarisation via the integrated solid effect I: theory". In: *Molecular Physics* 112.13 (2014), pp. 1761–1772.

[129] A. A. Kuzhelev, D. Dai, V. Denysenkov, and T. F. Prisner. "Solid-like dynamic nuclear polarization observed in the fluid phase of lipid bilayers at 9.4 T". In: *Journal of the American Chemical Society* 144.3 (2022), pp. 1164–1168.

[130] C. Tobar, K. Albanese, R. Chaklashiya, A. Equbal, C. Hawker, and S. Han. "Multi electron spin cluster enabled dynamic nuclear polarization with sulfonated BDPA". In: *The Journal of Physical Chemistry Letters* 14.51 (2023), pp. 11640–11650.

[131] D. Sezer. "Non-perturbative treatment of the solid effect of dynamic nuclear polarization". In: *Magnetic resonance* 4.1 (2023), pp. 129–152.

[132] F. A. Perras, Y. Matsuki, S. A. Southern, T. Dubroca, D. F. Flesariu, J. Van Tol, C. P. Constantinides, and P. A. Koutentis. "Mechanistic origins of methyl-driven Overhauser DNP". In: *The Journal of Chemical Physics* 158.15 (2023).

[133] B. Corzilius, A. A. Smith, A. B. Barnes, C. Luchinat, I. Bertini, and R. G. Griffin. "High-field dynamic nuclear polarization with high-spin transition metal ions". In: *Journal of the American Chemical Society* 133.15 (2011), pp. 5648–5651.

[134] T. Wolf, S. Kumar, H. Singh, T. Chakrabarty, F. Aussenac, A. I. Frenkel, D. T. Major, and M. Leskes. "Endogenous dynamic nuclear polarization for natural abundance 17O and lithium NMR in the bulk of inorganic solids". In: *Journal of the American Chemical Society* 141.1 (2018), pp. 451–462.

[135] M. A. Hope, S. Bjorgvinsdottir, D. M. Halat, G. Menzildjian, Z. Wang, B. Zhang, J. L. MacManus-Driscoll, A. Lesage, M. Lelli, L. Emsley, et al. "Endogenous 17O dynamic nuclear polarization of Gd-doped CeO2 from 100 to 370 K". In: *The Journal of Physical Chemistry C* 125.34 (2021), pp. 18799–18809.

[136] Y. Rao, C. T. Palumbo, A. Venkatesh, M. Keener, G. Stevanato, A.-S. Chauvin, G. Menzildjian, S. Kuzin, M. Yulikov, G. Jeschke, et al. "Design principles for the development of Gd (III) polarizing agents for magic angle spinning dynamic nuclear polarization". In: *The Journal of Physical Chemistry C* 126.27 (2022), pp. 11310–11317.

[137] I. B. Moroz, Y. Feldman, R. Carmieli, X. Liu, and M. Leskes. "Endogenous metal-ion dynamic nuclear polarization for NMR signal enhancement in metal organic frameworks". In: *Chemical Science* 15.1 (2024), pp. 336–348.

[138] E. Ravera, D. Shimon, A. Feintuch, D. Goldfarb, S. Vega, A. Flori, C. Luchinat, L. Menichetti, and G. Parigi. "The effect of Gd on trityl-based dynamic nuclear polarisation in solids". In: *Physical Chemistry Chemical Physics* 17.40 (2015), pp. 26969–26978.

[139] A. Capozzi, S. Patel, W. T. Wenckebach, M. Karlsson, M. H. Lerche, and J. H. Ardenkjær-Larsen. "Gadolinium effect at high-magnetic-field DNP: 70% 13C polarization of [U-13C] glucose using trityl". In: *The journal of physical chemistry letters* 10.12 (2019), pp. 3420–3425.

[140] A. Equbal, Y. Li, A. Leavesley, S. Huang, S. Rajca, A. Rajca, and S. Han. "Truncated cross effect dynamic nuclear polarization: an overhauser effect doppelganger". In: *The journal of physical chemistry letters* 9.9 (2018), pp. 2175–2180.

[141] A. Henstra, P. Dirksen, and W. T. Wenckebach. "Enhanced dynamic nuclear polarization by the integrated solid effect". In: *Physics Letters A* 134.2 (1988), pp. 134–136.

[142] A. Purea, C. Reiter, A. I. Dimitriadis, E. de Rijk, F. Aussenac, I. Sergeyev, M. Rosay, and F. Engelke. "Improved waveguide coupling for 1.3 mm MAS DNP probes at 263 GHz". In: *Journal of Magnetic Resonance* 302 (2019), pp. 43–49.

[143] A. A. Smith, B. Corzilius, J. A. Bryant, R. DeRocher, P. P. Woskov, R. J. Temkin, and R. G. Griffin. "A 140 GHz pulsed EPR/212 MHz NMR spectrometer for DNP studies". In: *Journal of Magnetic Resonance* 223 (2012), pp. 170–179.